Degree Project in Aerospace Engineering

Second Cycle, 30 credits

Layered Autonomous Guidance For Rendezvous and Proximity Operations

DIEGO BURATTI

Authors

Diego Buratti, <diego.buratti@mail.polimi.it>
Space Engineering
KTH Royal Institute of Technology
Politecnico di Milano

Place for Project

Bremen, Germany
OHB System AG

Examiner

Dimos V. Dimarogonas
KTH Royal Institute of Technology

Supervisors

Pedro Delgado Roque, KTH Royal Institute of Technology

Gabriella Vittoria Maria Gaias, Politecnico di Milano

Stefano Torresan, OHB System AG

Thomas Peters, OHB System AG

Abstract

The technological capability to perform rendezvous between two controlled vehicles in space has witnessed a growing interest since the years of the space race between the U.S. and the Soviet Union in the 1960s as well as a progressive shift from automated and manned approaches to increasingly more autonomous systems. Moreover, in recent years, the growing number of debris comprising rocket bodies and defunct satellites in orbit around the Earth is shifting the focus of rendezvous to Active Debris Removal, which requires a servicing satellite to safely approach a non-cooperative target to begin proximity operations.

The work presented in this thesis, developed in collaboration with the AOCS & GNC Design & Software department of OHB, aims to address such need by developing an integrated guidance software which a manoeuvring satellite may use to autonomously approach and inspect an orbiting target in a safe way. This is obtained by first developing closed-form impulsive manoeuvres for arbitrarily eccentric targets in the space of Relative Orbit Elements and then designing high-level guidance strategies which adopt such schemes to accomplish mission objectives. Ultimately, the implemented guidance law is validated in a high-fidelity `MATLAB/Simulink` simulator; the results demonstrate the effectiveness of the proposed architecture and its potential reusability across different mission scenarios.

Keywords

Guidance, Rendezvous, Spacecraft, Control, Astrodynamics

Abstract

Den tekniska förmågan att genomföra rendezvous mellan två styrda farkoster i rymden har väckt ett växande intresse sedan rymdkapplöpningen mellan USA och Sovjetunionen på 1960-talet, liksom en gradvis övergång från automatiserade och bemannade lösningar till allt mer autonoma system. Dessutom har det växande antalet rymdskrot bestående av raketkroppar och uttjänta satelliter i omloppsbana runt jorden under de senaste åren flyttat fokus för rendezvous till Active Debris Removal, vilket kräver att en servicegående satellit säkert närmar sig ett icke-samarbetsvilligt mål för att påbörja närhetsoperationer.

Det arbete som presenteras i denna avhandling, som har utvecklats i samarbete med OHB:s avdelning för AOCS & GNC Design & Software, syftar till att tillgodose detta behov genom att utveckla en integrerad styrprogramvara som en manövrerande satellit kan använda för att autonomt närma sig och inspektera ett mål i omloppsbana på ett säkert sätt. Detta uppnås genom att först utveckla slutna impulsiva manövrer för godtyckligt excentriska mål i rymden med relativa banelement och sedan utforma högnivåstyrningsstrategier som använder sådana scheman för att uppnå uppdragets mål. Slutligen valideras den implementerade styrningslagen i en högupplöst `MATLAB/Simulink`-simulator; resultaten visar effektiviteten hos den föreslagna arkitekturen och dess potentiella återanvändbarhet i olika uppdragsscenarier.

Nyckelord

Vägledning, Mötesplats, Rymdfarkost, Kontroll, Astrodynamik

Acknowledgements

I would like to express my gratitude to my university supervisors Prof. Gabriella Gaias from Politecnico di Milano for her valuable technical advice and Pedro Roque from KTH for the continued support during my thesis work.

I'm also especially grateful towards the people at the AOCS & GNC Design & Software department of OHB, starting from my company advisors Thomas and Stefano; our long discussions not only provided me with precious guidance[1] but also made me more and more passionate about the topic of rendezvous. I want to say thank you to all my colleagues for always being there whenever I needed help and to Marco for now welcoming me again into his team.

Voglio dire grazie a coloro con cui ho conidiviso esperienze in giro per l'Europa e che mi hanno fatto crescere come persona; a Federica, per essermi stata accanto durante tutto questo periodo, agli amici di sempre per avermi fatto sentire a casa ad ogni mio ritorno e alla mia famiglia per aver sempre creduto in me.

September 2025

[1] Pun fully intended and also unoriginal.

Acronyms

RVD/B	Rendezvous and Docking or Berthing
RPO	Rendezvous and Proximity Operations
GNC	Guidance, Navigation and Control
ADR	Active Debris Removal
OOS	On-Orbit Servicing
PAS	Passive-Abort Safety
ISS	International Space Station
AE	Approach Ellipsoid
ECI	Earth-Centered Inertial
LVLH	Local-Vertical Local-Horizontal
RTN	Radial-Transverse-Normal
TAN	Tangential
OE	Orbital Elements
GVE	Gauss Variational Equations
CWH	Clohessy-Wiltshire-Hill
HEO	Highly-Eccentric Orbit
ROE	Relative Orbit Elements
LEO	Low-Earth Orbit
IP	In-Plane
OOP	Out-Of-Plane
STM	State Transition Matrix
KOZ	Keep-Out Zone
FSM	Finite State Machine
WSE	Walking Safe Ellipse
SSE	Stationary Safe Ellipse
POI	Points Of Interest

Contents

Chapter 1

Introduction

1.1 Orbital Rendezvous

In-orbit rendezvous is generally defined as the process by which a spacecraft, the chaser, is brought in the close vicinity of another space object, the target, by means of a sequence of manoeuvres and controlled relative trajectories [23]. From an operational point of view, it follows the initial launch and phasing stages of a space mission, in which the chaser vehicle is positioned on approximately the same orbital plane as the target. On the other hand, proximity operations identify all operations to be executed by the chaser in a close range to the target, typically as far as about 100 m [63]. Historically, the final phase of a rendezvous mission is represented by the docking/berthing stage, a process that nominally culminates in the structural connection of the two spacecraft after the attitude alignment and final approach, which can be aided by a mechanical manipulator positioned on either of the two vehicles (in case of berthing or capture) [23] [70].

As it will also become apparent during the work carried out in this thesis, the research field of rendezvous techniques naturally shares many common points with that of formation flying, which, citing the definition provided in [1], indicates missions consisting of two or more satellites that have to track and maintain a desired relative trajectory and/or a relative orientation.

To meet and satisfy the challenging requirements imposed by the concept of operations of a rendezvous mission, a large number of different technical fields is involved; Guidance, Navigation and Control (GNC) represent key enabling technologies among

them. Within the context of the presented work, which focuses on autonomous rendezvous and proximity operations, they can be defined as in the following [47][70]:

- Guidance refers to the on-board software which is designed to plan the relative trajectories used by the chaser to reach the target and the impulsive manoeuvres required to follow them. In close proximity operations it also takes on the task of generating reference paths to be followed by the continuous control;
- The navigation software is responsible to estimate the relative state[1] of the chaser with respect to the target by means of filters which receive measurement information from the sensors and the spacecraft dynamics model;
- Control is the algorithm which generates force and torques through the on-board actuators to manipulate the chaser according to mission requirements. From a practical standpoint and within the considered framework, continuous feedback control takes over the impulsive guidance once the final approach to the target spacecraft begins.

The focus of the current work lies on the guidance task which enables far-to-close range rendezvous to a target spacecraft, and in particular on the development of algorithms which comply with the typical phases and requirements of a rendezvous mission, discussed in the following sections.

1.1.1 Applications and Constraints

According to the available literature and past space missions, rendezvous and formation flying systems pave the way to a diverse range of scientific and technological applications, which include examples such as [23]:

- Re-supply and re-fueling of orbital platforms
- Exchange of crew in manned missions
- Re-joining of planetary landers to an orbiting vehicle.
- In-orbit assembly and construction
- In-orbit repair of failed spacecraft

[1]Depending on the phase, different types of navigation algorithms may be employused to estimate the relative translational and/or rotational state between the two spacecraft.

- In-orbit inspection
- Active Debris Removal (ADR)

When specifically referring to formation flying applications, even more scientific objectives can be met thanks to the capability of the spacecraft formation to create larger apertures, focal lengths and baselines for measurement instruments than what would be allowed with a single satellite [52]. As for the described rendezvous applications, the first three examples can be seen as part of the bigger trend involving Rendezvous and Docking or Berthing (RVD/B) operations oriented towards space exploration, which came to reality in the 1960s during the height of the space race between the United States and the Soviet Union with the Vostok, Gemini, Soyuz and Apollo programs [69].

The last four items of the listed applications can on the other hand be classified within the emerging On-Orbit Servicing (OOS) mission architectures, which are currently being designed to enhance sustainability of the space environment. The increasing interest of space agencies towards this trend is clearly justified by two main points [3]:

1. Life extension and re-usability of failed platforms can represent a strong financial benefit when compared to space programs based on disposable assets;
2. The need of proper post-mission disposal techniques has gained increased importance over the years due to the extreme cluttering of the space environment, caused by lack of implementation of end-of-life disposal strategies as well as renewed fragmentations due to in-orbit collisions between objects; the latter reason is one of the main factors contributing to the fast growth of the object count in the most cluttered orbits as shown in Fig.1.1.1.

Although different mission objectives call for different architectures and requirements, some common constraints can be found across different rendezvous approaches.

- Depending on the type of target safety zones (see example in Fig.1.1.2), approach-trajectory corridors and hold points along the way may be defined to allow to check out the vehicle functions, to wait for permission to proceed by ground or for navigation filters to converge to a better estimation [23]. This type of requirements also preferably calls for inherently safe trajectories, which by definition should not lead to collision with the target, even in the case of loss of

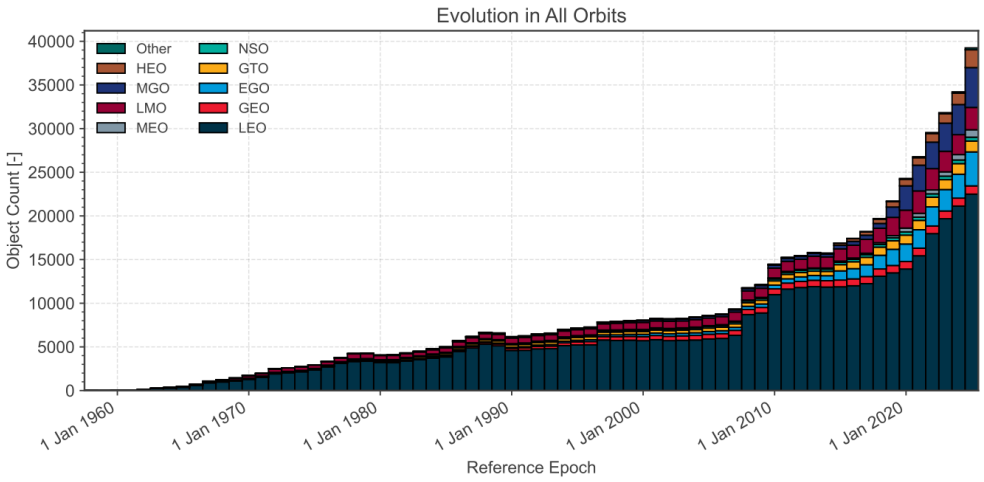

Figure 1.1.1: Number of objects divided per orbit class [45]

thrust capability at any point during the approach[2].

- The nominal attitude of the chaser spacecraft is decided by several factors, which include the need to point navigation sensors in the direction of the target and communication antennas to ground, as well as the need to point solar arrays towards the Sun to provide the necessary supply of power. Depending on the available propulsion system, it might also be necessary to properly orient the spacecraft every time a manoeuvre needs to be executed.
- Crewed missions require precise planning and synchronisation of crucial operations with proper Sun illumination conditions (critical in the last part of the approach) as well as with communication windows to ground stations. Autonomous operations may lift part of these requirements, leaving to the chaser spacecraft the capability to re-plan the trajectory to maximize observability conditions on the target.

1.1.2 Phases of Rendezvous Missions

Each space mission involving rendezvous of a chaser with a resident object is characterised by fundamentally different approach trajectories, safety requirements and time windows, dictated by nature of the target, which might be controlled or not, the main objective (*e.g*, docking, inspection), the adopted navigation system and more factors. A common ground for the general concept of operations of these missions can

[2]This constraint also takes the name of Passive-Abort Safety (PAS), and is usually defined for only a limited time horizon.

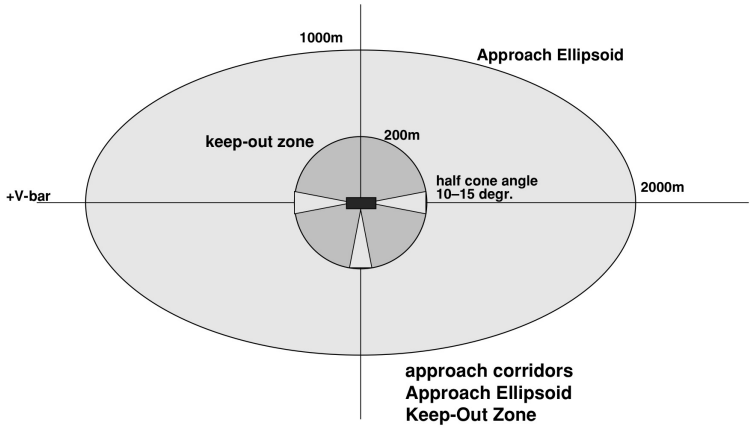

Figure 1.1.2: International Space Station (ISS) safety control zones [23]

be described by the following phases [23]:

1. The launch phase injects the chasing vehicle into the target orbital plane with controlled dispersion of the initial conditions;

2. The phasing stage has the objective to reduce the phase angle, intended as the angular separation between the two satellites, by exploiting a slightly lower chasing orbit which is characterised by a shorter orbital period. Depending on the ultimate goal of approach, the end of this phase might require to reach a predefined ”initial aim point” (mostly in docking scenarios) or to go through an ”entry gate”, an allowed region defined in the relative state of the chaser (positions and velocities);

3. The far range rendezvous typically begins when the manoeuvring spacecraft can switch from absolute to relative navigation, which is based on measurements of the target and/or shared information through intersatellite links. In the case of RVD/B missions to the ISS, this segment ends at the boundary of the Approach Ellipsoid (AE) (see Fig.1.1.2), whereas in missions requiring higher autonomy like ClearSpace-1, which is classified as ADR, this phase corresponds to an handover from the ground segment to the space segment and begins at a decision point positioned on the AE [64];

4. Close range rendezvous entails closing and fly-around manoeuvres which allow the chaser to reach the point from which the final approach (to docking, inspection or capture ...) can begin. The more the distance to the target is reduced, the more demanding are the requirements on the precision of the

relative state estimation as well as on the on-board autonomy.

Operations following close range rendezvous are very specific to the different mission profiles and cannot be generalised as well.

1.2 Approaches Towards On-Board Autonomy

The growing interest of the scientific community towards the increase of spacecraft autonomy in formation flying and rendezvous missions represents the natural evolution of the manual and automated approaches which have been pursued since the very first rendezvous demonstrations from the U.S. and the Soviet Union [69], and is based on the following advantages related to onboard autonomy [18]:

- The overall mission cost can be reduced by lightening the ground stations and control centers' operational loads;
- Inactivity or hold periods due to coverage problems and large communication delays can be reduced;
- With respect to automated approaches, the response to contingencies and failures is facilitated, potentially improving the mission safety;
- Higher flexibility and adaptability is achieved by allowing prompt response of the spacecraft to environment changes.

For these reasons, the standard orbital rendezvous techniques acquired since the space race are being reevaluated and refined with new solutions and approaches to integrate autonomous systems. Advances in the field of machine learning can represent one way with which unexpected and changing on-orbit conditions can be dealt with without bringing humans into the loop. According to [36], current approaches to spacecraft autonomy either fall in one of two categories: rule-based and optimization-based. The first category fully defines the behaviour of the spacecraft using state machine models which are characterised by a set of predefined modes and transitions between them; this modeling technique makes this approach attractive from an implementation perspective, owing to the low computing power required and the predictability of the decisions being taken. The second category sees the spacecraft and its mission profile as a functional to be minimised according to competing objectives within a constrained-optimization framework; this typically precludes direct on-board use due

to large required computing power.

The first approach, which enables autonomous yet deterministic decisions of the agent, is explored more in detail with the application to the rendezvous mission concept in Sec.3.3.1. More optimisation-oriented approaches are instead considered in Sec.3.3.2 and Sec.3.3.3.

1.3 Thesis Objectives and Structure

The objective of the work is to investigate and implement state of the art guidance algorithms for autonomous spacecraft rendezvous and inspection while prioritizing simplicity, determinism and robustness of the software to varying initial and boundary conditions. To this end, the manuscript is organized as follows:

- Chapter 2 builds the theoretical basis needed to understand, parametrize and propagate the relative motion between two spacecraft.
- Chapter 3 develops the guidance law starting from its lower logical layers, entailing analytic, closed-form manoeuvres and definition of safe relative states, and then moving to the higher layers which enable autonomous operations.
- Chapter 4 presents the integration and results of the described algorithms within the AOCS department Rendezvous and Proximity Operations (RPO) simulator, a high-fidelity nonlinear simulation tool which can be used to test GNC functions.
- Chapter 5 draws conclusions on the current work, reflecting on its limitations, contributions as well as possible ways of improvement.

1.3.1 Original Contributions

The original developments of the presented work include:

- Extension of manoeuvring algorithms for relative motion from near-circular target orbits to arbitrarily eccentric cases using quasi-non-singular Relative Orbit Elements (ROE). In particular, in Sec.3.2:
  - A closed-form algorithm for the three-point tangential scheme from [30] is derived using control inputs in the velocity-aligned frame;
  - The two-point radial scheme from [41] is extended to eccentric targets;

  - The two-point non-drifting algorithm from [51] is re-derived to obtain a ROE parametrization which is non-singular for zero eccentricities;

- Extension of guidance strategies from the literature (see Sec.3.3.2 and Sec.3.3.3) to eccentric cases using relative orbit C-elements to maintain passive safety;
- Definition of a novel finite state machine logic for rendezvous in Sec.3.3.1.

Chapter 2

Fundamentals

2.1 Relative Motion

2.1.1 Reference Frames

To delve into the discussion of relative motion and control between two spacecraft, it is important to first define the reference frames which will be used for absolute and relative state representation of the satellites.

Earth-Centered Inertial (ECI) frame

This coordinate frame is conventionally used to describe the orbital motion of a satellite around the Earth with respect to inertially fixed directions; it is fixed on the planet center of mass (assumed coincident with its geometric center) and is therefore only quasi-inertial due to the orbital motion of the Earth around the Sun. Its reference axes are defined as illustrated in Fig.2.1.1a:

- X_{ECI} points in the direction of the vernal equinox γ at the J2000.0 epoch [22].
- Z_{ECI} points in the direction of the north pole at the same reference epoch.
- Y_{ECI} completes the right-hand triad and lies on the mean equatorial plane at the reference epoch.

Within the context of the presented work, this frame is considered when integrating the absolute motion of each of the satellites by means of Newton's law of gravitation.

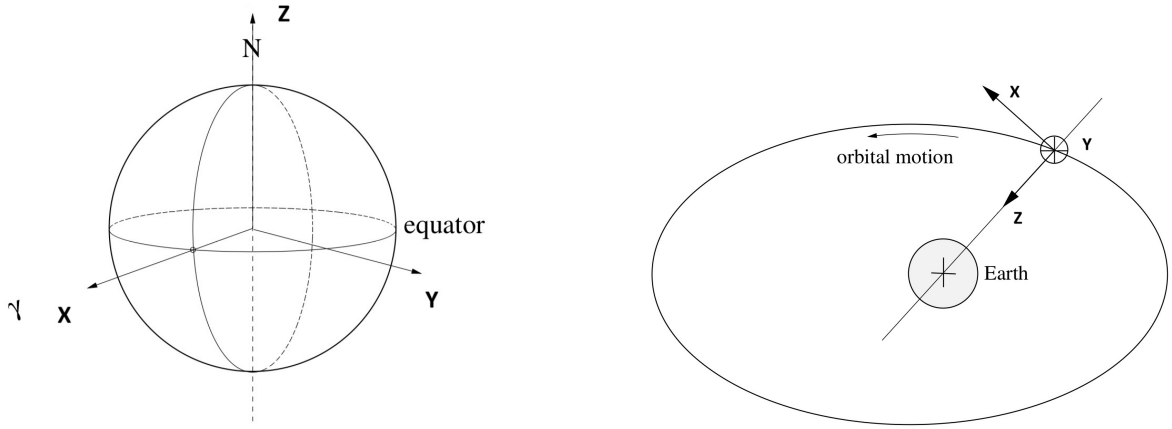

(a) ECI frame (b) LVLH frame

Figure 2.1.1: Reference frames [23]

Local-Vertical Local-Horizontal (LVLH) frame

This non-inertial coordinate frame is a faster moving reference which can be used to describe relative motions. It is centered on the center of mass of a spacecraft and its axes, shown in Fig.2.1.1b are defined as:

- Y_{LVLH} points in the opposite direction with respect to the orbit angular momentum vector. In the rendezvous literature it is often denoted as H-bar.
- Z_{LVLH} points "downwards" to the center of the Earth. In the rendezvous literature it is often denoted as R-bar.
- X_{LVLH} completes the right-hand triad and is aligned to the orbital velocity vector only on circular orbits. For this reason, it is often referred to as V-bar.

Different nomenclatures can be found in the rendezvous and formation flying literature referring to this coordinate frame, such as local orbital frame, Radial-Transverse-Normal (RTN) frame or Hill frame [60]. The last two cases typically refer to a frame in which $X_{RTN} = -Z_{LVLH}$, $Y_{RTN} = X_{LVLH}$ and $Z_{RTN} = -Y_{LVLH}$. In the presented work, this frame will be used as reference to express the relative motion of the chaser by fixing the origin of the axes on the target.

Tangential (TAN) frame

The tangential or flight path [52] reference frame is another local frame centered on the spacecraft center of mass which is rotated on the orbital frame with respect to the

discussed LVLH frame. In particular:

- the X_{TAN} axis is aligned with the orbital velocity of the target. This will be referred to as the tangential direction throughout the thesis.
- the Y_{TAN} stays the same as in the LVLH frame definition. This will be referred to as the normal direction throughout the thesis.
- the Z_{TAN} points approximately in the direction of the Earth, completing the right-handed triad. Although not aligned with the radial vector, this will be referred to as the radial direction throughout the thesis.

While this may seem trivial, the two frames coincide exactly in the case of circular orbits. What makes this reference interesting from the control point of view is that the normal and radial directions are orthogonal to the spacecraft velocity for any eccentricity of the orbit, and instantaneous velocity impulses along either of these two directions do not change the orbital energy, as it will be seen in the next sections.

Body frame

The orientation of the target spacecraft to be inspected within its own local rotating frame may be described using rigid body kinematics. The coordinate body frame $\mathcal{B}$

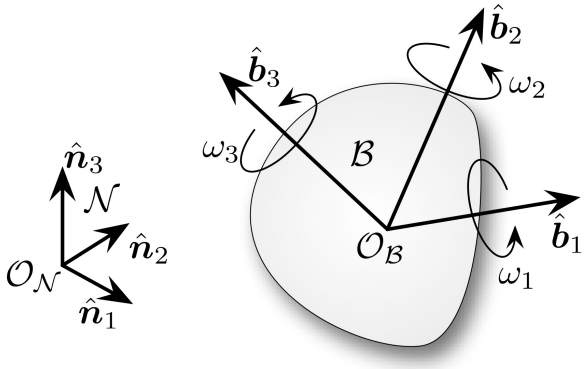

Figure 2.1.2: Body reference frame [35]

in Fig.2.1.2 is defined by its origin $\mathcal{O}$, fixed in the spacecraft center of mass and three orthogonal axes fixed to the non-deforming vehicle structure. The rotational motion of $\mathcal{B}$ with respect to an inertial frame $\mathcal{N}$ can be described through the angular velocity vector $\boldsymbol{\omega}$.

2.1.2 Keplerian Motion

Keplerian motion refers to the idealized orbital motion of a satellite body around a main point mass attractor assuming that only those two bodies are involved and no external disturbances are present. Moving from Newton's gravitational law with these same assumptions, the nonlinear second-order differential equation describing the motion of the satellite with position r relative to the planet is:

$$\ddot{\mathbf{r}} = -\frac{\mu}{r^3}\mathbf{r} \tag{2.1}$$

where μ is the gravitational constant of the planet. By integrating Eq.2.1 one can obtain the full state representation of the spacecraft in terms of position and velocity vectors in the ECI frame, given proper initial conditions. An alternative representation of the absolute state of the spacecraft is given by the set of Keplerian Orbital Elements (OE), which for unperturbed propagation are characterized by constant elements, except for the last, which identifies the position on the orbit:

- a is the orbit semi-major axis, which defines the orbital period;
- e is the orbit eccentricity;
- i is the orbit inclination;
- Ω is the orbit right ascension of the ascending node;
- ω is the orbit argument of perigee;
- f is the true anomaly, whereas M is the mean anomaly.

The routines to transform the spacecraft state between the cartesian ECI set and the OE set, as well as to transform between f and M are well documented in the literature (see [12]) and will not be reported here. The described set of OE is said to be "singular" because it becomes undefined in the cases of equatorial ($i = 0$) and circular ($e = 0$) orbits, for which the location of the line of nodes (identified by Ω) and the perigee (identified by ω) becomes ambiguous; a variety of "quasi-nonsingular" or "nonsingular" orbit elements sets that solve these problems can be alternatively adopted and can be found in the literature [2].

To propagate the motion of a satellite in the described conditions, it is sufficient to

solve for its mean anomaly M using Kepler's equation:

$$n \cdot (t - t_0) = M - M_0 \tag{2.2}$$

where n is the mean motion, defined as $\sqrt{\mu/a^3}$. Moreover, by using Eq.2.1 to express the orbital energy, it is possible to write the vis-viva (or energy) equation [60]:

$$-\frac{\mu}{2a} = \frac{v^2}{2} - \frac{\mu}{r} \tag{2.3}$$

from which it will be possible to infer that small and instantaneous velocity impulses in directions orthogonal to the flight path which do not modify the magnitude of v significantly do not change the orbit energy, hence the semi-major axis and period of the orbit ($P = 2\pi\sqrt{a^3/\mu}$) remain unchanged. This is a result which becomes clear within the context of the Gauss Variational Equations (GVE), treated in Sec.2.1.3.

2.1.3 Variational Equations

In the previous section it was stated that under ideal, unperturbed (Keplerian) conditions the introduced set of OE remains constant in time, except for the last element; such an assumption needs to be abandoned when facing real-world cases, where external perturbations (*e.g.*, asphericity of planets, atmospheric drag, solar pressure) are accounted for. To face this issue, one solution could be to simply integrate numerically Eq.2.1, adding on the right side known perturbative accelerations $\mathbf{a_d}$; such a method takes the name of Cowell's method, from the British mathematician who used it in 1909 to compute the orbit of Halley's Comet. When considering applications where these perturbative accelerations are orders of magnitude smaller than the central body gravitational pull, different approaches like perturbation methods are considered; these have in common the fact that only the equations describing the time evolution of the deviation from the two-body solution are sought [60]. This δ is a deviation defined between the actual perturbed orbit and a reference unperturbed orbit referred to as osculating, since at t_0 it coincides in position and velocity with the perturbed orbit[1]. One approach among these perturbation strategies is Encke's method [2], which derives a second-order differential equation of δ to be integrated over time

[1]This condition is defined "osculating condition".

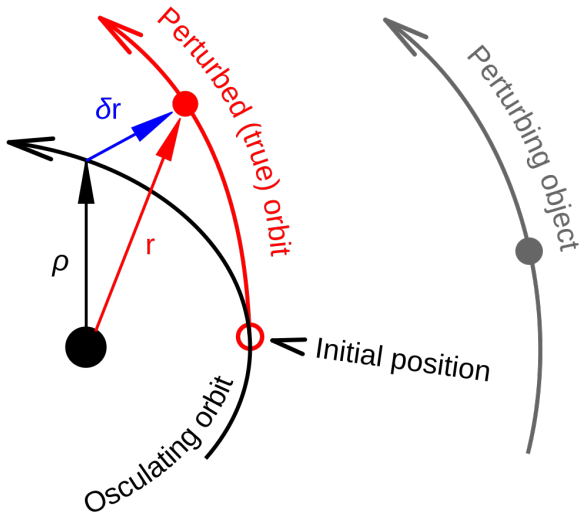

Figure 2.1.3: Osculating and perturbed orbit [67]

to obtain perturbed $\mathbf{r}(t)$ and $\dot{\mathbf{r}}(t)$. Another approach is to consider the alternative orbit representation vector $\mathbf{e}$ which uses the defined OE and continuously impose the osculating condition with the perturbed solution at each instant of time; the focus of the problem is then shifted to finding the time derivative of the osculating vector $\dot{\mathbf{e}}$. To this purpose, two methods to derive the variational, first-order equations can be used:

- Lagrangian Brackets [6], which lead to the development of Lagrange's planetary equations [2];
- Poisson Brackets, which lead to the development of the Gauss Variational Equations.

The second group of variational equations is particularly convenient when the external acceleration a_d is non-conservative[2], since one of the assumptions taken in the derivation using Lagrangian Brackets is the possibility to define a scalar disturbance potential which only depends on the position vector. Moreover, the disturbing acceleration can be mapped in whatever local orbit frame of choice; for convenience, the variational equations for the selected frame of OE with the disturbing acceleration expressed in a velocity-aligned frame taken from [2] are reported in the

[2]Many on-orbit disturbances, as well as control accelerations, fall within this definition.

following:

$$\begin{aligned}
\frac{da}{dt} &= \frac{2a^2 v}{\mu} a_v \\
\frac{de}{dt} &= \frac{1}{v}\left(\frac{r}{a}\sin f \cdot a_n + 2(e+\cos f)a_v\right) \\
\frac{di}{dt} &= \frac{r\cdot\cos(f+\omega)}{h} a_h \\
\frac{d\Omega}{dt} &= \frac{r\cdot\sin(f+\omega)}{h\cdot\sin i} a_h \\
\frac{d\omega}{dt} &= \frac{1}{ev}\left(-\left(2e+\frac{r}{a}\cos f\right)a_n + 2\sin f\cdot a_v\right) - \frac{r\sin(f+\omega)\cos i}{h\cdot\sin i} a_h \\
\frac{dM}{dt} &= n + \frac{b}{aev}\left(\frac{r}{a}\cos f\cdot a_n - 2\left(1+e^2\frac{r}{p}\right)\sin f\cdot a_v\right)
\end{aligned} \tag{2.4}$$

where the semi-latus rectum of the orbit $p = a\eta^2$, the semi-minor axis of the orbit $b = a\eta$ and the eccentricity factor $\eta = \sqrt{1-e^2}$ have been introduced. The acceleration components a_v, a_n and a_h are respectively expressed along the X_{TAN}, $-Z_{TAN}$ and $-Y_{TAN}$ directions (see Sec.2.1.1). It can be noticed that the first of Eq.2.4 confirms the physical intuition that only accelerations directed in the velocity direction change the osculating semi-major axis; moreover, ω, which defines the rotation of the orbit in its plane, is the only element which is influenced by accelerations in all directions. Lastly, by taking the last of Eq.2.4 and neglecting perturbations, one can see that after integration it reduces to Kepler's equation (see Eq.2.2).

The GVE represent one of the first building blocks necessary to develop the low-level guidance manoeuvring schemes to arbitrarily change the OE of the chaser, as it will be discussed in Sec.3.2.

2.1.4 Relative Orbit Equations of Motion

This section aims to provide a basic theoretical understanding of the relative motion equations and related assumptions which determine the relative unperturbed trajectories between the two considered spacecraft. The presented developments are mostly based on reference [60]. For the sake of readability, it is stated here that whenever a subscript is missing from a variable/vector, it is implied that this last is referring to the target spacecraft. Fig.2.1.4 illustrates the problem at hand: the inertial positions of the target and chaser spacecraft are respectively denoted as $\mathbf{r_T}$ and $\mathbf{r_C}$; the relative position of the chaser is expressed in the non-inertial, rotating RTN frame

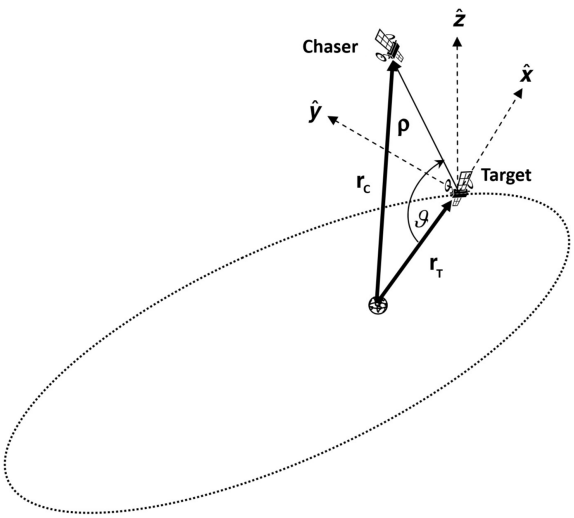

Figure 2.1.4: Relative motion of the chaser in the rotating RTN frame centered on the target [1]

of the target $\{\hat{x}, \hat{y}, \hat{z}\}$ (see Sec.2.1.1) as the vector $\boldsymbol{\rho}$. Using this notation, the chaser position vector may be written as:

$$\mathbf{r_C} = \mathbf{r_T} + \boldsymbol{\rho} = (r_T + x)\hat{x} + y\hat{y} + z\hat{z} \tag{2.5}$$

The transport theorem [68], recalled for convenience, relates the time derivative of a vector expressed in an inertial frame N to the derivative taken in a non-inertial one B:

$$\frac{^N d\mathbf{r}}{dt} = \frac{^B d\mathbf{r}}{dt} + \boldsymbol{\omega}_{B/N} \times \mathbf{r} \tag{2.6}$$

where $\boldsymbol{\omega}_{B/N}$ defines the angular velocity of the B frame with respect to the inertial frame N. In the unperturbed Keplerian motion, the non-inertial RTN frame rotates relatively to the ECI frame with an angular velocity equal to $\boldsymbol{\omega} = \dot{f}\hat{z}$; using this definition and Eq.2.6, it's possible to derive Eq.2.5 twice with respect to time and to obtain Eq.2.7:

$$\begin{aligned}\ddot{\mathbf{r}}_C = &(\ddot{r}_T + \ddot{x} - 2\dot{y}\dot{f} - \ddot{f}y - \dot{f}^2(r_T + x))\hat{x} \\ &+ (\ddot{y} + 2\dot{f}(\dot{r}_T + \dot{x}) + \ddot{f}(r_T + x) - \dot{f}^2 y)\hat{y} \\ &+ \ddot{z}\hat{z}\end{aligned} \tag{2.7}$$

Eq.2.7 can be further simplified using the following intuitions:

1. The angular momentum vector of the target orbit, defined as $\mathbf{h} = \mathbf{r} \times \dot{\mathbf{r}}$, which is

easily proven to be a constant using cross-product rules for unperturbed motion (see Eq.2.1), has its magnitude defined as: $h = r^2\dot{f}$. By exploiting the constancy of $\dot{h}$, the following expression is derived:

$$\ddot{f} = -2\frac{\dot{r}}{r}\dot{f} \tag{2.8}$$

2. The target position vector can also be written in the RTN frame as $\mathbf{r_T} = r_T\hat{x}$. By taking two time derivatives with respect to the inertial frame, the target orbit radius acceleration is expressed as:

$$\ddot{r}_T = r_T\dot{f}^2\left(1 - \frac{r_T}{p}\right) \tag{2.9}$$

By substituting Eq.2.8 and Eq.2.9 into Eq.2.7 and equating the result to the chaser equations of motion given by Eq.2.1, with the position vector as defined by Eq.2.5, the exact relative equations of motion given in Eq.2.10 can be obtained.

$$\begin{aligned} \ddot{x} - 2\dot{f}\left(\dot{y} - y\frac{\dot{r}}{r}\right) - x\dot{f}^2 - \frac{\mu}{r^2} &= -\frac{\mu}{r_C^3}(r + x) \\ \ddot{y} + 2\dot{f}\left(\dot{x} - x\frac{\dot{r}}{r}\right) - y\dot{f}^2 &= -\frac{\mu}{r_C^3}y \\ \ddot{z} &= -\frac{\mu}{r_C^3}z \end{aligned} \tag{2.10}$$

Eqs.2.10 describe the unperturbed relative motion of a chaser spacecraft relatively to a target for arbitrarily large separations between the two. However, the right-hand side of each equation is highly non-linear in r_C and an effort can be made to further simplify. In fact, if the relative distances x, y, z are much smaller than the orbit radius r_T, the norm of the chaser orbit radius may be re-written as:

$$r_C = \sqrt{(r_T + x)^2 + y^2 + z^2} = r_T\sqrt{1 + 2\frac{x}{r_T} + \frac{x^2 + y^2 + z^2}{r_T^2}} \approx r_T\sqrt{1 + 2\frac{x}{r_T}} \tag{2.11}$$

where a first-order linearization about the point $x = y = z = 0$ is applied. Such an approximation also allows to write the non-linear term as:

$$\frac{\mu}{r_C^3} \approx \frac{\mu}{r_T^3}\left(1 - 3\frac{x}{r_T}\right) = \frac{r}{p}\dot{f}^2\left(1 - 3\frac{x}{r_T}\right) \tag{2.12}$$

where the last identity is found by using the fact that $h = \sqrt{\mu p} = r^2 \dot{f}$. By substituting Eq.2.12 into Eq.2.10 the linearized relative equations of motions are found:

$$\begin{aligned} \ddot{x} - x\dot{f}^2\left(1 + 2\frac{r}{p}\right) - 2\dot{f}\left(\dot{y} - y\frac{\dot{r}}{r}\right) &= 0 \\ \ddot{y} + 2\dot{f}\left(\dot{x} - x\frac{\dot{r}}{r}\right) - y\dot{f}^2\left(1 - \frac{r}{p}\right) &= 0 \\ \ddot{z} + \frac{r}{p}\dot{f}^2 z &= 0 \end{aligned} \tag{2.13}$$

Since most of orbital rendezvous applications have a target spacecraft flying on a near-circular orbit (see RVD/B missions to space stations, or the most cluttered orbital regions calling for ADR in Fig.1.1.1) it is often convenient to further simplify Eq.2.13 by assuming a circular reference orbit, which entails that $e = 0$, $r = p$ and $\dot{f} = n = \sqrt{\mu/r^3}$, leading to the very simple form:

$$\begin{aligned} \ddot{x} - 2n\dot{y} - 3n^2 x &= 0 \\ \ddot{y} + 2n\dot{x} &= 0 \\ \ddot{z} + n^2 z &= 0 \end{aligned} \tag{2.14}$$

The set of Eq.2.14 is commonly known as the Clohessy-Wiltshire-Hill (CWH) equations, owing to the famous publication from the first two [11] as well as to the initial important contribution to the derivation from Hill [21]. The very simple form of the CWH equations allows to find closed-form solutions to the relative equations of motion and represents the major reason for their wide use in on-board rendezvous guidance systems [23], with flight heritage on the first manned missions (Gemini, Apollo and Space Shuttle programs [9][32]) as well as on the first autonomous technology demonstrations (XSS-10 [17], ETS-VII [38]). Upon integration of the differential Eqs.2.14, the following homogeneous analytical solution is found for the relative position components:

$$\begin{aligned} x(t) &= x_{off} && -A_0 \cos(nt - \alpha) \\ y(t) &= y_{off} - \frac{3}{2}ntx_{off} && +2A_0 \sin(nt - \alpha) \\ z(t) &= && B_0 \sin(nt - \beta) \end{aligned} \tag{2.15}$$

Where x_{off}, A_0, α, y_{off}, B_0 and β are introduced integration constants defined on the

initial conditions. The results in Eq.2.15 need further considerations in order to have a first clear geometrical insight into the free relative motion of the chaser with respect to the target:

- The out-of-plane motion along $\hat{z}$ is a simple harmonic oscillation of amplitude B_0 and phase β around the target orbit plane and was found to be completely decoupled from the in-plane equations of motion even before the introduction of the circular reference orbit assumption (see Eqs.2.13).

- The in-plane motion describes a 2-by-1 ellipse, with the semi-major axis aligned with the velocity direction $\hat{y}$. Both in-plane directions can be characterized by constant offsets, but only the radial x_{off} causes a secular growth in the other coordinate; a bounded relative orbit is obtained by setting x_{off} to zero, which in terms of initial conditions entails:

$$\dot{y_0} + 2nx_0 = 0 \tag{2.16}$$

It goes without saying that the model presented in Eqs.2.14 does not represent the arriving point of the rendezvous literature nor it embodies the ”best” relative motion description; an extensive variety of cartesian-state-based models has been developed since the 1960s, each characterized by a particular range of applicability (*e.g.*, eccentricity of the target, linearising assumption, modeled perturbation forces). Of particular interest for arbitrarily eccentric reference orbits are linear models which use the true anomaly instead of time as independent variable; a notable example is the development presented by Yamanaka and Ankersen in [72], which provided a linear propagation model which is currently considered state-of-the-art for Highly-Eccentric Orbit (HEO) and which has been used onboard the recently launched Proba-3, a formation flying mission of two spacecraft in a HEO which aims to perform Solar coronagraphy and formation manoeuvres in a region around apogee [49]. A comprehensive survey of the many available relative motion models is provided in [62], where a comparative assessment based on the dynamics models performances is also drawn based on specific test cases.

2.1.5 Relative Orbit Elements

In the previous section a closed-form analytical solution for the case of close satellites (for which the linearizing assumption holds) and circular target orbits was presented in the form of the CWH equations (see Eqs.2.15); such a solution was observed to depend on the set of relative Cartesian initial conditions through the introduced integration constants. A different approach to relative motion modelling is to use instead a relative state based on a set of six linear or nonlinear combinations of the chaser and target OE, generally defined as ROE. The immediate benefits of such a parametrization choice are the following:

- A ROE-based state is characterised by the slowly time-varying nature coming from the single absolute orbit elements, as seen in Sec.2.1.2;
- Orbit perturbations and control manoeuvres can be easily included using Lagrange's Planetary Equations and GVE, discussed in Sec.2.1.3.
- As it is the case for the single absolute orbits, a state representation based on Keplerian elements can offer greater geometrical insight into the shape of the relative orbit, as it will be shown in the following.

Many different ROE definitions can be found in the literature, each of which being characterised by specific advantages and drawbacks; the following paragraph aims to introduce the sets which are most relevant for the presented work.

Differential Orbit Elements

One common approach is to parametrise the relative orbit using differential orbit elements (sometimes denoted as orbit element differences), which are defined as in the following:

$$\Delta\mathbf{e} = \delta\mathbf{e} = \mathbf{e}_C - \mathbf{e}_T = [\delta a, \delta e, \delta i, \delta\Omega, \delta\omega, \delta M]^T \tag{2.17}$$

where $\mathbf{e}$ denotes the absolute OE of one spacecraft; it is to be specified that the definition of $\delta\mathbf{e}$ is not constrained specifically to the set of OE here considered, but it can be defined on any set of choice. The differential orbit element parametrization has been extensively adopted in formation flying modelling by Schaub, Alfriend and Gim [57][59][31] and has been used in design process and manoeuvre-planning of NASA's MMS [54] and CPOD [55] missions. It offers the following immediate insights into the relative orbit geometry:

- The relative semi-major axis δa allows to generalise the condition for bounded relative motion found in Eq.2.16 to any relative orbit size and eccentricity; in fact, periodic relative motion simply requires the orbits of the chaser and target to have the same orbit periods. This is simply enforced through the "energy matching" condition as:

$$\delta a = 0 \tag{2.18}$$

- The remaining elements of $\delta\mathbf{e}$ only control the shape of the relative orbit, in particular:

  - The element differences δi and $\delta\Omega$ influence the phase of the out-of-plane motion; for example, if only δi is non-zero then it can be expected that the relative orbit will have maximum out-of-plane separation when it crosses the northern or southermost regions.

  - The elements $\delta\omega$ and δM express the along-track separation between the two satellites, and remain constant for bounded relative orbits (Eq.2.18).

As introduced in Sec.2.1.2, the adopted absolute OE are singular for circular and equatorial orbits; for this reason, the relative state representation given in Eq.2.17 is also singular, in the sense that it is undefined when mapping it from another state parametrization.

Quasi-non-singular Relative Orbit Elements

A quasi-non-singular ROE set needs to be defined starting from absolute OE which are still defined for zero-eccentricity orbits. This is often solved by eliminating the singular elements ω, M and by defining the eccentricity vector components $e_x = e \cdot cos(\omega)$, $e_y = e \cdot sin(\omega)$ and the mean argument of latitude $u = \omega + M$. A new set of ROE may be defined as a non-linear combination of the defined quasi-non-singular elements of

chaser and target:

$$\delta\alpha = \begin{bmatrix} \delta a \\ \delta\lambda \\ \delta e_x \\ \delta e_y \\ \delta i_x \\ \delta i_y \end{bmatrix} = \begin{bmatrix} (a_C - a)/a \\ (u_C - u) + (\Omega_C - \Omega)\cos i \\ e_{x,C} - e_x \\ e_{y,C} - e_y \\ i_C - i \\ (\Omega_C - \Omega)\sin i \end{bmatrix} \tag{2.19}$$

where $\delta\lambda$ is defined as the relative mean longitude between the spacecraft; as it will be later shown the term $\delta\Omega cosi$ is introduced to decouple the relative mean longitude from out-of-plane motion. Note also that δa here is the same as the one defined for differential orbit elements, but it is normalised using the target semi-major axis; it is remarked here that elements without a subscript refer to the target spacecraft. This relative orbit representation is based on the definition of the relative eccentricity and inclination vectors, which can be expressed in polar notation as:

$$\delta\mathbf{e} = \delta e \begin{pmatrix} \cos\varphi \\ \sin\varphi \end{pmatrix}, \ \delta\mathbf{i} = \delta i \begin{pmatrix} \cos\vartheta \\ \sin\vartheta \end{pmatrix}, \tag{2.20}$$

One of the most interesting features of this ROE set is the fact that it is possible to demonstrate that its elements match the integration constants of the analytical solution to the CWH equations, reported in Eqs.2.15, as done in [16]:

$$\begin{aligned} x(t)/a &= \delta a && -\delta e \cdot \cos(u - \varphi) \\ y(t)/a &= \delta\lambda - \frac{3}{2}\delta a u && +2\delta e \cdot \sin(u - \varphi) \\ z(t)/a &= && \delta i \cdot \sin(u - \vartheta) \end{aligned} \tag{2.21}$$

Therefore, under the same assumptions which have been used to derive the CWH equations, the presented relative state parametrization in Eq.2.19 holds the following geometrical insight (as visualised in Fig.2.1.5):

- $a\delta a$ represents the offset of the center of the current relative orbit along the radial direction. As it could also be inferred from the discussion on orbit element differences, it also represents the relative drift between the orbits of chaser and target and a non-zero value causes the along track dimension to grow (or reduce)

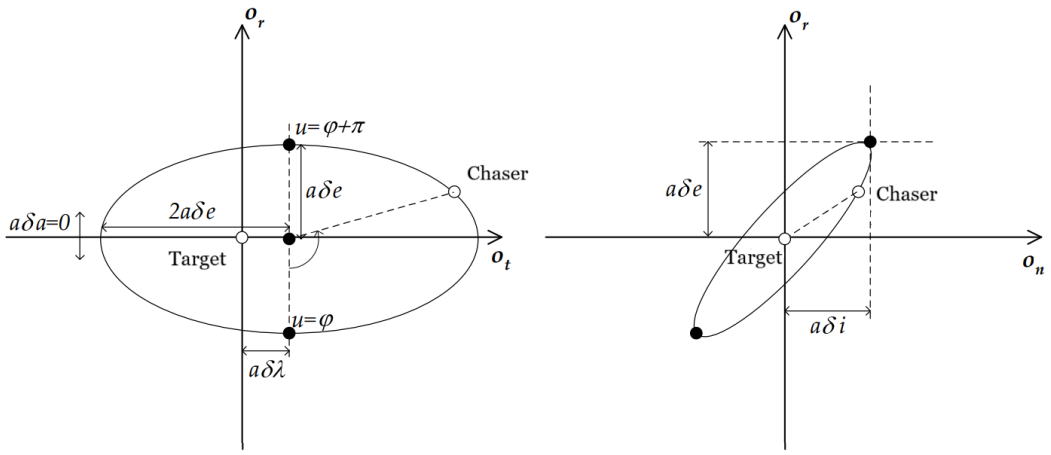

Figure 2.1.5: Relative motion of the chaser around a circular target projected on the RTN frame [13]

in a secular way.

- $a\delta\lambda$ represents the offset of the orbit in the along-track dimension.
- $a\delta e$ represents the in-plane relative orbit size, whereas $a\delta i$ represents the out-of-plane oscillation amplitude.
- The phases φ and ϑ of the relative eccentricity and inclination vectors are respectively termed relative perigee and relative ascending node, and they define the position of the chaser on the relative orbit at a given mean argument of latitude u of the target orbit.

Another key feature of this ROE set is the E/I-vector separation principle for collision avoidance, which was originally developed for the safe colocation of geostationary satellites [19]. The main idea is to avoid a collision hazard in the presence of along-track position uncertainties (generally much higher than in the other two directions) by ensuring a proper and consistent separation between the two spacecraft in the radial and normal directions. This can be obtained by imposing collinear[3] relative eccentricity and inclination vectors; in fact, having $\varphi = \vartheta$ ensures (see Eqs.2.21) maximum x when $z = 0$ and maximum z when $x = 0$. Fig.2.1.6 shows the relative orbit geometry of a chaser spacecraft around a circular target with $a\delta e = a\delta i = 4$ m and $a\delta a = a\delta\lambda = 0$ for varying E/I phasing angles ($\varphi - \vartheta$); as expected, the collinear condition between the E/I vectors yields the projection on the cross-track plane (RN-plane, in blue) which maintains maximum separation.

[3]Parallel or anti-parallel

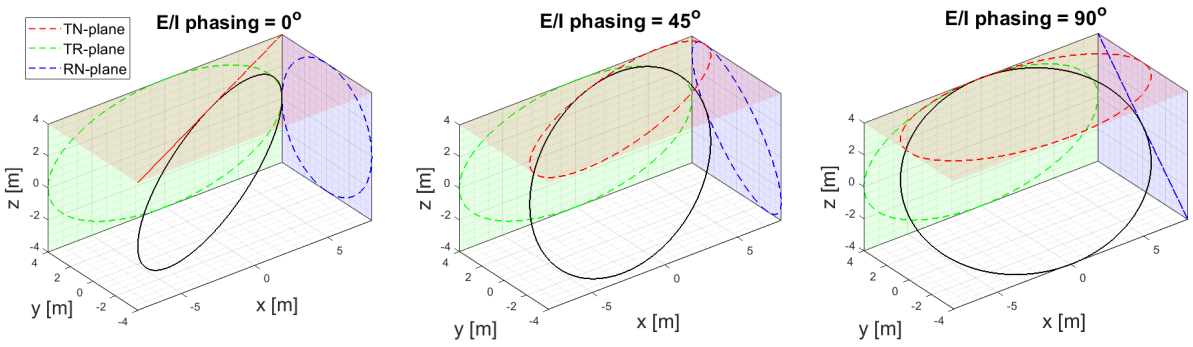

Figure 2.1.6: Relative LVLH orbit geometry for varying E/I phasing angles

Based on the founding assumptions used in the derivation of the CWH equations, this set of ROE has been often adopted since its introduction to rendezvous and formation flying missions in near-circular Low-Earth Orbit (LEO). The first practical application of the E/I-vector separation concept to a formation flying scenario was formalised in [43] as the basis for the implementation of the safe longitude swap manoeuvre for the two-satellite GRACE formation to compensate for the atomic oxygen wear on the two spacecraft. Subsequent missions and demonstrations which exploited this safety concept include the Autonomous Formation Flying System of TanDEM-X [15], the Spaceborne Autonomous Formation Flying Experiment within the PRISMA mission [14] and the AVANTI experiment [27] onboard the BIROS satellite of the FireBird mission. The main obvious shortcoming of the quasi-non-singular ROE set is the fact that the clear geometrical intuition on the relative orbit is progressively lost as the eccentricity of the target orbit increases.

Relative Orbit C-Elements

As illustrated in the previous section, the quasi-non-singular ROE set is a powerful representation which allows to easily design a relative orbit compliant with the PAS concept; in order to extend this capability to eccentric targets, a different set needs to be considered. The C-elements are a relative orbit element set which was intuitively found by Peters and Noomen [50] during the mathematical derivation of the linear cotangential transfer, which represents the generalization of the Hohmann transfer [12] from circular orbit rendezvous. Their definition is given as function of the

discussed orbit element differences:

$$\begin{aligned} C_1 &= \eta^2 \delta a - 2ae\delta e \\ C_2 &= e\delta p - p\delta e \\ C_3 &= -ep(\delta\omega + \cos i\delta\Omega) \\ C_4 &= a(\delta\omega + \cos i\delta\Omega + \eta^{-1}\delta M) \\ C_5 &= -p(\cos\omega\delta i + \sin i \cdot \sin\omega\delta\Omega) \\ C_6 &= p(\sin\omega\delta i - \sin i \cdot \cos\omega\delta\Omega) \end{aligned} \tag{2.22}$$

An immediate comparison to the previously introduced set can be drawn. The element C_1 provides a generalisation of the relative semi-major axis, the element C_4 is a scaled definition of the modified relative mean longitude $\delta\lambda_e$ (introduced in [53] to discuss control of the quasi-non-singular ROE in eccentric cases), whereas C_2, C_3 and C_5, C_6 respectively represent generalised relative eccentricity and inclination components. The key differences from the quasi-non-singular set are the following:

- The C-elements are dimensionalised with the semi-major axis a and the semi-latus rectum p.
- The in-plane element C_3 is also decoupled from out-of-plane motion using the term $cosi\delta\Omega$.

PAS-based relative orbit design using C-elements follows the same philosophy as the one illustrated in the previous section, which is that large uncertainty in the along track direction calls for safe separation in the cross-track plane of the target; the reference frame considered is however rotated from the LVLH to the presented TAN (velocity-aligned, see Sec.2.1.1). The reason for this is that the z coordinate of the LVLH frame (R-bar) is dependent on the relative mean anomaly δM, making the safety analysis along the z-axis dependent on the along-track position if the relative semimajor axis is non-zero [50]. Working in TAN frame therefore allows to retain the simplicity in the analysis by only considering two dimensions; the free motion along these is parametrized in the following way:

$$\begin{aligned} y_{TAN} &= \frac{1}{\rho}(C_5 \sin f - C_6 \cos f) \\ z_{TAN} &= -\frac{1}{\rho\theta}(C_1 + C_2 \cos f + C_3 \sin f) \end{aligned} \tag{2.23}$$

where the scaling factors $\rho = 1 + ecosf$ and $\theta = \sqrt{2\rho - \eta^2}$ govern the behaviour of the orbital radius and velocity, both non-constant on elliptic orbits. One can notice how Eqs.2.23 strike a resemblance with the equations along the z and x from Eqs.2.21, where circular motion was assumed. To generalise the relative E/I separation concept, the In-Plane (IP) and Out-Of-Plane (OOP) phase angles and dimensions are introduced:

$$\begin{aligned} \alpha &= \arctan(C_3/C_2), & \beta &= \arctan(C_6/C_5) \\ C_{IP} &= \sqrt{C_2^2 + C_3^2}, & C_{OOP} &= \sqrt{C_5^2 + C_6^2} \end{aligned} \tag{2.24}$$

The generalization of the safe orbit concept to the eccentric reference case is obtained by imposing collinearity between the generalised relative eccentricity vector (defined by magnitude C_{IP} and phase α) and the generalised relative inclination vector (defined by magnitude C_{OOP} and phase β). Fig.2.1.7a shows the comparison between relative orbit initialisation using different phasing angles for the E/I separation criterion formulated in the (quasi-non-singular) ROE set and the one formulated using C-elements considering an eccentric target orbit with $e = 0.5$ and same in-plane and out-of-plane sizes. It is easy to see that the latest method is able to consistently

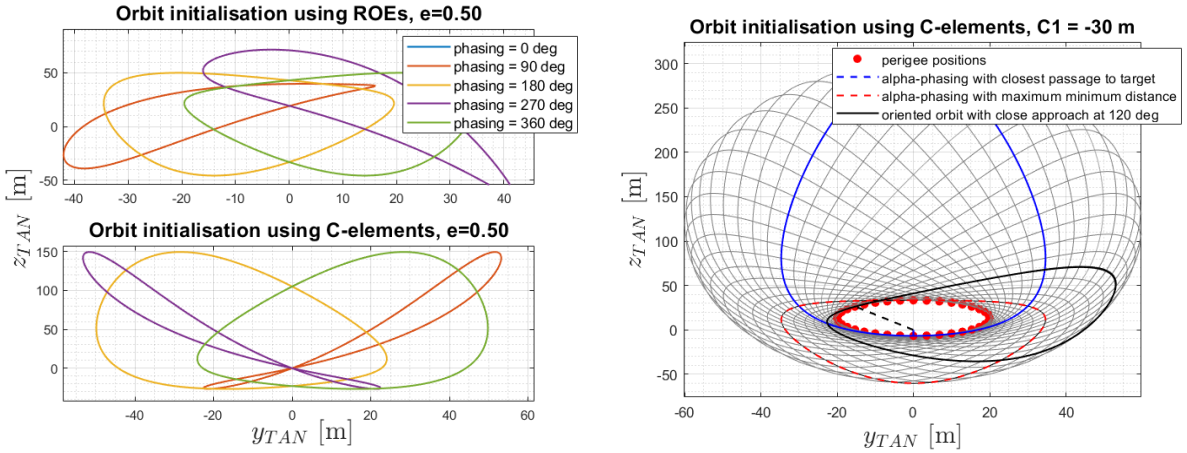

(a) Comparison of E/I separation concepts

(b) Safe trajectory family generated by α

Figure 2.1.7: Safe orbit initialisation using C-elements

extend the safety concept to high elliptical orbits, whereas the first loses its geometrical meaning as expected. Moreover, unlike the circular case, by imposing the generalised E/I collinearity condition and the relative orbit sizes one does not generate a unique relative orbit geometry but a family of trajectories lying on a quadric surface in the three-dimensional space [37] and oriented according to the single phasing of α (or β). To simplify the problem, safe sizing of the relative orbit can then be done by considering the inner boundary of the trajectory family; the locus of points forming the boundary

is defined by the perigee positions, where the y_{TAN} and z_{TAN} coordinates are scaled by the largest value of ρ and θ:

$$\begin{aligned} y_{TAN}^{IB} &= -\frac{C_{OOP}}{(1+e)}\sin(f-\alpha) \\ z_{TAN}^{IB} &= -\frac{(C_1 + C_{IP}\cdot\cos(f-\alpha))}{(1+e)^2} \end{aligned} \tag{2.25}$$

The generated trajectory family obtained by imposing the generalised safe E/I separation concept to a chaser orbiting a target with $e = 0.5$ is shown in Fig.2.1.7b; the lower boundary of the trajectory family as well as possible choices of single orbits based on different criteria are also shown. Eqs.2.25 provide a conservative way to safely size the relative orbit; as in the circular case, to have the chaser spiralling around the origin, the radial offset needs to be limited such that $|C_1| < C_{IP}$. On the other hand, to design drift-free trajectories (setting $\delta a = 0$ in Eqs.2.22), the new condition to impose is the following:

$$C_1 = \frac{2e}{1+e^2}C_2 \tag{2.26}$$

The linear mappings between the C-elements set and the quasi-non-singular ROE are provided in Appendix A, and will often be used throughout the presented work.

2.1.6 State Transition Matrices

A State Transition Matrix (STM) $\Phi(t, t_0)$ provides a linear, direct mapping from an initial state $\mathbf{x}(t_0)$ to a final state vector $\mathbf{x}(t)$:

$$\mathbf{x}(t) = \Phi(t_0, t)\cdot\mathbf{x}(t_0) \tag{2.27}$$

Mathematically, Φ can be seen as the sensitivity matrix of the current state to the initial conditions [60]. The STM for a dynamical system can be derived starting from its representation as a system of first-order equations:

$$\dot{\mathbf{x}} = A\mathbf{x} \tag{2.28}$$

where A is often referred to as the plant matrix of the system. For example, considering the derived CWH equations from Eqs.2.14, the plant matrix is easily defined as:

$$A^{CWH} = \begin{bmatrix} 0 & 0 & 0 & 1 & 0 & 0 \\ 0 & 0 & 0 & 0 & 1 & 0 \\ 0 & 0 & 0 & 0 & 0 & 1 \\ 3n^2 & 0 & 0 & 0 & 2n & 0 \\ 0 & 0 & 0 & -2n & 0 & 0 \\ 0 & 0 & -n^2 & 0 & 0 & 0 \end{bmatrix} \tag{2.29}$$

The CWH model is particularly convenient to derive a state transition matrix because its plant is characterised by constant coefficients ($n = const$ for circular motion of the target); in fact, it is possible to write the general solution of Eq.2.28 using the Taylor's series:

$$\mathbf{x}(t) = \left(I + \sum_{n=1}^{\infty} A^n \frac{(t-t_0)^2}{n!} \right) \mathbf{x}(t_0) \tag{2.30}$$

where the constancy of A was exploited to express $\frac{d^n \mathbf{x}(t)}{dt^n}|_{t_0} = A^n \mathbf{x}(t_0)$. The term between parentheses in Eq.2.30 is the STM describing the evolution of the dynamical system from t_0 to t, and can be expressed as the matrix exponential function of A:

$$\Phi(t_0, t) = e^{A \cdot (t - t_0)} \tag{2.31}$$

The expression of Φ for the CWH model can be found in Appendix A of [23]. In the general case, the derivation process of Φ is made more complicated by time-varying coefficients of the plant matrix A, as in the case of dynamic models using rectilinear coordinates and describing relative motion around arbitrarily eccentric target orbits.

General useful properties of the linear propagation through the STM include:

1. $\Phi(t_0, t_0) = I$
2. $\Phi(t_0, t_2) = \Phi(t_1, t_2)\Phi(t_0, t_1)$
3. $\Phi(t_0, t) = T^{-1}(t)\hat{\Phi}(t_0, t)T(t_0)$, where T is a linear transformation which maps the considered relative state representation to one identified by the $\hat{}$ symbol.

Based on what has been said so far, the relative state $\mathbf{x}$ to be propagated can be expressed by any of the desired representations discussed; moreover, as illustrated by

the comprehensive survey in [62] a great variety of propagation models accounting for diverse types of differential orbit perturbations and assumptions is available from the relevant literature. Of particular interest to the presented work are the dynamic models that are based on the illustrated quasi-non-singular ROE (the quasi-non-singular term will be omitted from here on for brevity), which have benefited from years of studies oriented towards the precise modelling and inclusion of on-orbit perturbation effects, like first-order J_2 (due to flattening of the Earth) and differential drag due to the residual atmosphere. Technology demonstrations like the one onboard the aforementioned PRISMA mission [14] even provided valuable flight data which helped refine these models to correct discrepancies with existing STMs [26].

The STM for the considered ROE takes on an extremely simple form by considering pure Keplerian motion; in fact, by definition, all the elements of Eq.2.19 are constant in the absence of perturbations, with the exception of $\delta\lambda$, which has the relative mean anomaly δM embedded through δu, non-constant in the case of relative drift δa. By taking the first order variation of the mean argument of latitude and using Eq.2.2 one obtains:

$$\delta u = \delta\omega + \delta(M_0 + n(t-t_0)) = \delta u_0 + \delta\left(\sqrt{\frac{\mu}{a^3}}(t-t_0)\right) = \delta u_0 - \frac{3}{2}n\delta a(t-t_0) \quad (2.32)$$

where δa is the normalised relative semi-major axis; note that no assumptions are made on the target eccentricity. The STM takes then the elementary form:

$$\Phi^{ROE}(t_0,t) = \begin{bmatrix} 1 & 0 & 0 & 0 & 0 & 0 \\ -\frac{3}{2}n(t-t_0) & 1 & 0 & 0 & 0 & 0 \\ 0 & 0 & 1 & 0 & 0 & 0 \\ 0 & 0 & 0 & 1 & 0 & 0 \\ 0 & 0 & 0 & 0 & 1 & 0 \\ 0 & 0 & 0 & 0 & 0 & 1 \end{bmatrix} \quad (2.33)$$

2.1.7 Modelling of Orbit Perturbations

The STM derived in Eq.2.33 can feasibly be used to compute impulsive manoeuvres to command the chaser, since these are typically characterised by propagation periods which are relatively short when compared to the timescales over which orbit

perturbations have a significant effect [52]. Nonetheless, the implementation of more advanced perturbed models remains extremely significant when long-term motion planning of the chaser is needed. Fig.2.1.8a illustrates the comparison of different

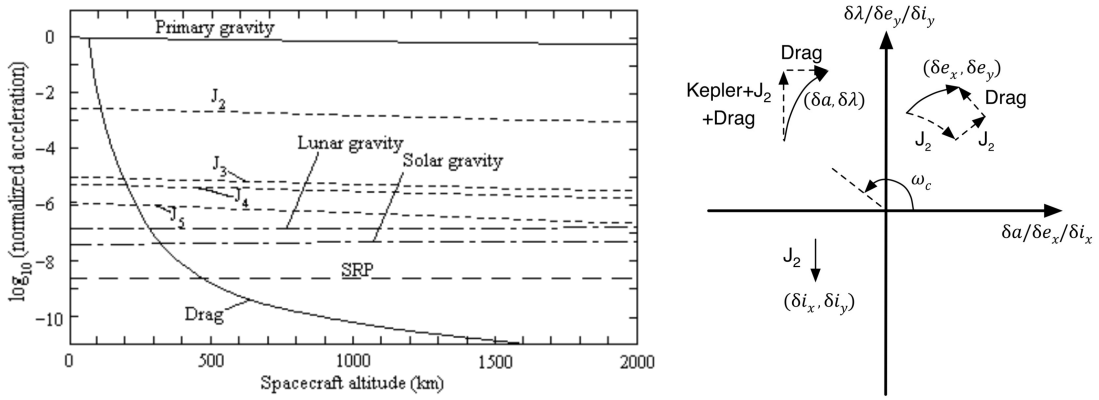

(a) Perturbing accelerations types [25] (b) Effects of J_2 and drag on ROE [39]

Figure 2.1.8: On-orbit perturbations

types of perturbing acceleration with varying spacecraft altitudes; it can be noticed that primary gravity, which is the only effect accounted for by pure Keplerian models, exerts an acceleration which is orders of magnitude higher than any other source. The deviation of Earth's gravity field from radial symmetry introduces additional terms to the gravitational potential among which the most prominent stem from the second-order zonal coefficient J_2, caused by Earth's flattening. Perturbation theories (see Sec.2.1.3) show that the equatorial bulge of the planet causes a secular regression of the line of nodes (Ω) as well as a rotation of the line of apsides (changing ω and M). A second prominent type of acceleration for LEO satellites is aerodynamic drag, which is caused by the interaction of the residual atmosphere molecules with the spacecraft surface, producing an acceleration which is predominantly anti-parallel to the velocity v of the vehicle relative to the incident stream:

$$\ddot{r} = \frac{1}{2}\rho v^2 C_D \frac{A}{m} \tag{2.34}$$

where ρ is the atmospheric density, C_D the drag coefficient, A the cross-sectional area and m the mass of the satellite. The term $B = C_D \frac{A}{m}$ is often denoted as the ballistic coefficient, and in close formations its difference ΔB over two satellites is the typical driving factor on the relative along-track acceleration [13]. It is quite intuitive that identical geometric design of two spacecraft can help minimize ΔB and differential drag effects; nevertheless, attitude manoeuvres of the chaser and

uncontrolled pointing on the target can still increase the differential factor quite significantly. Although more disturbances like third-body (from Moon and Sun) and solar radiation pressure have increasing influence on spacecraft motion at higher altitudes, the only differential perturbations considered within the current work are J_2 and drag.

Fig.2.1.8b provides a visualisation of four distinct relative motion modes produced by the combined mean effects of Keplerian motion and J_2 on the considered ROE set:

- A constant drift of $\delta\lambda$ due to both;
- A rotation of $\delta\mathbf{e}$ due to J_2;
- A secular drift of $\delta\mathbf{e}$, proportional to the target eccentricity vector (dotted line) and orthogonal to its direction due to J_2;
- A constant drift of δi_y due to J_2; it ought to be pointed out that this drift is proportional to the δi_x component, meaning that stationkeeping effort is reduced for configurations with $\delta i_x = 0$.

Differential drag on the other hand introduces the following effects:

- A linear drift of δa, which entails a quadratic drift in $\delta\lambda$ due to their coupling in Keplerian motion (see Eq.2.32);
- A linear drift of $\delta\mathbf{e}$ parallel to the phase angle of the target argument of perigee.

A state-of-the-art review of ROE-based linear propagation models valid for arbitrary eccentric orbits lead to the following implementation choices:

- In [28] Gaias et al. develop an analytical formulation which generalizes the first-order STM to include the secular effect of even zonal harmonics of the geopotential; in comparison to previous works ([13], [26], [39]) the STM derivation is obtained through the plant matrix without introducing any assumptions on the target eccentricity by expanding its mean orbit elements rather than its time derivatives. The STM Φ^{J_2} adopted to include only first-order J_2 secular effects is reported for convenience in Appendix B.
- In [39] Koenig et al. expand the modelling of time-varying differential drag in near-circular orbits from [26] and present a generalised framework which

allows to embed differential drag effects in the propagation of relative motion on arbitrarily eccentric orbits. To achieve this, two main approaches are proposed:

1. Using density-model-specific methods entails deriving an STM starting from a simple closed-form dynamic model for the drag perturbation (based on Eq.2.34), which is based on mathematical models estimating the relative ballistic coefficient ΔB as well as the local atmospheric density. Although a variety of detailed atmospheric models is available from the literature, the main evident shortcoming of this approach is related to unmodelled variations in the two variables which reduce accuracy of the propagation.

2. On the other hand using density-model-free methods asks for a state augmentation to incorporate the piece-wise constant[4] change rates of δa, δe_x and δe_y due to differential drag. The key idea is to estimate these derivatives on-board by using a simple linear regression on navigation data where the effects of J_2 have been filtered out. Naturally, the shortcoming of this approach is the fact that propagation accuracy is closely tied to the observability of the relative state.

For the current application, the second method was chosen to accommodate a more general architecture. Details on the STM as well as estimation process of the change rates are reported in Appendix B.

[4]This assumption can only be valid for a limited number of orbit periods of the target spacecraft.

Chapter 3

Methodology

3.1 Rendezvous Strategy Based on Safe Orbits

Having defined the necessary mathematical and theoretical background in the previous chapter, the autonomous guidance law can now be formulated starting from its higher-level approach strategy. As already introduced, a major requirement involved in the design of proximity approach trajectories is to ensure Passive-Abort Safety (PAS) in order to guarantee robustness against collisions in the event of off-nominal behaviour of either the navigation or the control system; to be compliant to such a constraint two types of approach trajectories are typically considered and are shown in Fig.3.1.1:

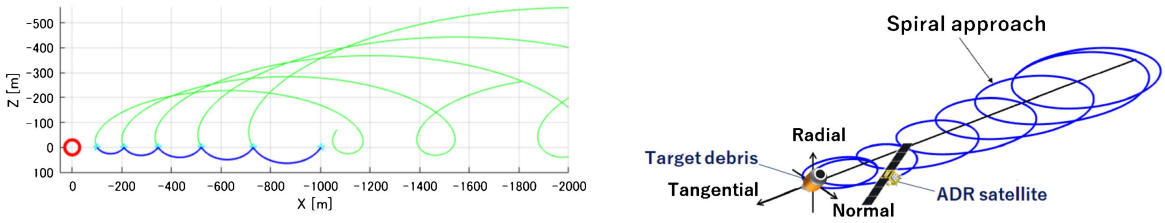

(a) V-bar hopping approach (b) Spiralling approach

Figure 3.1.1: PAS-compliant rendezvous strategies [56]

- The V-bar approach is based on a sequence of ”hopping” manoeuvres which progressively reduce the inter-satellite distance in the along-track direction. These two-point hops can be made inherently safe by either ensuring that the satellite goes away from the target after a failure to deliver the second firing (see green trajectories in Fig.3.1.1a) or by using drift-free coasting arcs through mostly

radial-oriented firings that return to the initial point in the same off-nominal case. This strategy has been extensively implemented in past manned missions like the Space Shuttle as well as automated rendezvous including the ATV cargo transfer vehicle to the ISS [23] as well as technology demonstrations like the ETS-VII [38].

- The spiral approach on the other hand relies on the relative E/I separation concept (introduced in Sec.2.1.5) to maintain a relative trajectory that spirals along the V-bar (see Fig.3.1.1b). The idea in this case is to gradually reduce the in-plane and out-of-plane sizes while maintaining a consistent distance from the origin on the cross-track (RN) plane. As shown in previous sections, this approach philosophy was inherited from formation flying applications and, according to the literature, seems to represent the main direction taken by past (AVANTI experiment from DLR [27], ELSA-d from Astroscale [24]) and future (ClearSpace-1 [64]) ADR missions to partially cooperative and non-cooperative targets.

In [56] Sasaki et al. present a comparison between these two approaches and discuss them in the context of non-cooperative rendezvous. Numerical simulations demonstrate how the first trajectory enables simpler satellite system design by limiting the variations in the Line-of-Sight vector to the target, allowing the chaser to maintain a fixed attitude with respect to the local orbit frame hence simplifying the management of visual-based relative navigation sensors. On the other hand, the second strategy greatly minimises fuel consumption (ΔV allocated budget) and can work with less reliable navigation solutions. To enable autonomous rendezvous operations and

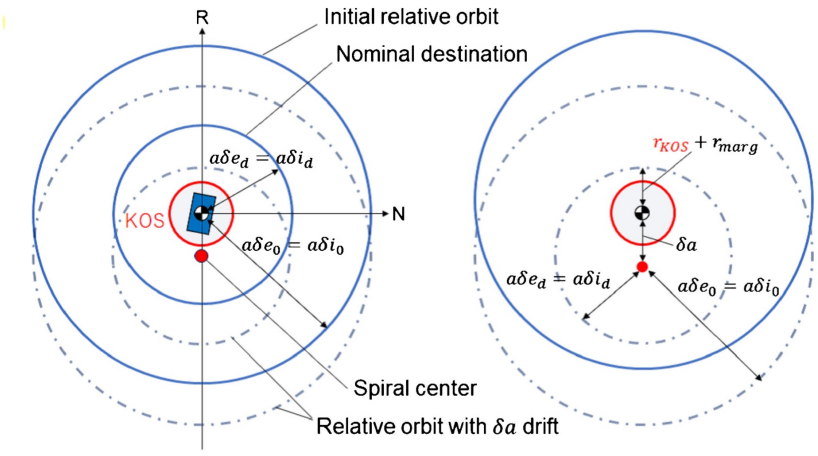

Figure 3.1.2: Safe spiralling approach design based on KOZ definition [56]

comply with typical requirements of ADR missions involving small chaser satellites, the second strategy is selected for the current work. As it will be later discussed, the concept of trajectory safety also involves the definition of either a spherical or ellipsoidal Keep-Out Zone (KOZ) (or KOS as shown in Fig.3.1.2) around the target spacecraft to ensure that the collision avoidance condition is robust with respect to uncertainties [3]. Fig.3.1.2 also shows that to guarantee PAS with respect to the KOZ on the cross-track (RN) plane care should be taken when selecting the relative drift $a\delta a$ between stationary orbits, as it has been shown in Sec.2.1.5 to shift the center of the relative orbit along the radial direction; the generalisation of such concept to non-circular targets has also been discussed and given in the form of the C_1 element of the relative orbit C-elements set.

3.2 Impulsive Manoeuvres for Arbitrary Elliptic Target Orbits Using Relative Orbit Elements

To realise the approach trajectories described in the previous section as well as to counteract the on-orbit disturbances discussed in Sec.2.1.7 a library of manoeuvres is developed in the following to arbitrarily change the ROE of the chaser spacecraft while approaching an arbitrarily eccentric target. Based on the definition of the STM matrix Φ (see Sec.2.1.6) and assuming impulsive manoeuvres which change the relative state $\mathbf{x}$ of the chaser, the general guidance linear equations for a single-point manoeuvre at t_1, with initial conditions given at t_0 can be written as:

$$\mathbf{x}_{t_1^+} = \Phi(t_0, t_1) \cdot \mathbf{x}_{t_0} + \mathcal{B}(t_1) \cdot \Delta\mathbf{v} \tag{3.1}$$

where the term $\Delta\mathbf{v}$ represents the instantaneous change in the relative velocity vector and $\mathcal{B}(t_1)$ represents the input matrix at time t_1 which maps the imposed variation of velocity into a change of the components of the relative state $\mathbf{x}$. Naturally, for relative Cartesian state representations, $\mathcal{B}$ takes on an extremely simple form but becomes less trivial for ROE parametrizations. The matrix $\mathcal{B}$ is derived hereafter according to the following choices:

1. In order to extend already existing manoeuvring schemes from circular rendezvous[1] to eccentric cases, $\mathbf{x}$ is parametrized using the quasi-non-singular

[1]Rendezvous to a target on a circular orbit.

ROE (see Sec.2.1.5), which will be referred to as $\delta\boldsymbol{\alpha}$ from now on.

2. As previously introduced, $\mathcal{B}$ and $\Delta\mathbf{v}$ will be expressed in the velocity-aligned TAN frame (see Sec.2.1.1); in this way, control on the relative semi-major axis δa is only possible along the tangential direction, generalising the circular formulation more effectively.

The Gauss Variational Equations provided in Eqs.2.4 have been initially derived as a tool to incorporate small perturbing accelerations, but it can also be used in the context of impulsive control by integrating them to obtain a direct map between a velocity increment $\Delta\mathbf{v}$ and a change in orbit elements, where the velocity step is defined from the input accelerations $\mathbf{a}$ as:

$$\Delta\mathbf{v} = \int_{\tau_0^-}^{\tau_0^+} \mathbf{a} \cdot d\tau \tag{3.2}$$

In practice, this translates the time derivatives in Eqs.2.4 into discrete variations of the elements. By substituting the GVE into the definition of the ROE in Eq.2.19 and by considering constant orbit elements of the target (not being manoeuvred), the following equations are obtained:

$$\begin{aligned}
\Delta\delta a &= \frac{2av}{\mu}\Delta v_v \\
\Delta\delta\lambda &= \left(\frac{2\sin f}{v}\sqrt{\frac{1-\eta}{1+\eta}} - \frac{2re\eta\sin f}{vp}\right)\Delta v_v + \left(-\frac{2}{v} - \frac{r\cos f}{va}\sqrt{\frac{1-\eta}{1+\eta}}\right)\Delta v_n \\
\Delta\delta e_x &= \left(\frac{2e\cos\omega}{v} + \frac{2}{v}\cos(\omega+f)\right)\Delta v_v + \left(\frac{r}{va}\sin(\omega+f) + \frac{2e\sin\omega}{v}\right)\Delta v_n \\
&\quad + \left(\frac{e\sin\omega\cdot r\sin(f+\omega)\cos i}{h\sin i}\right)\Delta v_h \\
\Delta\delta e_y &= \left(\frac{2e\sin\omega}{v} + \frac{2}{v}\sin(\omega+f)\right)\Delta v_v + \left(-\frac{r}{va}\cos(\omega+f) - \frac{2e\cos\omega}{v}\right)\Delta v_n \\
&\quad + \left(-\frac{e\cos\omega\cdot r\sin(f+\omega)\cos i}{h\sin i}\right)\Delta v_h \\
\Delta\delta i_x &= \left(\frac{r\cos(f+\omega)}{h}\right)\Delta v_h \\
\Delta\delta i_y &= \left(\frac{r\sin(f+\omega)}{h}\right)\Delta v_h
\end{aligned} \tag{3.3}$$

where the input $\Delta\mathbf{v}$ is defined in the same frame as the accelerations in Eqs.2.4; the complete $\mathcal{B}$ matrix expressed in the actual TAN frame is reported in Appendix C. Main observations regarding the derivation of Eqs.3.3 are that:

- It has been carried out under the linearizing assumption that the absolute orbit elements of the target are equivalent to those of the chaser when computing the single terms of $\mathcal{B}$;
- It should also be noted that the ROE set is defined in practice starting from mean orbit elements[2], whereas the GVE express the instantaneous time derivatives of the osculating orbit elements ($\frac{d\boldsymbol{\alpha}^{OSC}}{dt} = \Gamma(\alpha^{OSC})\mathbf{u}$). Strictly, this would lead the time derivatives of the mean elements to be defined as $\frac{d\boldsymbol{\alpha}^{MEAN}}{dt} = \frac{\partial\alpha^{MEAN}}{\partial\alpha^{OSC}}\Gamma(\alpha^{OSC})\mathbf{u}$. However, according to [58] the sensitivity matrix $\frac{\partial\alpha^{MEAN}}{\partial\alpha^{OSC}}$ is essentially the identity matrix with off-diagonal terms being of order of J_2 or smaller if the osculating to mean transformation is obtained using the popular first order truncation of Brouwer's (see in Appendix F of [60]). Thus, as a first approximation Eqs.3.3 can also be feasibly used to command mean relative orbit elements.
- It is valid for arbitrary eccentricities of the target, as no circularizing assumptions on e have been introduced. Still, Eqs.3.3 are not valid for equatorial orbits ($i = 0$), owing to the singularity of the original ROE set.

On the other hand, the derived $\mathcal{B}_{TAN}$ matrix highlights some interesting aspects:

- As expected, the relative semi-major axis is only changed using tangential firings and is decoupled from the other two directions;
- Without the approximation of near-circular target, the in-plane control problem (through δe_x and δe_y) is coupled to the out-of-plane impulses (Δv_h); such a coupling is amplified for more eccentric reference orbits, and it is inherent to the definition of the ROE.
- The out-of-plane elements $\delta i_x, \delta i_y$ are instead completely de-coupled from in-plane firings.

The derived input matrix can now be used to build closed form manoeuvring schemes which are suitable for on-board implementation, and are discussed in the next sections. Moreover, each developed manoeuvring scheme is validated using a pre-existing department's linear propagation function for relative motion based on the unperturbed Yamanaka-Ankersen STM [72]; the results produced in the relative Cartesian frame are then linearly mapped to the ROE set to analyze their time evolution.

[2]Transformed set of orbit elements which excludes short and long period oscillations due to J_2.

3.2.1 Single-Point Manoeuvres

In the current treatment, single-point manoeuvres refer to impulsive control schemes which are executed at a single anomaly on the reference orbit. The objectives of this class of manoeuvres include:

- Control of the shape of the relative orbit by means of the relative eccentricity $\delta\mathbf{e}$ and inclination $\delta\mathbf{i}$.
- Control of the drift of the relative orbit through δa.

It should be highlighted that mathematically a single-point scheme can provide complete control on the Out-Of-Plane (OOP) motion (two desired variations and two unknowns[3]) but the same cannot be achieved for the IP motion, which is characterised by four elements.

Out-of-plane Control

OOP control is achieved by commanding the relative inclination components of the chaser satellite. From Eqs.3.3 one can see that a single firing in the OOP direction is sufficient to achieve a desired change in both components. By defining the true argument of latitude of the manoeuvre as $\nu_{man} = f_{man} + \omega$, the location of the firing can be found by dividing the equation for $\Delta\delta i_y$ by the one for $\Delta\delta i_x$:

$$\nu_{man} = \arctan(\Delta\delta i_y, \Delta\delta i_x) \tag{3.4}$$

whereas the magnitude of the firing can be found by taking the squared sum of the two equations and defining $r = p/(1 + e\cos f)$ [4]:

$$\Delta v_Y = -\sqrt{\frac{\mu}{a}}\frac{1 + e\cos f_{man}}{\eta}||\Delta\delta\mathbf{i}|| \tag{3.5}$$

where Y refers to the OOP direction in the TAN frame and $||\Delta\delta\mathbf{i}|| = \sqrt{\Delta\delta i_x^2 + \Delta\delta i_y^2}$. Since the TAN and LVLH (or RTN) frames share the same OOP direction, the derived Eqs.3.4, 3.5 can also be found in Eq.(39) of [10] with a sign change. Tab.3.2.1 presents the initial and final conditions used to test the manoeuvre in the linear propagator, which takes as input a guidance Δv table specifying firing time (computed through

[3] Manoeuvre location and amplitude of OOP firing.
[4] Conic equation from Keplerian motion.

Table 3.2.1: Initial and final data for OOP single-point manoeuvre test

a [km]	e [-]	i [^{o}]	Ω [^{o}]	ω [^{o}]	f_0 [^{o}]
9000	0.2	40	45	100	40

ROE [m]	$a\delta a$	$a\delta\lambda$	$a\delta e_x$	$a\delta e_y$	$a\delta i_x$	$a\delta i_y$
Initial	-4	-500	0	-40	30	0
Aimed	-	-	-	-	0	20

Kepler's law from f_{man}, Eq.2.2) and x, y, z components of the velocity change. The results of the propagation are plotted in the target LVLH frame in Fig.3.2.1; on the right side, the in-plane view on x and z is reported and, as expected, it can be noticed that the OOP firing yields no effect on the trajectory along these components. Because the

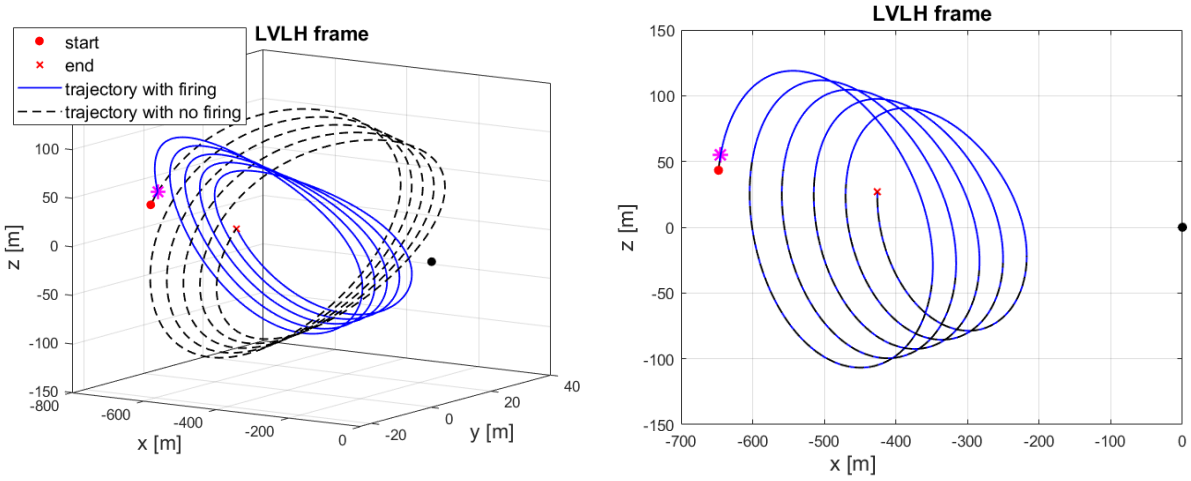

Figure 3.2.1: OOP manoeuvre results with linear propagation, 5 orbit periods

projection of the trajectory on the $x-z$ plane does not change, one can also observe on the left plot of Fig.3.2.1 that the trajectory with firing intersects the original one after an integer number of orbital periods from the firing point. These intersections therefore represent the manoeuvring anomalies ν_{man} that can be used to move from one orbit to the other using the single-point firing. Fig.3.2.2 reports the linear propagation results in the space of the controlled ROE; geometrically, ν_{man} is the angle which identifies the direction of the desired variation of the $\Delta\delta\mathbf{i}$ vector. It is also intuitive to understand that there are actually two opportunities per orbit allowing to move between the two relative orbits, which can be termed as relative ascending and descending nodes of the initial/final orbits. Moreover:

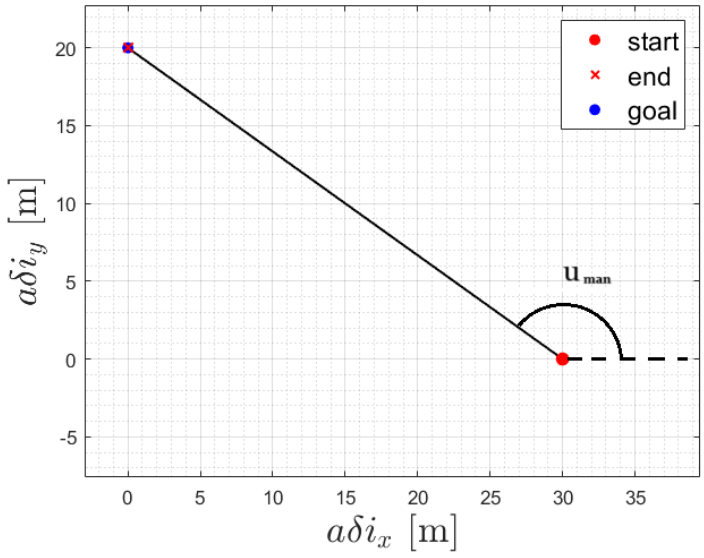

Figure 3.2.2: OOP manoeuvre results in the $\delta i_x/\delta i_y$ phase plane

- The two nodes are separated by half orbit period;
- If one fires at the relative descending node, the change in velocity Δv shall be delivered in the opposite direction. This is a result which can be easily understood by observing Fig.3.2.2, where $\nu_{man}^{desc} = \nu_{man}^{asc} + \pi$, which identifies the direction of the variation of $\Delta\delta\mathbf{i}$, would cause the firing to move the final point in the opposite direction with respect to the aimed state.
- As can be noticed from Eq.3.5, in the eccentric target case the two nodes yield different costs for the manoeuvre, meaning that the choice of either one could be based alternatively on timing or fuel minimization requirements.

To prioritize reactivity of the guidance software, the developed function picks the closest node to minimise the manoeuvre execution time; in the presented test case, the initial argument of latitude is $\nu_0 = 140^o$, the manoeuvre one is at $\nu_{man} \approx 146.31^o$.

In-Plane Shape Control

As introduced, the in-plane problem is more complex owing to the number of variables to be controlled, doubled with respect to the OOP case. Nevertheless, by simplifying the problem to only control the relative eccentricity components using a single radial firing, which does not affect the relative drift, a similar procedure to the $\Delta\delta\mathbf{i}$ control may be followed; in fact, the true anomaly at which the firing needs to be delivered can

once again be computed by taking the ratio of the related equations from Eqs.3.3:

$$\frac{\Delta\delta e_x}{\Delta\delta e_y} = -\frac{\frac{r}{va}\sin(\omega + f_{man}) + \frac{2e\sin\omega}{v}}{\frac{r}{va}\cos(\omega + f_{man}) + \frac{2e\cos\omega}{v}} \tag{3.6}$$

The solution is obviously less trivial in the non-circular case; still, by re-arranging Eq.3.6 as $K_1\cos f + K_2\sin f = K_3$, the two potential locations of the manoeuvre can be computed using the auxiliary angle method:

$$\begin{gathered} f_{man} = \arccos\left(\frac{K_3}{R}\right) + \alpha, \qquad f'_{man} = 2\pi - \arccos\left(\frac{K_3}{R}\right) + \alpha \\ C = \frac{\Delta\delta e_x}{\Delta\delta e_y}, \qquad K_1 = C\frac{p}{a}\cos\omega + 2Ce^2\cos\omega + \frac{p}{a}\sin\omega + 2e^2\sin\omega, \\ K_2 = -C\frac{p}{a}\sin\omega + \frac{p}{a}\cos\omega, \qquad K_3 = -2Ce\cos\omega - 2e\sin\omega, \qquad R = \sqrt{K_1^2 + K_2^2} \end{gathered} \tag{3.7}$$

whereas the magnitude of the radial firing is easily found by taking the squared sum of the two relevant equations:

$$\Delta v_z = -||\Delta\delta\mathbf{e}||\frac{va\eta^2}{r(e^2 + 2e\cos f_{man} + 1)} \tag{3.8}$$

where $||\Delta\delta\mathbf{e}|| = \sqrt{\Delta\delta e_x^2 + \Delta\delta e_y^2}$. The manoeuvre is validated using the linear propagator with data reported in Tab.3.2.2. The LVLH trajectory resulting from the

Table 3.2.2: Initial and final data for IP single-point manoeuvre test

a [km]	e [-]	i [^{o}]	Ω [^{o}]	ω [^{o}]	f_0 [^{o}]
18348	0.5	40	45	100	100

ROE [m]	$a\delta a$	$a\delta\lambda$	$a\delta e_x$	$a\delta e_y$	$a\delta i_x$	$a\delta i_y$
Initial	0	-4000	-200	150	0	200
Aimed	-	-	0	-300	-	-

linear propagator is reported in Fig.3.2.3, whereas the time evolution of the in-plane ROE is illustrated in Fig.3.2.4. Once again, a single pulse manoeuvre is able to achieve the desired change in the components of the relative eccentricity vector, and the developed function picks the closest manoeuvring anomaly between the computed f_{man} and f'_{man}; moreover, it can be observed from Fig.3.2.3 that the initial and final orbits are both stationary hence the relative drift has not been modified. This is also confirmed

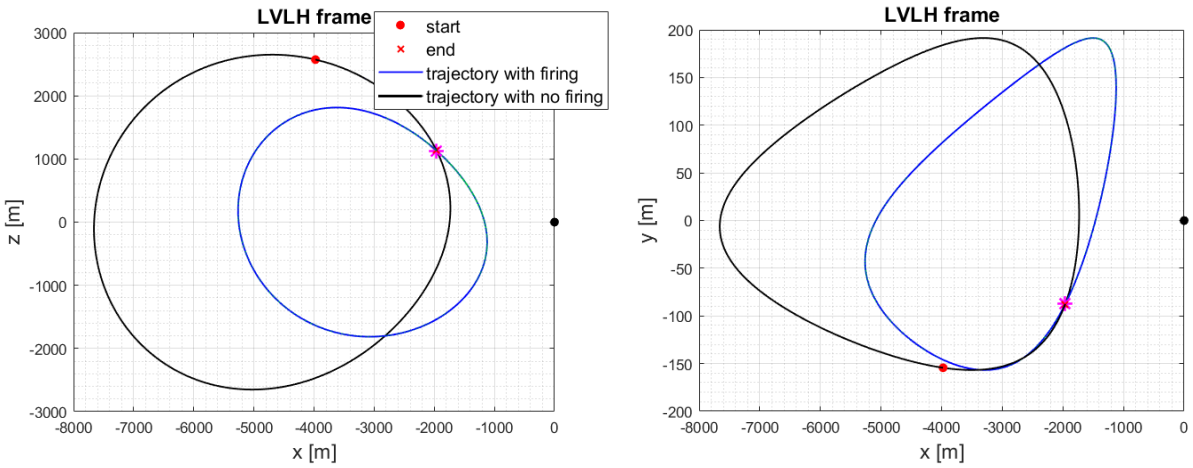

Figure 3.2.3: IP manoeuvre results with linear propagation, 5 orbit periods

by the time evolution of $a\delta a$ showcased in Fig.3.2.4, which is only ruled by linearisation errors on δa. A further point to be highlighted is the influence of the radial firing on the relative mean longitude $\delta\lambda$, which determines the along-track position of the relative orbit. In fact, in the selected test case the large manoeuvre required for in-plane phasing moves the chaser forward with respect to the original position; one way to cope with this side effect is to select the one anomaly between the two computed which increases the absolute value of $\delta\lambda$ rather than reducing it. For the current application

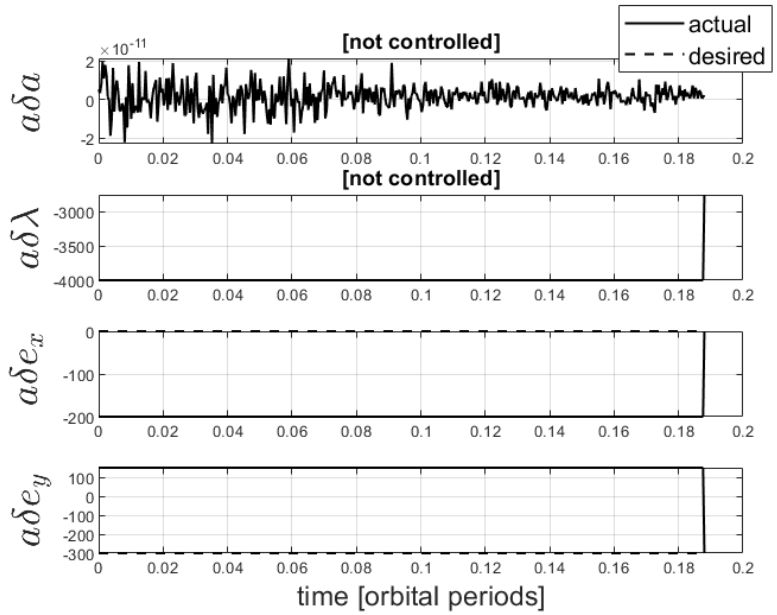

Figure 3.2.4: IP manoeuvre results mapped to ROE over time

higher priority is once again given to reactivity of the control, since the single-point manoeuvres used to correct $\Delta\delta\mathbf{e}$ will only be employed for small phasing manoeuvres and consequently small movements on the along-track axis are considered negligible

as long as PAS is guaranteed. A point which deserves considerably more attention is the observed coupling between OOP firings and undesired variations on δe_x and δe_y shown in Eq.3.3; such an effect becomes problematic when the autonomous guidance schedules a relative orbit resizing in both the IP and OOP dimensions. To account for this, one solution is to express the OOP change in velocity from the last of Eqs.3.3 as:

$$\Delta v_h = \frac{h}{r \sin(f+\omega)} \Delta \delta i_y \tag{3.9}$$

The actual required variations on the relative eccentricity components, accounting for thean coupling effect produced by an OOP manoeuvre, become:

$$\begin{aligned} \Delta \delta e_x^{actual} &= \Delta \delta e_x^{des} - \frac{e \sin \omega}{\tan i} \Delta \delta i_y \\ \Delta \delta e_y^{actual} &= \Delta \delta e_y^{des} + \frac{e \cos \omega}{\tan i} \Delta \delta i_y \end{aligned} \tag{3.10}$$

As said, this compensation scheme can be implemented in practice to cope with concurrent relative E/I separation corrections on both IP and OOP dimensions and is also valid for multiple-point manoeuvres. This method is validated using the same

Table 3.2.3: Aimed ROE for OOP precompensation test

ROE [m]	$a\delta a$	$a\delta\lambda$	$a\delta e_x$	$a\delta e_y$	$a\delta i_x$	$a\delta i_y$
Initial	0	-4000	-200	150	0	200
Aimed	-	-	0	-300	**40**	**150**

absolute orbit elements as Tab.3.2.2, but the final ROE are defined in Tab.3.2.3. The results of the linear propagation obtained by calling both manoeuvring functions described so far and by using the described compensation scheme in Eqs.3.10 are shown in Fig.3.2.5. As it can be noticed, the precompensation allows to precisely account for the deviation of $\Delta\delta\mathbf{e}$ caused by the OOP firing (which is visualised as the second smaller jump in Fig.3.2.5), successfully reaching the desired point in the phase plot. It should be noted that the same results would have been obtained if the OOP manoeuvre had been executed first, leaving to the on-board guidance the freedom to choose to execute the IP manoeuvre at either the f_{man} or f'_{man} anomaly.

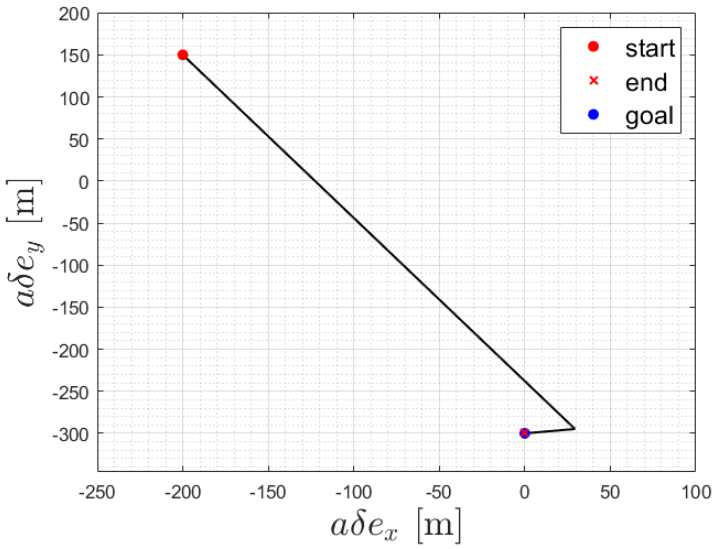

Figure 3.2.5: IP manoeuvre results in $\delta e_x/\delta e_y$ space using OOP precompensation

Relative Drift Control

To realise the rendezvous strategy described in Sec.3.1 a control on the relative drift of the travelling orbit is also needed. As shown by Eqs.3.3, a single tangential impulse at any point of the orbit can be used; however, since tangential manoeuvres also yield an effect on the other ROE, the firing anomaly can be selected according to different criteria:

- To minimise fuel expenditure for a given $\Delta\delta a$ the firing should be delivered where the orbital velocity v is the highest, which is at the target perigee.

- To minimise or partially control the effect that the firing would have on the other ROE the anomaly can be chosen to minimise selected elements of the $\mathcal{B}$ matrix.

As said, in the selected spiralling approach it is crucial to have the projection on the cross-track plane winding around the origin with some margin, typically specified by the KOZ size (see Fig.3.1.2). To enforce PAS of the approach, the second strategy is followed here. In particular, the true anomaly of the firing is chosen in such a way to always enlarge the relative orbit in-plane size, which is described by the squared sum of δe_x and δe_y. Using the elements $\mathcal{B}_{31}^{TAN}$ and $\mathcal{B}_{41}^{TAN}$ from the input matrix in Appendix

C, this means selecting an anomaly that satisfies both of the following equations:

$$\begin{cases} \text{sign}(\Delta\delta a) \cdot \text{sign}(\delta e_x) \cdot (A\cos f - B\sin f + Ae) > 0 \\ \text{sign}(\Delta\delta a) \cdot \text{sign}(\delta e_y) \cdot (B\cos f + A\sin f + Be) > 0 \end{cases} \tag{3.11}$$

$$A = \cos\omega \qquad B = \sin\omega$$

Once the firing anomaly is picked, v can be computed and the required change of velocity is simply derived by inverting the first of Eqs.3.3. Drift control is demonstrated using linear propagation for the "braking" ($a\delta a$ from -50 to 0) and "accelerating" ($a\delta a$ from 0 to 50) cases using the data reported in Tab.3.2.4. The results of the

Table 3.2.4: Initial and final data for drift control, single-point manoeuvre test

a [km]	e [-]	i [^{o}]	Ω [^{o}]	ω [^{o}]	f_0 [^{o}]
17000	0.01	10	50	220	50

ROE [m]	$a\delta a$	$a\delta\lambda$	$a\delta e_x$	$a\delta e_y$	$a\delta i_x$	$a\delta i_y$
Initial	**-50 / 0**	400	10	190	0	100
Aimed	**0 / 50**	-	-	-	-	-

trajectory propagation in the LVLH frame are reported in Fig.3.2.6. On the left side, the

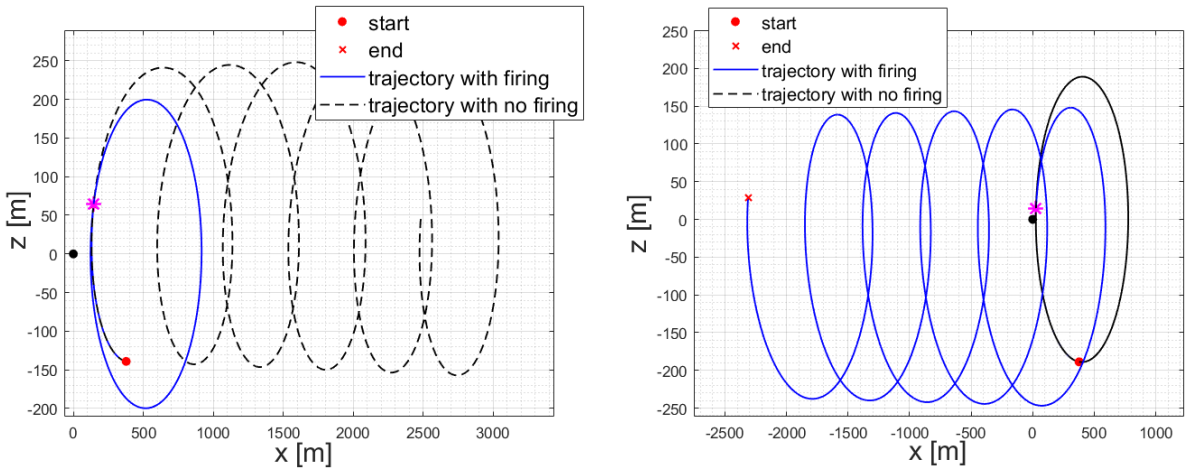

(a) Braking test case

(b) Accelerating test case

Figure 3.2.6: Drift control manoeuvre results with linear propagation, 5 orbit periods

manoeuvre is called to stop a trajectory which is drifting away from the target, whereas on the right side drift is commanded to initiate a spiralling motion around the target position.

3.2.2 Multiple-Point Manoeuvres

The previous section showed that a single firing positioned either at the relative ascending or descending node between the initial and aimed relative orbits is enough to grant full controllability of the OOP motion. On the other hand, the in-plane problem parametrised by δa, $\delta\lambda$, δe_x and δe_y (or the synchronised control of all ROE) requires at least two distinct firing points to achieve full controllability. Reference [30] provides a comprehensive survey on possible in-plane control schemes for near-circular target orbits obtained with either two or three distinct firings, investigating their cost, type of solution (analytical or numerical) and predictability, an important parameter for the deterministic autonomy of the guidance law. The idea of the aforementioned review is to investigate different manoeuvring schemes by changing the type of firing direction (radial, tangential or both) and constraining the problem using different manoeuvre locations and desired end conditions. The main guidelines presented from the results in the paper are the following:

- The two-point manoeuvre option generally requires to be solved through a numerical method with proper initial conditions; moreover, the schemes characterised by an analytical solution only apply to specific scenarios and employ radial firings, implying that only a fuel-suboptimal cost can be achieved.
- On the other hand, triple-tangential manoeuvring schemes allow finding multiple analytical (like ID: $\nexists_{12}$ in the paper) or semi-analytical (like ID: $\nexists_{13}$) solutions to achieve whatever aimed final ROE set.

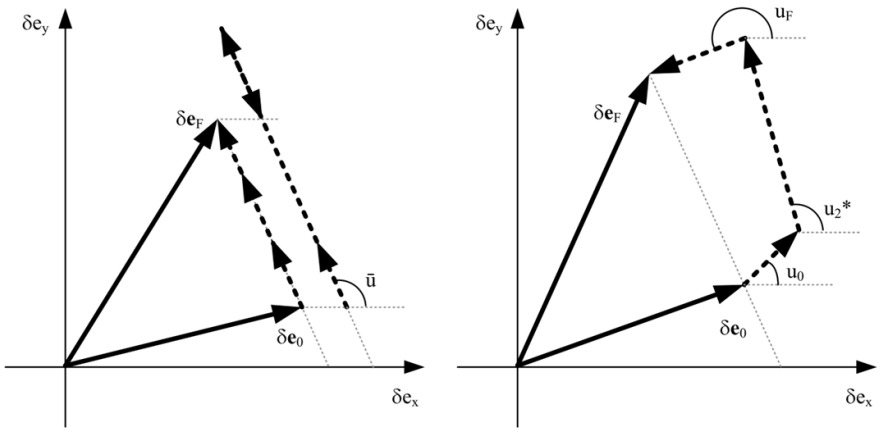

Figure 3.2.7: $\nexists_{12}$ (left) and $\nexists_{13}$ (right) manoeuvring schemes in the $\delta e_x/\delta e_y$ plane [30]

The aforementioned three-point tangential schemes are shown in Fig.3.2.7:

1. The $\not{\mathcal{N}}_{12}$ manoeuvre is said to achieve the absolute minimum possible Δv cost when the variation of the in-plane dimension $\Delta\delta e$ is the dominant cost factor among the IP elements; under a geometrical point of view, it minimises the path in the $\delta e_x/\delta e_y$ space by executing the tangential firings at arguments of latitude u equal to the phase of the total required $\Delta\delta\mathbf{e}$ vector, meaning that the changes in the relative eccentricity vector always lay parallel to the vector $\delta\mathbf{e}^F - \delta\mathbf{e}^0$.

2. The $\not{\mathcal{N}}_{13}$ scheme instead results more convenient when the major cost factor is represented by the changes in relative drift; in this case the main idea is to start and stop an intermediate drift as the first and last possible actions. The location of the second firing is to be computed numerically.

Because of its low computational effort required, predictability and efficiency, the analytical solution given by the first scheme, simply referred to as "three-point-tangential firing scheme" in the following, was selected for implementation in the control level for the autonomous guidance software of the AVANTI experiment [29] and studied in successive publications. In particular, in the references [10][53] it was argued that the minimum Δv bound for in-plane reconfiguration found in [30] could be easily extended to eccentric targets and the 3-pt tangential scheme was reformulated for unperturbed elliptic orbits; however, because of the adoption of the LVLH frame in both derivations the manoeuvre locations could only be provided as a formula to be solved iteratively (see Eq.(44) of [10]).

Three-Point Tangential Firing Scheme

This section presents the closed-form solution for the described 3-pt tangential manoeuvre for IP control in unperturbed eccentric orbits. Since the locations of the firings need to be aligned along the desired $\Delta\delta\mathbf{e}$ direction, they can be found by taking the ratio of the $\mathcal{B}_{31}^{TAN}$ and $\mathcal{B}_{41}^{TAN}$ elements of the derived input matrix:

$$\frac{\Delta\delta e_x}{\Delta\delta e_y} = \frac{e\cos\omega + \cos(\omega + f_{man})}{e\sin\omega + \sin(\omega + f_{man})} \tag{3.12}$$

By using again the auxiliary angle method as done in Eq.3.7 the solution is computed as:

$$\begin{aligned} f_{man} &= \arccos\left(\frac{K_3}{R}\right) + \alpha, \qquad f'_{man} = 2\pi - \arccos\left(\frac{K_3}{R}\right) + \alpha \\ K_1 &= \frac{\Delta\delta e_x}{\Delta\delta e_y}\sin\omega - \cos\omega, \quad K_2 = \frac{\Delta\delta e_x}{\Delta\delta e_y}\cos\omega + \sin\omega, \\ K_3 &= e\cos\omega - \frac{\Delta\delta e_x}{\Delta\delta e_y}e\sin\omega, \qquad R = \sqrt{K_1^2 + K_2^2} \end{aligned} \tag{3.13}$$

The true anomalies of the manoeuvres f_{man} and f'_{man} represent the two points per orbit where the firing may be delivered; logically, if the closest point is f_{man}, the three manoeuvring points to consider are $[f_{man}, f'_{man}, f_{man} + 2\pi]$. It can be proven that the maximum time length of the reconfiguration (since the moment the manoeuvre is computed) is 1.5 orbits. As for the firing amplitudes, they are derived by considering the effect of the i-th firing and unperturbed Keplerian propagation (see STM in Eq.2.33) to express the evolution of the in-plane ROE as $\delta\alpha_F = \Phi_{0f}\delta\alpha_0 + \Phi_{if}\Delta\delta\alpha_i$. By expressing each component:

$$\begin{cases} \Delta\delta a = \delta a_F - \delta\alpha_0 = \frac{2av_1}{\mu}\delta v_{T1} + \frac{2av_2}{\mu}\delta v_{T2} + \frac{2av_3}{\mu}\delta v_{T3} \\ \Delta\delta\lambda = M_{0F}\delta a_0 + M_{1F}\frac{2av_1}{\mu}\delta v_{T1} + M_{2F}\frac{2av_2}{\mu}\delta v_{T2} + \mathcal{B}^1_{21}\delta v_{T1} + \mathcal{B}^2_{21}\delta v_{T2} + \mathcal{B}^3_{21}\delta v_{T3} \\ \Delta\delta e_x = \mathcal{B}^1_{31}\delta v_{T1} + \mathcal{B}^2_{31}\delta v_{T2} + \mathcal{B}^3_{31}\delta v_{T3} \\ \Delta\delta e_y = \mathcal{B}^1_{41}\delta v_{T1} + \mathcal{B}^2_{41}\delta v_{T2} + \mathcal{B}^3_{41}\delta v_{T3} \end{cases} \tag{3.14}$$

$$M_{ij} = -\frac{3}{2}n(t_j - t_i)$$

where $\mathcal{B}^i_{kj}$ refers to the kj component of the input matrix written in the TAN frame and evaluated at the i-th time instant. By only considering the first three of Eqs.3.14:

$$\begin{aligned} \begin{bmatrix} \frac{\mu}{2a}\Delta\delta a \\ \Delta\delta\lambda - M_{0f}\delta a_0 \\ \Delta\delta e_x \end{bmatrix} &= \begin{pmatrix} v_1 & v_2 & v_3 \\ \mathcal{B}^1_{21} + M_{1F}\frac{2av_1}{\mu} & \mathcal{B}^2_{21} + M_{2F}\frac{2av_2}{\mu} & \mathcal{B}^3_{21} \\ \mathcal{B}^1_{31} & \mathcal{B}^2_{31} & \mathcal{B}^3_{31} \end{pmatrix} \begin{bmatrix} \delta v_{T1} \\ \delta v_{T2} \\ \delta v_{T3} \end{bmatrix} \\ &= \begin{pmatrix} v_1 & v_2 & v_3 \\ C_1^* & C_2^* & C_3 \\ D_1 & D_2 & D_3 \end{pmatrix} \begin{bmatrix} \delta v_{T1} \\ \delta v_{T2} \\ \delta v_{T3} \end{bmatrix} \end{aligned} \tag{3.15}$$

The solution is found by analytically inverting the matrix:

$$\begin{bmatrix} \delta v_{T1} \\ \delta v_{T2} \\ \delta v_{T3} \end{bmatrix} = \frac{1}{\det} \begin{pmatrix} C_2^*D_3 - C_3D_2 & -v_2D_3 + v_3D_2 & v_2C_3 - v_3C_2^* \\ -C_1^*D_3 + C_3D_1 & v_1D_3 - v_3D_1 & -v_1C_3 + v_3C_1^* \\ C_1^*D_2 - C_2^*D_1 & -v_1D_2 + v_2D_1 & v_1C_2^* - v_2C_1^* \end{pmatrix} \begin{bmatrix} \frac{\mu}{2a}\Delta\delta a \\ \Delta\delta\lambda - M_{0f}\delta a_0 \\ \Delta\delta e_x \end{bmatrix} \tag{3.16}$$

$$\det = v_1(C_2^*D_3 - C_3D_2) - v_2(C_1^*D_3 - C_3D_1) + v_3(C_1^*D_2 - C_2^*D_1)$$

The derived manoeuvring scheme is validated using linear propagation in both a circular and eccentric target orbit cases, using the data reported in Tab.3.2.5. Fig.3.2.8

Table 3.2.5: Initial and final data for 3pt tangential control manoeuvre test

a [km]	e [-]	i [^{o}]	Ω [^{o}]	ω [^{o}]	f_0 [^{o}]
30500	**0/0.75**	-5	357	88	90

ROE [m]	$a\delta a$	$a\delta\lambda$	$a\delta e_x$	$a\delta e_y$	$a\delta i_x$	$a\delta i_y$
Initial	-20	-700	130	-50	40	0
Aimed	0	-500	150	0	-	-

reports the linear propagation results in the in-plane LVLH frame of the target for both eccentricity cases; as already explained in Sec.2.1.5, within this frame one can notice that the in-plane size along z is increasingly amplified for higher along-track distances x from the origin when $e \neq 0$. A further observation, which is specific to the considered tests, is that in both cases the first firing introduces an intermediate relative drift which is higher than the initial one, making the chaser drift away faster in the case of loss of thrust control. Fig.3.2.9 shows instead the paths followed in the ROE space throughout

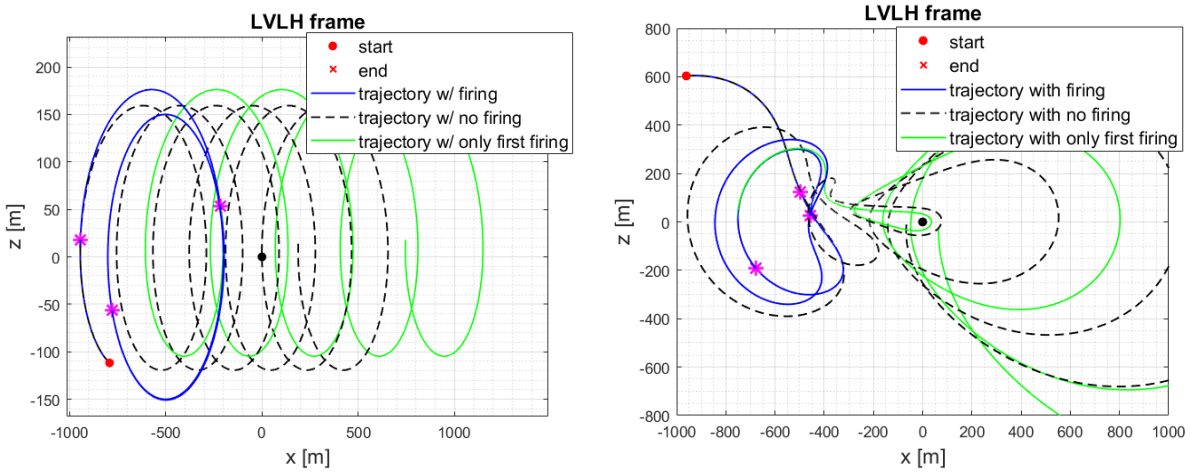

Figure 3.2.8: 3-pt tan. manoeuvre results in LVLH, circular (left) and eccentric (right)

the entire manoeuvre. Based on these plots, some observations can be made:

- The manoeuvre follows a minimum distance path in the $\delta e_x/\delta e_y$ space in both cases, owing to the choice on the placing of the firing anomalies.
- The main notable difference introduced when dealing with non-zero eccentricities of the target is that the jumps caused by the tangential

firings in the $\delta\lambda/\delta a$ space are no longer exactly vertical; this is explained by the fact that the relative mean longitude $\delta\lambda$ is not affected by velocity changes in the tangential direction when $e = 0$ (and $\eta = 1$), as it can be verified by the second of Eqs.3.3.

- A further significant difference is that in the eccentric scenario the manoeuvre produces an intermediate relative orbit (after the first firing) which drifts tens of meters past the aimed along-track position of -500 m; this is something which needs to be accounted for especially when deciding which manoeuvre to use during proximity operations, owing to the strict requirements coming from other GNC functions (*e.g.*, vision-based navigation).

- The circular reconfiguration examined requires a total $\Delta v \approx 0.006$ m/s whereas the eccentric one amounts to $\Delta v \approx 0.009$ m/s.

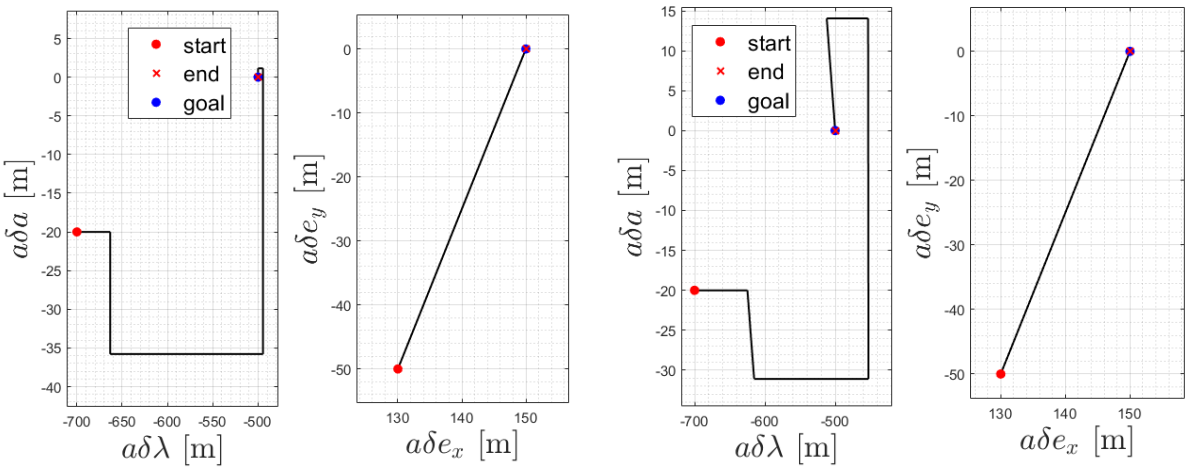

Figure 3.2.9: 3-pt tan. manoeuvre results in ROE, circular (left) and eccentric (right)

Two-Point Radial Firing Scheme

The three-point tangential scheme proves to be quite convenient in the most general in-plane reconfiguration for the following reasons:

- In terms of predictability, if the scheduler exploits all the next available nodes, the reconfiguration always takes less than one and a half orbit periods. As it will be seen in later sections, this level of time determinism is desirable when a higher level planner needs to allocate time slots where the chaser may or may not manoeuvre.

- In terms of fuel consumption, the in-plane reconfiguration using tangential firings is physically more convenient than the radial schemes owing to the higher controllability of the orbit energy in the velocity direction.

Nonetheless, in some scenarios the reduced influence of radial manoeuvres on the orbital energy can be considered as a benefit rather than a drawback; in fact, by employing radial burns only, the effect of the thrust errors on the in-plane elements is minimised and higher control accuracy can be achieved (as seen from the flight results of the SAFE formation flying guidance experiment [14]). Moreover, a manoeuvring scheme which does not impact the relative drift is also particularly interesting in cubesat formations where periodic formation keeping against J_2 effects may not be feasible due to the limited amount of fuel; in such cases the safety condition needs to rely on a separation on the relative longitude between the pair. Reference [41] proposes two and three point schemes using radial burns in circular target orbits; to generalise the idea to eccentric reference orbits, the TAN frame is adopted once again to define the control scheme.

Because only three IP components are to be commanded (δa is not controllable), two firings are sufficient to grant full controllability of the problem. The idea is once again to choose the argument of latitude of the firings in such a way that the individual corrections on $\delta\mathbf{e}$ are collinear to the total desired $\Delta\delta\mathbf{e}$, therefore the two locations can be computed according to Eqs.3.7. The amplitudes are instead computed in a similar way to the previous scheme:

$$\begin{cases} \Delta\delta\lambda &= M_{0F}\delta a_0 + \mathcal{B}^1_{23}\delta v_{R1} + \mathcal{B}^2_{23}\delta v_{R2} \\ \Delta\delta e_x &= \mathcal{B}^1_{33}\delta v_{R1} + \mathcal{B}^2_{33}\delta v_{R2} \\ \Delta\delta e_y &= \mathcal{B}^1_{43}\delta v_{R1} + \mathcal{B}^2_{43}\delta v_{R2} \end{cases} \tag{3.17}$$

$$M_{ij} = -\frac{3}{2}n(t_j - t_i)$$

Upon inversion of the first two of Eqs.3.17 one obtains:

$$\begin{bmatrix} \delta v_{R1} \\ \delta v_{R2} \end{bmatrix} = \frac{1}{\mathcal{B}^1_{23}\mathcal{B}^2_{33} - \mathcal{B}^1_{33}\mathcal{B}^2_{23}} \begin{pmatrix} \mathcal{B}^2_{33} & -\mathcal{B}^2_{23} \\ -\mathcal{B}^1_{33} & \mathcal{B}^1_{23} \end{pmatrix} \begin{bmatrix} \Delta\delta\lambda - M_{0F}\delta a_0 \\ \Delta\delta e_x \end{bmatrix} \tag{3.18}$$

The manoeuvre is validated using the data in Tab.3.2.6, which represents a case where the chaser shrinks and re-centers the relative orbit on the target position. Fig.3.2.10

Table 3.2.6: Initial and final data for 2pt radial control manoeuvre test

a [km]	e [-]	i [^{o}]	Ω [^{o}]	ω [^{o}]	f_0 [^{o}]
24500	0.44	39	357	0	350

ROE [m]	$a\delta a$	$a\delta\lambda$	$a\delta e_x$	$a\delta e_y$	$a\delta i_x$	$a\delta i_y$
Initial	0	100	230	-50	230	0
Aimed	-	0	150	25	-	-

reports the linear propagation results in the LVLH frame. The main notable feature of the trajectory is the fact that the intermediate orbit (in green) used to reach the final desired one is drift-free, increasing safety of the reconfiguration. A comparison may be

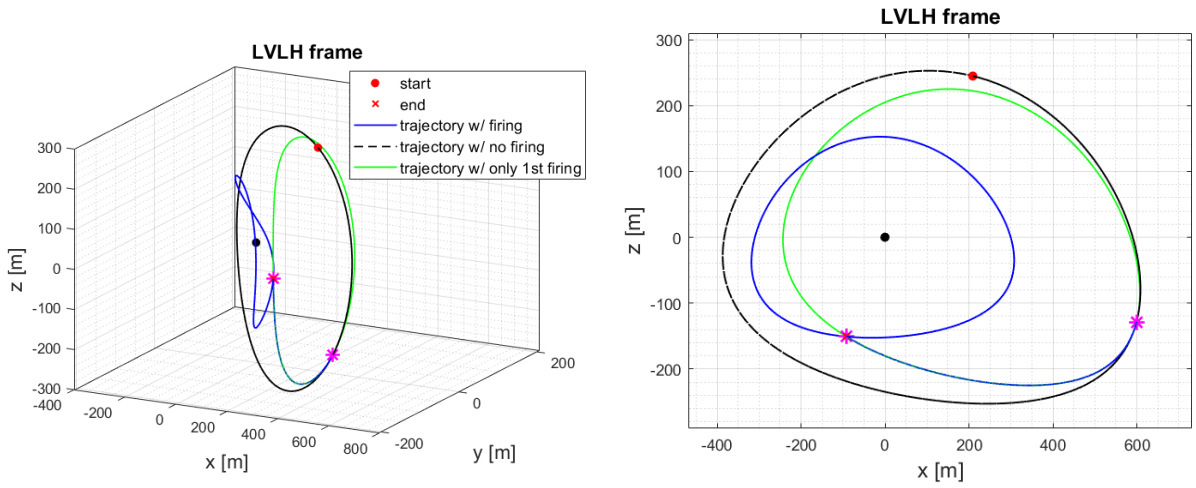

Figure 3.2.10: 2-pt radial manoeuvre results in LVLH frame

drawn to the three-point tangential scheme to analyse the differences between the two using the same test data as reported in Tab.3.2.6, with a final aimed $a\delta a$ equal to zero. Fig.3.2.11 shows the trajectory obtained using the tangential scheme. As expected from previous discussions, the key drawback of the tangential scheme is the reduced PAS of the reconfiguration owing to induced non-zero intermediate relative drifts, which lead to significant risks of collision in case of occurring anomalies during the second and third firings. As for fuel consumption, the radial scheme requires a total $\Delta v \approx 0.019$ m/s whereas the second amounts to $\Delta v \approx 0.010$ m/s, which entails that almost half of the fuel is saved. The main conclusion is that the choice of either manoeuvre is to be based on the specific reconfiguration scenario, in particular:

- The use of the tangential scheme is ideal whenever the relative orbit

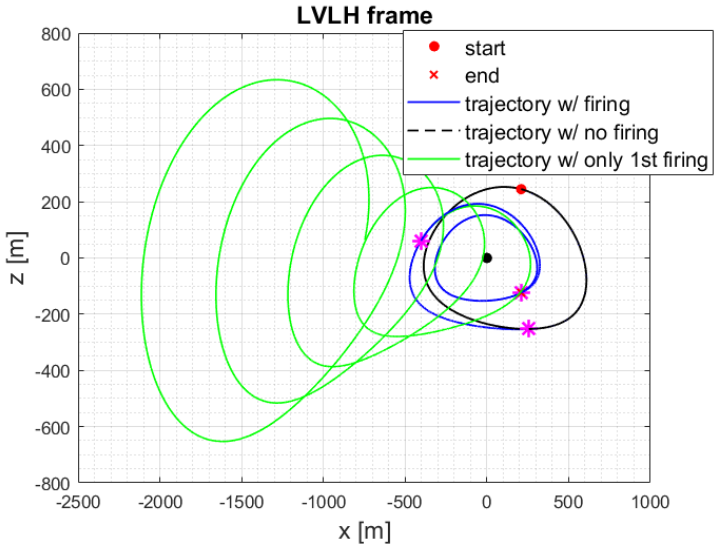

Figure 3.2.11: 3-pt tangential manoeuvre results in LVLH frame for comparison

reconfiguration asks for large variations of the in-plane size (which would amount to large amounts of fuel being consumed) and for control on the relative drift.

- The radial scheme is instead suitable for close proximity operations which do not require large reconfigurations; as seen in the previous section, this manoeuvre might also be preferred to avoid ”overshoots” of $\delta\lambda$ during the reconfiguration.

Two-Impulse Non-Drifting Transfer Scheme

As it will be discussed in Sec.3.3, all the manoeuvres treated so far can be used to command and maintain the spiralling approach to the target discussed in Sec.3.1; at its core, this strategy involves moving between safe orbits using the natural orbit motion by imposing a non-zero drift $a\delta a$. To enhance trajectory safety during close-proximity operations (*e.g.*, beginning of the target inspection phase) one can also include drift-free transfer trajectories between the stationary safe orbits; this type of manoeuvre, typically referred to as ”radial hop” is one the main building blocks of the V-bar approach strategy described in Sec.3.1 and is well known and implemented in circular orbit rendezvous scenarios. Reference [51] provided a generalisation of the two-impulse non-drifting transfer analytical solution to elliptic orbits using a Cartesian and a differential orbit elements formulation.

The objective of this section is to build on [51] by providing a formulation for the currently adopted set of quasi-non-singular ROE. As in the original paper, the problem

is simplified by the following assumptions:

- As the other presented multiple-point schemes, it is possible to only focus on the in-plane problem as long as the OOP motion is properly phased and its control accounted for using the precompensation technique in Eqs.3.10.

- The first firing needs to have a radial as well as a tangential component; this last can be easily computed by nullifying the relative drift at the first firing point, which is arbitrarily chosen in this scheme.

The problem is therefore reduced to three equations (in the commanded $\Delta\delta\lambda$ and $\Delta\delta\mathbf{e}$ components) and three unknowns (amplitudes of the radial firings and location of the second). Assuming an initial non-zero relative drift δa_0, the tangential component of the first firing can be easily found from Eqs.3.3 as:

$$\delta v_{T1} = \frac{\mu}{2av_1}(-\delta a_0) \tag{3.19}$$

The effect of δv_{T1} can easily be accounted for in the rest of the derivation by defining a "reduced" set for the remaining ROE:

$$\begin{bmatrix} \delta\lambda \\ \delta e_x \\ \delta e_y \end{bmatrix}_{RED} = \begin{bmatrix} \delta\lambda \\ \delta e_x \\ \delta e_y \end{bmatrix}_0 + \begin{bmatrix} \mathcal{B}^1_{21} \\ \mathcal{B}^1_{31} \\ \mathcal{B}^1_{41} \end{bmatrix} \cdot \delta v_{T1} \tag{3.20}$$

These reduced elements are essentially the initial conditions to be used in the 2-pt radial non-drifting transfer. A further simplification of the derivation relies on the fact that the submatrix of the unperturbed STM (see Eq.2.33) describing the evolution of the three IP elements is equal to the identity matrix if $\delta a = 0$. This allows to write the propagation equation from the first to the second point of the manoeuvre as:

$$\delta\alpha^{2+}_{RED} = \delta\alpha^{1-}_{RED} + \mathcal{B}\{2:4,3\}|_1\delta v_{R1} + \mathcal{B}\{\,2:4,3\}|_2\delta v_{R2} \tag{3.21}$$

where the notation $|_i$ indicates which of the two firing points the quantities refer to. The reduced notation is omitted from now on. By expanding the previous equation it

is possible to obtain ($\nu = f + \omega$):

$$\begin{bmatrix} \delta\lambda_{2+} - \delta\lambda_{1-} \\ \delta e_{x,2+} - \delta e_{x,1-} \\ \delta e_{y,2+} - \delta e_{y,1-} \end{bmatrix} = \begin{bmatrix} \frac{2}{\not p} + \frac{r\cos f}{\not p a}\sqrt{\frac{1-\eta}{1+\eta}} \\ -\frac{r}{\not p a}\sin\nu - \frac{2e\sin\omega}{\not p} \\ \frac{r}{\not p a}\cos\nu + \frac{2e\cos\omega}{\not p} \end{bmatrix}_1 \frac{\delta v_{R1}}{v_1} + \begin{bmatrix} \frac{2}{\not p} + \frac{r\cos f}{\not p a}\sqrt{\frac{1-\eta}{1+\eta}} \\ -\frac{r}{\not p a}\sin\nu - \frac{2e\sin\omega}{\not p} \\ \frac{r}{\not p a}\cos\nu + \frac{2e\cos\omega}{\not p} \end{bmatrix}_2 \frac{\delta v_{R2}}{v_2} \tag{3.22}$$

By expressing $r = a\eta^2/\rho$, where $\rho = 1 + e\cos f$, the velocity impulses can be scaled using the formula:

$$\widetilde{\delta v} = \frac{\delta v_R}{\rho v} \tag{3.23}$$

Eq.3.22 can be reorganized in the following form:

$$\begin{bmatrix} \delta\lambda_{\Delta v,1} & \delta\lambda_{\Delta v,2} \\ \delta e_{x,\Delta v,1} & \delta e_{x,\Delta v,2} \\ \delta e_{y,\Delta v,1} & \delta e_{y,\Delta v,2} \end{bmatrix} \begin{bmatrix} \widetilde{\delta v}_1 \\ \widetilde{\delta v}_2 \end{bmatrix} = \begin{bmatrix} \Delta\delta\lambda \\ \Delta\delta e_x \\ \Delta\delta e_y \end{bmatrix}$$

where: (3.24)

$$\delta\lambda_{\Delta v} = 2\rho + \eta^2\cos f\sqrt{\frac{1-\eta}{1+\eta}}$$

$$\delta e_{x,\Delta v} = -\eta^2\sin\nu - 2\rho e\sin\omega$$

$$\delta e_{y,\Delta v} = \eta^2\cos\nu + 2\rho e\cos\omega$$

Using the second and third of Eqs.3.24 it is possible to find the expressions for the scaled velocity changes as:

$$\begin{aligned} \widetilde{\delta v}_1 &= \frac{\delta e_{x,\Delta v2}\Delta\delta e_y - \delta e_{y,\Delta v2}\Delta\delta e_x}{\delta e_{x,\Delta v2}\cdot\delta e_{y,\Delta v1} - \delta e_{y,\Delta v2}\cdot\delta e_{x,\Delta v1}} \\ \widetilde{\delta v}_2 &= \frac{\delta e_{y,\Delta v1}\Delta\delta e_x - \delta e_{x,\Delta v1}\Delta\delta e_y}{\delta e_{x,\Delta v2}\cdot\delta e_{y,\Delta v1} - \delta e_{y,\Delta v2}\cdot\delta e_{x,\Delta v1}} \end{aligned} \tag{3.25}$$

The scaled velocities found in Eqs.3.25 can be substituted into the first of Eqs.3.24. By simplifying the resulting equation and expressing it as a function of the only unknown f_2, it is possible to once again arrive to the familiar trigonometric form $K_1\cos f_2 + K_2\sin f_2 = K_3$ and solve it using the already employed auxiliary angle

method (see Eqs.3.13), where the coefficients are:

$$\begin{aligned} K_1 &= \Delta\delta e_x K_{ex1} + \Delta\delta e_y K_{ey1} + \Delta\delta\lambda K_{\lambda 1} \\ K_2 &= \Delta\delta e_x K_{ex2} + \Delta\delta e_y K_{ey2} + \Delta\delta\lambda K_{\lambda 2} \\ K_3 &= -(\Delta\delta e_x K_{ex0} + \Delta\delta e_y K_{ey0} + \Delta\delta\lambda K_{\lambda 0}) \end{aligned} \tag{3.26}$$

$$\begin{aligned} &K_{ex0} = 2e\cos\omega\delta\lambda_{\Delta v1} - 2\delta e_{y,\Delta v1}, \qquad K_{ex2} = -\eta^2\delta\lambda_{\Delta v1}\sin\omega \\ &K_{ex1} = \eta^2\delta\lambda_{\Delta v1}\cos\omega + 2e^2\cos\omega\delta\lambda_{\Delta v1} - 2e\delta e_{y,\Delta v1} + \delta e_{y,\Delta v1}\beta \end{aligned}$$

$$\begin{aligned} &K_{ey0} = 2e\sin\omega\delta\lambda_{\Delta v1} + 2\delta e_{x,\Delta v1}, \qquad K_{ey2} = \eta^2\delta\lambda_{\Delta v1}\cos\omega \\ &K_{ey1} = \eta^2\delta\lambda_{\Delta v1}\sin\omega + 2e^2\sin\omega\delta\lambda_{\Delta v1} + 2e\delta e_{x,\Delta v1} - \delta e_{x,\Delta v1}\beta \end{aligned} \tag{3.27}$$

$$\begin{aligned} &K_{\lambda 0} = -2e\cos\omega\delta e_{x,\Delta v1} - 2e\sin\omega\delta e_{y,\Delta v1}, \quad K_{\lambda 2} = \eta^2(\delta e_{x,\Delta v1}\sin\omega - \delta e_{y,\Delta 1}\cos\omega) \\ &K_{\lambda 1} = -\eta^2\delta e_{x,\Delta v1}\cos\omega - 2e^2\cos\omega\delta e_{x,\Delta v1} - 2e^2\sin\omega\delta e_{y,\Delta v1} - \delta e_{y,\Delta v1}\eta^2\sin\omega \end{aligned}$$

where $\beta = \eta^2\sqrt{\frac{1-\eta}{1+\eta}}$. The formulation for the non-drifting transfer using quasi-non-singular ROE is concluded; after computing the anomaly of the second firing by solving the trigonometric equation with coefficients K_1, K_2, K_3 the amplitudes of the two radial firings can be found using Eqs.3.25. These last expressions become singular for a transfer angle $\varphi = f_2 - f_1 = k\pi$, with k even, meaning that the second anomaly of firing is to be chosen as the one which is neither coincident with the initial position nor separated by a full orbit period. The algorithm is validated in an elliptic target case as well as in a zero eccentricity case (to which the original formulation is singular) using the data in Tab.3.2.7. The propagation results are reported in Fig.3.2.12 and Fig.3.2.13.

Table 3.2.7: Initial and final data for non-drifting transfer manoeuvre test

a [km]	e [-]	i [^{o}]	Ω [^{o}]	ω [^{o}]	f_0 [^{o}]
14500	**0/0.21**	39	357	28	90

ROE [m]	$a\delta a$	$a\delta\lambda$	$a\delta e_x$	$a\delta e_y$	$a\delta i_x$	$a\delta i_y$
Initial	-5	-650	100	10	100	0
Aimed	0	-200	50	0	-	-

The initial relative orbit is characterized by a relative drift which is nullified with the tangential component of the first firing; this generates a transfer orbit which returns to

the initial firing point in case the second one cannot be executed (see green trajectory arc), increasing the passive safety of the approach. Fig.3.2.13 demonstrates that the

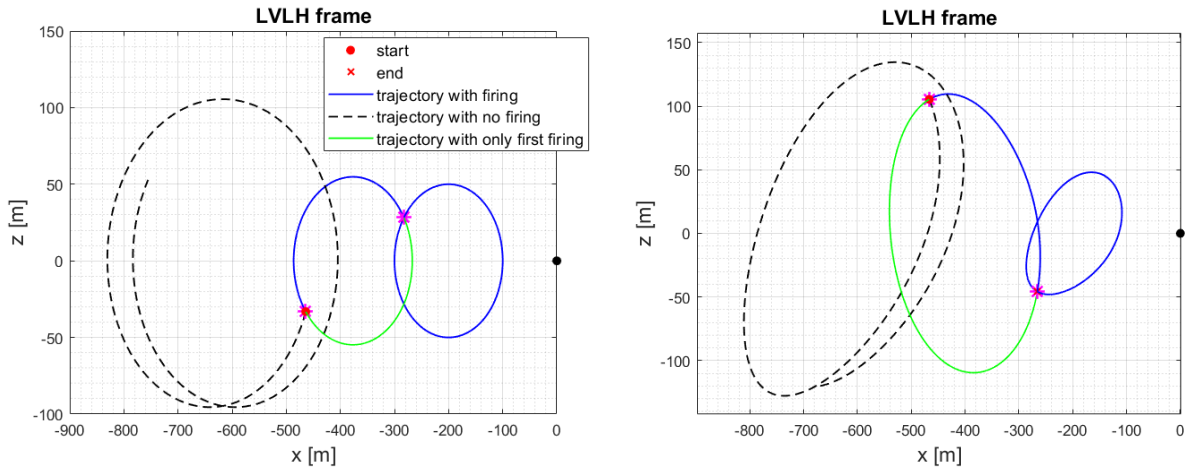

(a) Circular target case (b) Eccentric target case

Figure 3.2.12: Non-drifting transfer manoeuvre results in LVLH

algorithm is able to successfully reach the desired in-plane ROE for both eccentricity cases, although with quite different phases of the intermediate relative eccentricity vector $\delta\mathbf{e}$; this means that, in general, it is not possible to impose that the transfer orbit complies with the E/I separation criterion and that it might cross the KOZ on the cross-track projection.

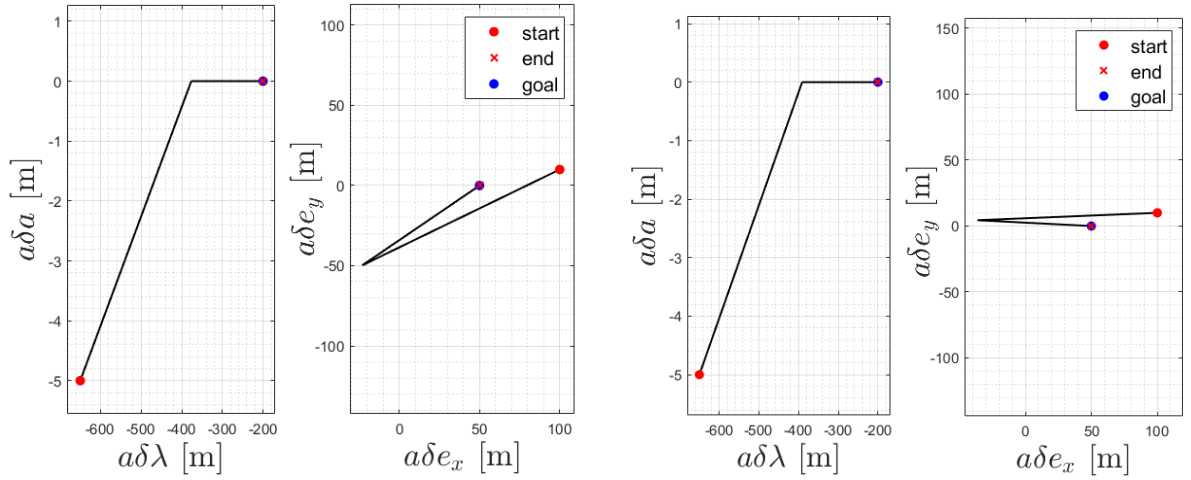

(a) Circular target case (b) Eccentric target case

Figure 3.2.13: Non-drifting transfer manoeuvre results in ROE space

3.2.3 Glideslope Manoeuvres

In the context of proximity operations for spacecraft rendezvous, the term glideslope refers to a N-pulse manoeuvre originally developed for close-range activities of the space shuttle with other vehicles [46]; the algorithm allows to follow a translational motion in any direction in space through an impulsive guidance function. A typical use of the glideslope is to approach a target vehicle for docking, in which case an inbound decelerating profile is required.

Cartesian Space Formulations

An autonomous glideslope function is classically based on the two-impulse rendezvous problem [34], which is formulated in the Cartesian relative space because the STM can be factorized as in the following:

$$\Phi^{LVLH} = \begin{bmatrix} \Phi_{rr} & \Phi_{r\dot{r}} \\ \Phi_{\dot{r}r} & \Phi_{\dot{r}\dot{r}} \end{bmatrix} \tag{3.28}$$

which allows to write the evolution of relative position and velocity as:

$$\begin{aligned} \mathbf{r}(t) &= \Phi_{rr}(t)\mathbf{r}_0 + \Phi_{r\dot{r}}(t)\dot{\mathbf{r}}_0 \\ \dot{\mathbf{r}}(t) &= \Phi_{\dot{r}r}(t)\mathbf{r}_0 + \Phi_{\dot{r}\dot{r}}(t)\dot{\mathbf{r}}_0 \end{aligned} \tag{3.29}$$

By using the first of Eqs.3.29, it is possible to compute the necessary velocity jump at the first point $\mathbf{r}_1$ to reach a desired position $\mathbf{r}_2$ after a given time interval:

$$\Delta\mathbf{v}_1 = \Phi_{r\dot{r}}^{-1}(\mathbf{r}_2 - \Phi_{rr} \cdot \mathbf{r}_1) - \dot{\mathbf{r}}_1 \tag{3.30}$$

This first velocity jump pushes the chaser towards to desired position, but in order to control the arrival velocity, the second of Eqs.3.29 is used:

$$\Delta\mathbf{v}_2 = \dot{\mathbf{r}}_2 - (\Phi_{\dot{r}r}\mathbf{r}_1 + \Phi_{\dot{r}\dot{r}} \cdot (\dot{\mathbf{r}}_1 + \Delta\mathbf{v}_1)) \tag{3.31}$$

The working principle of the different glideslope functions is commonly based on building a trajectory which, is discretised in space and to use Eq.3.30 at each considered point to reach the next. A further consideration to be made is the fact that the very simple STM which propagates the relative motion through the ROE

described in Eq.2.33 (or any other including perturbations) can be used within the described framework as long as a linear map between the ROE and the cartesian LVLH coordinates is available. In fact, according to the properties of Φ discussed in Sec.2.1.6, it is possible to write:

$$\Phi^{LVLH} = \frac{\partial \mathbf{x}^{LVLH}}{\partial \delta \boldsymbol{\alpha}_{qns}} \cdot \Phi^{ROE} \cdot \frac{\partial \delta \boldsymbol{\alpha}_{qns}}{\partial \mathbf{x}^{LVLH}} \tag{3.32}$$

The introduced equations can be used to implement the classic straight-line inbound decelerating glideslope on orbits of arbitrary eccentricity according to [34]. The main idea is to define a "distance-to-go" vector $\boldsymbol{\rho}(t)$ which emanates from the target position $\mathbf{r}_T(t)$ and defines the direction to the initial position $\mathbf{r}_0$; its direction cosines (which define the unit vector $\mathbf{u}_\rho$) are given by:

$$\begin{aligned} \cos\alpha &= (x_0 - x_T)/\rho_0 \\ \cos\beta &= (y_0 - y_T)/\rho_0 \\ \cos\gamma &= (z_0 - z_T)/\rho_0 \end{aligned} \tag{3.33}$$

where ρ_0 is the initial distance to go. By specifying the initial $\dot{\rho}_0$ and target $\dot{\rho}_T$ approach velocities (reasonably defined as $\dot{\rho}_0 < \dot{\rho}_T < 0$) a linear relationship between ρ and $\dot{\rho}$ can be postulated:

$$\dot{\rho} = a\rho + \dot{\rho}_T \tag{3.34}$$

The intermediate positions to go through are then written as:

$$\rho(t) = \rho_0 e^{a \cdot t} + (\dot{\rho}_T/a)(e^{at} - 1) \tag{3.35}$$

where $a = (\dot{\rho}_0 - \dot{\rho}_T)/\rho_0$. The total transfer time is fixed by $\dot{\rho}_0$ and $\dot{\rho}_T$, hence by deciding how many N thruster firings to use, which divides the approach trajectory in uniform intervals, the intermediate positions may be obtained using Eq.3.35; once each point is reached, Eq.3.30 can be used to compute the necessary impulse to reach the next. This way, no firing is executed at the last position, minimizing plume impingement on the target spacecraft. The manoeuvre is validated using data in Tab.3.2.8 and its propagation results are shown in Fig.3.2.14. As can be observed from Fig.3.2.14a, the actual approach trajectory of the chaser is not along the approach line, but is instead characterised by jumps between the discretised positions, owing to the relative orbital dynamics. The relative approach velocity along $\boldsymbol{\rho}$ is also shown not to follow exactly

Table 3.2.8: Initial and final data for straight-line glideslope manoeuvre test

a [km]	e [-]	i [^{o}]	Ω [^{o}]	ω [^{o}]	f_0 [^{o}]
28348	0.6	40	45	100	150

LVLH [m]	x	y	z	v_x	v_y	v_z
Initial	100	70	70	0	0	0
Aimed	10	10	10	-	-	-

$N_{firings}$	$\dot{\rho}_0$ [m/s]	$\dot{\rho}_T$ [m/s]
5	-10^{-2}	-10^{-3}

a linear evolution (see Fig.3.2.14b), but it is always lower than the prescribed linear trend based on $\dot{\rho}_T$ and $\dot{\rho}_0$. The glideslope manoeuvre allows to follow a forced-motion trajectory in the Cartesian space, including circular ones for target circumnavigation, and can be used as terminal guidance in the last phase of rendezvous. The next section investigates how this approach can be extended to the ROE space formulation.

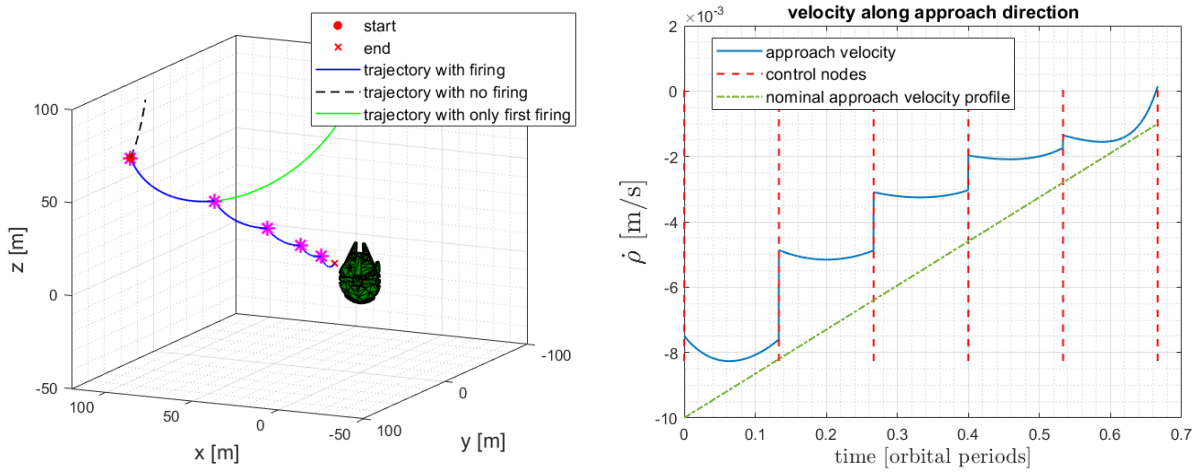

(a) LVLH trajectory

(b) Approach-line velocity over time

Figure 3.2.14: Straight-line inbound decelerating glideslope propagation results

Relative Orbit Elements Space Formulations

The main limit of formulating a glideslope-like manoeuvre function in the ROE space is the fact that the STM cannot be factorized as shown in Eq.3.28. Still, the adoption of a formulation based on relative orbit elements could enable building a trajectory which

passes through PAS relative orbits in a predetermined time window, a feature which, as seen in later sections, can prove to be particularly useful in the final approach to a safe inspection orbit. The general two-point transfer between two arbitrary relative states at fixed time instants t_1, t_F can be expressed as:

$$\delta\alpha_F = \Phi_{1F}^{\delta\alpha}\delta\alpha_1 + \Phi_{1F}^{\delta\alpha}\mathcal{B}_1\delta\mathbf{v}_1 + \mathcal{B}_\mathcal{F}\delta\mathbf{v}_F \tag{3.36}$$

which can be rewritten as the system:

$$\underbrace{\begin{bmatrix}\Phi_{1F}^{\delta\alpha}\mathcal{B}_1 & I\cdot\mathcal{B}_\mathcal{F}\end{bmatrix}}_{6\times 6}\underbrace{\begin{bmatrix}\delta\mathbf{v}_1\\ \delta\mathbf{v}_F\end{bmatrix}}_{6\times 1} = \mathbf{A}\cdot\mathbf{x} = \underbrace{\delta\alpha_F - \Phi_{1F}^{\delta\alpha}\delta\alpha_1}_{6\times 1} = \mathbf{b} \tag{3.37}$$

The solution of Eq.3.37 is found as the minimum 2-norm of $\mathbf{x}$ through the following expression [47]:

$$\mathbf{x} = \mathbf{A}^T(\mathbf{A}\mathbf{A}^T)^{-1}\mathbf{b} \tag{3.38}$$

The idea is to define a set of intermediate safe relative states in the ROE space and use Eq.3.38 to compute the velocity changes between each couple of relative orbits. To

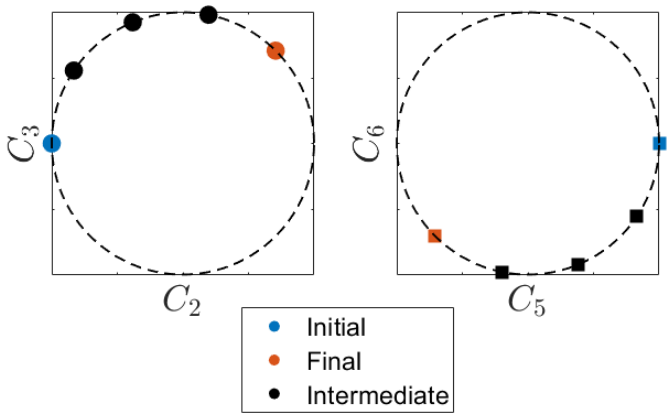

Figure 3.2.15: Definition of intermediate phasing angles for glideslope manoeuvre

avoid loss of generality caused by the assumptions on the eccentricity, the intermediate states are defined using the described C-elements (see Sec.2.1.5); in particular, the intermediate orbits are taken by sampling the shortest angle differences between the initial and final IP and OOP phasing angles (see Fig.3.2.15), previously defined as α and β. The IP and OOP sizes, respectively defined C_{IP} and C_{OOP}, as well as the element C_4 which represents the along-track position are linearly sampled between the initial

and final values; the intermediate C_1 elements are chosen to obtain drift-free orbits[5] according to Eq.2.26. The manoeuvre is validated using the data shown in Tab.3.2.9 and propagation results for two eccentricity cases reported in Fig.3.2.16.

Table 3.2.9: Initial and final data for ROE-based glideslope manoeuvre test

a [km]	e [-]	i [^{o}]	Ω [^{o}]	ω [^{o}]	f_0 [^{o}]	$N_{firings}$	T_{transf} [orbits]
28348	**0/0.3**	40	45	100	150	5	1.2

C-elements [m]	C_1	C_2	C_3	C_4	C_5	C_6
Initial	**0/-275.23**	-500	0	500	500	0
Aimed	**0/55.05**	100	100	200	-100	-100

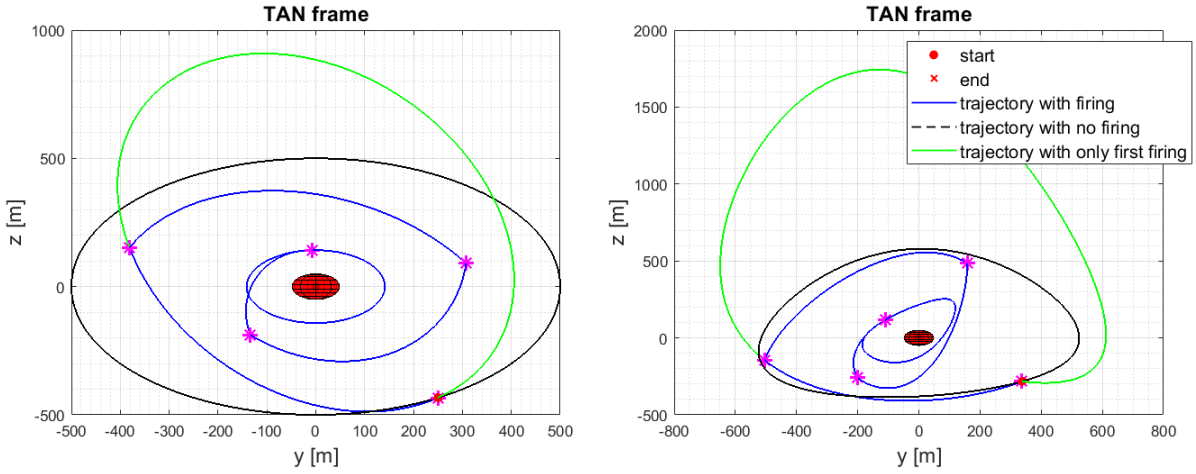

(a) Circular target case

(b) Eccentric target case

Figure 3.2.16: ROE-based glideslope propagation results in cross-track TAN frame

The trajectories are represented in the velocity-aligned (TAN) frame and only their projection on the cross-track plane, used to show compliance with E/I-based passive safety, is reported. The implemented manoeuvre scheme produces a trajectory that winds around the origin without crossing it, which can be interesting in scenarios where large re-phasing (in terms of the α and β angles, which allow to pick a certain geometry out of the family shown in Fig.2.1.7b) of the relative orbit is needed in a deterministic time.

[5]The choice on the intermediate values taken on by C_1 is considered here an arbitrary one which may result inconvenient based on the fuel use in some reconfiguration scenarios.

3.2.4 Summary

Tab.3.2.10 reports a summary of the developed manoeuvring schemes, with a brief discussion regarding their main features.

Table 3.2.10: Summary of manoeuvring schemes

Manoeuvre	Use	Advantages	Disadvantages
1PT OOP	Full control of out-of-plane relative motion	Only one firing needed, short reconfiguration window	High Δv cost
1PT RAD	Control of relative eccentricity components	No effect on relative drift, allows to execute quick and small corrections to compensate perturbation effects on IP shape	Higher Δv cost than tangential schemes, not suitable for large shape reconfigurations
1PT TAN	Control of drifting motion of relative orbit	Firing can be executed at any point on the orbit	Influence on relative eccentricity and relative mean longitude needs to be accounted for
3PT TAN	Full control of IP relative motion	Fuel consumption nears minimum Δv bound for large reconfigurations of the relative eccentricity components	Maximum reconfiguration time window of 1.5 orbit periods
2PT RAD	Control of relative eccentricity and relative mean longitude	No effect on relative drift, minimisation of effect of thrust errors on controlled IP elements	Higher Δv cost than tangential schemes
2PT Non-drifting transfer	Passively-safe transfer between arbitrary relative stationary orbits	Initial orbit can be drifting, manoeuvre can be executed at any point on the orbit	High Δv due to radial firings
N-PT Glideslopes	Reach arbitrary Cartesian state or relative orbit using N-firings	Manoeuvre transfer time is deterministic and given as input	Firings are not aligned with a specific direction and can lead to significant Δv costs

PT=Point, **OOP**=Out-Of-Plane (Y_{TAN}), **RAD**=Radial (Z_{TAN}), **TAN**=Tangential (X_{TAN})

3.3 Guidance Strategies

Having completed the development of the manoeuvring schemes which change the relative state of the chaser, the discussion can now shift to the higher layers of the guidance software, represented by different types of logics which can be embedded in the rendezvous concept of operations.

3.3.1 Finite State Machine Guidance

As introduced in Sec.1.2, one of the ways by which autonomous spacecraft operations may be enabled is through the previously defined rule-based architectures, which entail a complete definition of the conditions in which the spacecraft might be and corresponding actions to take in response to specific scenarios. The most straightforward realization of this type of decisional architecture takes the form of a Finite State Machine (FSM), a computational model that has the following properties:

- It is characterised by a finite number of states and transitions between them, which are regulated by specific conditions, or guards, that define the behavioural logic of the FSM. On one side this requires a deep understanding of the problem at hand in order to present the correct guidance response to different scenarios but makes the behaviour of the agent predictable and deterministic, properties which are highly desirable in space missions design.
- Complexity of the decisions may be increased through the process of nesting of the defined states, which in practice introduces a hierarchy in the switching criteria, giving a higher priority to certain transitions over others.

The use of the FSM concept applied to autonomous rendezvous operations is, surprisingly, almost a novel idea within the literature, and has been formally proposed and studied in the context of formations maintenance and control in [65], where relative orbits are characterised as ”slots”. The presented architecture has been developed using Stateflow, a MATLAB/Simulink toolbox which enables the direct implementation of state transition flowcharts to describe how a set of models reacts to inputs, events and time-based conditions. To build a finite state machine logic around the rendezvous concept, an approach geometry which may be generalised to a variety of missions is devised based on the phases and constraints discussed in Sec.1.1 and is

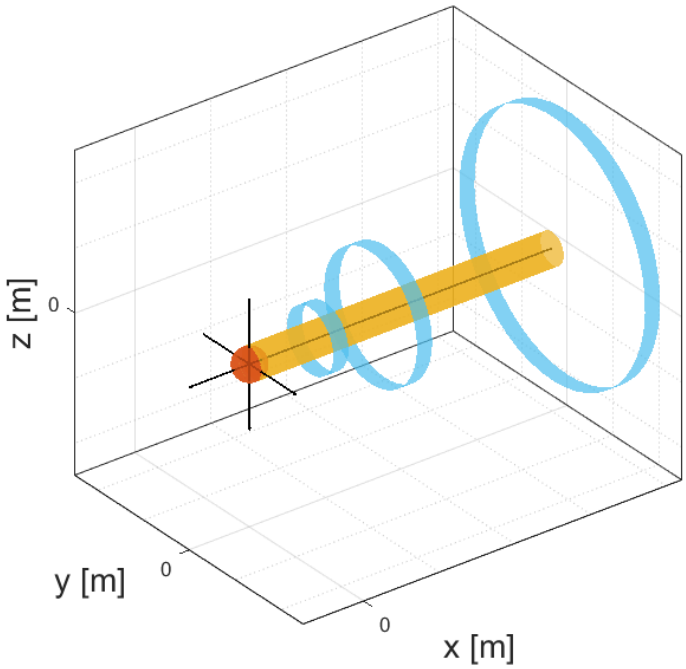

Figure 3.3.1: Approach geometry for FSM guidance, TAN frame

visualised in Fig.3.3.1. In particular:

- Based on the definition of the cross-track size of a KOZ around the target position (in red), a never-to-cross tube (orange) is considered around the along-track axis x in order to enforce PAS for the entirety of the approach.
- The approach trajectory is based on the definition of a series of holding states (or gates, in light blue) which are defined by two characteristics:
  - A waiting time, which requires the chaser to stationkeep (maintain its position and relative orbit) for a limited time, allowing to accomodate a variety of functions including switch of sensors for relative navigation, holding for convergence of filters or ground contact. In the presented test cases the waiting times are predefined in the initialisation script, but they can potentially be decided autonomously by the spacecraft and fed as input to the guidance function.
  - A geometric size, which defines the position of the center of the stationary relative orbit along x as well as the minimum distances (margins) to take from the never-to-cross tube when sizing the relative trajectory.
- It is fundamentally based on the autonomous manoeuvring capability of the

chaser to switch between two main states: a Walking Safe Ellipse (WSE) and a Stationary Safe Ellipse (SSE) state.

Fig.3.3.2 provides a visualisation of the structure of the implemented FSM, based on the Stateflow model. At the upper layer, three truth tables command the high-

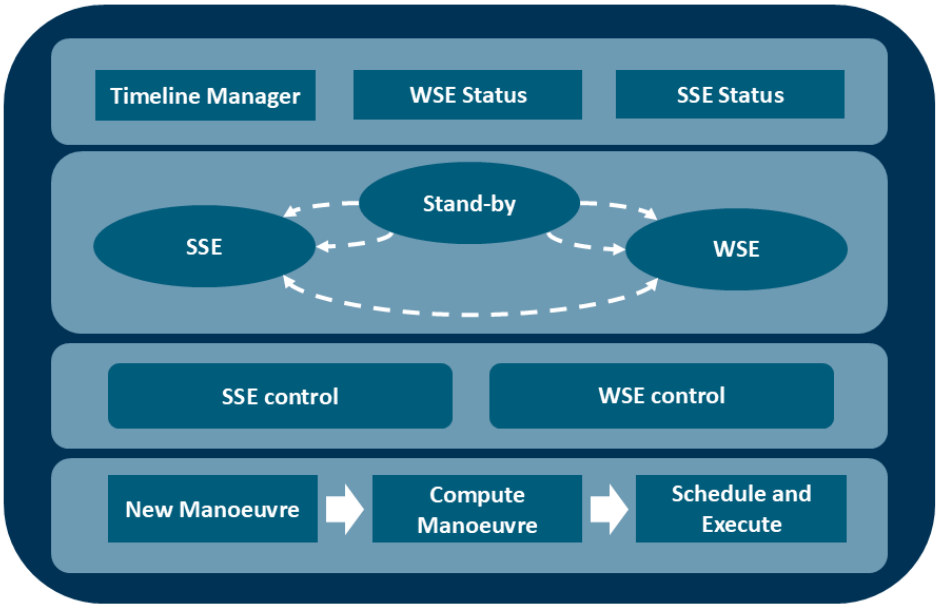

Figure 3.3.2: Conceptual structure of the FSM

level behaviour of the machine; the timeline manager evaluates whether the chaser spacecraft is outside or inside the prescribed next hold point based on the definition of error bands, which should be related to the expected control and navigation performance, whereas the WSE/SSE status classifies the current relative orbit. For example, an SSE characterised by an estimated drift $a\delta a$ higher than a prescribed threshold is termed as ”drifting”. The information from the higher layer is then used as in the following:

- Decisions from the timeline manager condition the transitions between the main states of the FSM, in practice commanding to stop or move the relative orbit in a specific direction. As it will be discussed in Sec.4, these decisions can also be based on concurring objectives such as estimation of differential drag effects.
- Classification from the WSE/SSE status truthtables is used to inform decisions in the control layer to choose the appropriate manoeuvre within the guidance library (see Sec.3.2).

Lastly, the lower layer implements manoeuvre computation and execution and

interfaces the guidance software with the thrusters model used to command the spacecraft, and will not be discussed in detail. Fig.3.3.3 illustrates the structure of the control layer for the WSE and SSE states. As it can be seen from the figure, both states

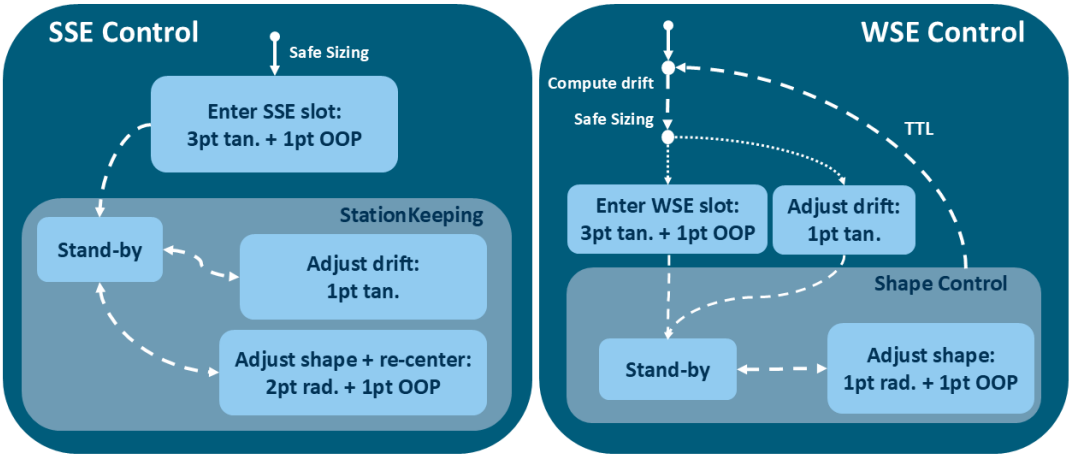

Figure 3.3.3: Structure of WSE and SSE control layer

benefit from the decoupling between drift and shape corrections obtained by adopting a velocity-aligned reference frame for the control; moreover, whenever both an IP and OOP manoeuvres are commanded, the relative eccentricity precompensation scheme illustrated in Eqs.3.10 is adopted. Further observations are discussed:

- Transitions to the stand-by (or waiting) states are triggered by completion of a selected manoeuvre scheme, communicated by the lowest layer in Fig.3.3.2.
- ”Safe Sizing” refers to a call to a function that returns the relative eccentricity and inclination components based on user-defined margins to be maintained from the KOZ on the cross-track plane and the nominal drift.
- Given user-defined minimum and maximum drift values of the WSE, ”Compute drift” provides the necessary $a\delta a$ to reach the next hold point in a prescribed time. The function is called again if after the drifting time the SSE state has not been reached yet, triggered by temporal transition logic (TTL).

It is emphasized here that the presented approach can be explicitly tied to any specific mission timeline (defined in terms of, *e.g.*, holding and drifting periods), a feature that is particularly valuable for mission management and ground support of ongoing operations. The following subsections detail the external functions called by the FSM during SSE and WSE control.

Safe Relative Orbit Sizing

To ensure PAS for any eccentricity of the target orbit, safe relative orbit sizing is based on the described relative orbit C-elements (see Sec.2.1.5); in their dedicated section, it was shown how the inner bound of the family of orbits generated by different IP phasing α of the generalised eccentricity vector could be used to conservatively size the relative orbit. Based on Eq.2.25, the in-plane and out-of-plane dimensions can be computed as in the following:

$$\begin{aligned} C_{IP} &= |C_1| + (KOZ_Z + M_Z) \cdot (1+e)^2 \\ C_{OOP} &= (KOZ_Y + M_Y) \cdot (1+e) \end{aligned} \tag{3.39}$$

where C_1 can be computed on the nominal drift of the relative orbit and KOZ and M respectively refer to the keep-out-zone and the defined margin sizes of the next waypoint along a particular dimension. To choose a phasing for the vectors, it was decided to fix the OOP one to minimise stationkeeping effort against perturbations; in fact, as discussed in Sec.2.1.7, the effect of J_2 on the relative inclination vector is contained by adopting a configuration with $\delta i_x = 0$[6], which according to the ROE definition in Eq.2.19 implies having two orbits with the same inclination. This same choice has also been adopted in past technology demonstrations such as in [15] and [29]. From the direct mapping in Appendix A, this means that:

$$C_5 = -\sin\omega \cdot \delta i_y, \qquad C_6 = -\cos\omega \cdot \delta i_y \tag{3.40}$$

from which the phasing β can be computed according to Eq.2.24. The IP phasing α can then be fixed on either a parallel or anti-parallel condition, depending on the initial state. The C-element state vector can then be converted to the ROE set to be used to call the guidance manoeuvres.

Relative Drift Computation

As already introduced, this function is used by the FSM to compute the relative drift δa required to reach the next waypoint; in order to preserve efficiency against differential drag perturbations, the computation also accounts for the estimated change rate $\delta\dot{a}$. The evolution of the relative mean argument of longitude becomes, according to the

[6] As illustrated in later sections, a different choice on the phasing of the IP/OOP vectors might be needed to enhance visibility on the target spacecraft to support vision-based navigation.

drag-perturbed STM in Appendix B:

$$\Delta\delta\lambda = -\frac{3}{2}n\tau\delta a_0 - \frac{3}{4}n\tau^2\delta\dot{a} \tag{3.41}$$

where $\tau = (t - t_0)$. The main ideas of the algorithm are the following:

1. A nominal user-defined drift period τ between two waypoints is considered and used to compute the relative drift required by inverting Eq.3.41.

2. Having defined limit values $a\delta a^{MIN}$ and $a\delta a^{MAX}$, if the absolute value of the relative drift $a\delta a_0$ to be commanded is either too high or too low the value is saturated and the drifting time is recomputed by solving Eq.3.41 for τ. Care must be taken in the presence of opposing differential drag ($\delta\dot{a} \cdot \Delta\delta\lambda > 0$) and of maximum saturation of the drift value, in which case it might be possible that the next waypoint cannot be reached with a single firing. By setting the discriminant of the quadratic Eq.3.41 equal to zero the maximum distance that can be travelled is found as:

   $$\Delta\delta\lambda^{MAX} = \frac{3}{4}\frac{n\delta a_0^2}{\delta\dot{a}} \tag{3.42}$$

   for which the drifting time can be computed.

3. The relative drift to command is used to safely size the relative orbit as explained in the previous section and the drifting time is used as argument of the TTL condition in Fig.3.3.3.

3.3.2 Time-Constrained Optimal Guidance

The previous section illustrated an approach to the rendezvous problem which is based on the idea of building a guidance law using a set of computationally simple rules in such a way to accommodate high level requirements and, at the same time, embed some level of fuel-optimality with the choice of the manoeuvring schemes and the way perturbations effects are mitigated. A different approach, more shifted towards the optimization paradigm, was developed for the autonomous manoeuvre planner module of the AVANTI experiment within the DLR FireBird mission [29] and is further investigated and expanded in the following. The main idea is to split the overall reconfiguration problem (from an initial point in the ROE space $\mathbf{P}_0$ to a final $\mathbf{P}_F$, where $\mathbf{P}(t) = a\delta\boldsymbol{\alpha}(t)$) into two distinct layers:

1. A guidance layer computes the intermediate configurations $\mathbf{P}_i$ to be reached at discretised times t_i by minimising a functional which represents the Δv cost of the overall plan. Because the problem requires to plan over long time windows, complex propagation models can be used to account for long-term, non-Keplerian effects.

2. A control layer is used to provide local solutions to the i-th problem of establishing any intermediate configuration $\mathbf{P}_i$ in a limited time horizon. Because these are relatively short reconfiguration intervals, this layer can assume pure Keplerian motion to obtain closed form formulas for the single manoeuvres, as done in Sec.3.2.

Fig.3.3.4 provides a visualization of the problem at hand over a set of discretized $m+1$ time nodes; from the guidance point of view, the ROE describing the trajectory evolve in a continuous way until a discontinuity at the end of each time interval takes place. The functional to be optimised is written by assuming that the IP reconfigurations are

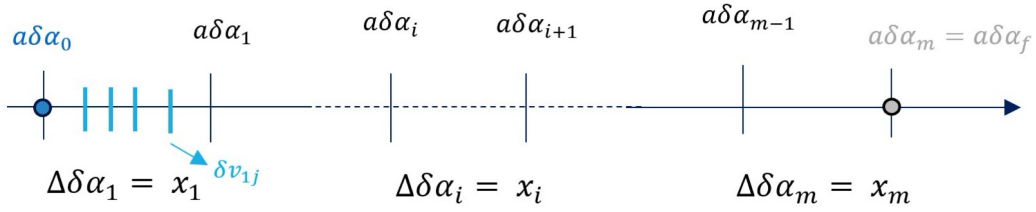

Figure 3.3.4: Representation of the decoupled guidance and control problem [3]

achieved by only using tangential burns, which allows to correlate the minimisation of the Δv cost of a manoeuvre to the distance between two points in the ROE space. This is a conclusion which is provided based on the expression of the minimum Δv bound in [30] for near-circular, and which was extended to the eccentric case in [10]. The functional then takes the following form:

$$J_{\text{plan}} = \sum_{i=1}^{m} (\Delta||\delta\mathbf{i}||)_i^2 + \sum_{i=1}^{m} (\Delta\delta a)_i^2 + \sum_{i=1}^{m} (\Delta\delta\lambda)_i^2 + \sum_{i=1}^{m} (\Delta||\delta\mathbf{e}||)_i^2 \tag{3.43}$$

The single variations in ROE $a\Delta\delta\boldsymbol{\alpha}_i$ which take place at each discretised time t_i become the control variables and the complete reconfiguration over the entire interval ($t_0 \rightarrow t_F$) can be written as:

$$\mathbf{P}_F = \Phi_{0F}\mathbf{P}_0 + \sum_{i=1}^{m} \Phi_{iF} \cdot a\Delta\delta\boldsymbol{\alpha}_i \tag{3.44}$$

By imposing that the last jump reaches the desired $\mathbf{P}_F$ state, it can be expressed as a function of the previous $m-1$ jumps:

$$a\Delta\delta\boldsymbol{\alpha}_M = P + H\mathbf{x} \tag{3.45}$$

where the following quantities have been defined:

$$\begin{aligned} \mathbf{x} &= [a\Delta\delta\boldsymbol{\alpha}_1, ..., a\Delta\delta\boldsymbol{\alpha}_{M-1}] \\ P &= \Phi_{MF}^{-1}[a\delta\boldsymbol{\alpha}_F - \Phi_{0F} \cdot a\delta\boldsymbol{\alpha}_0] \\ H &= -\Phi_{MF}^{-1}[\Phi_{1F}, \Phi_{2F}, ..., \Phi_{M-1,F}] \end{aligned} \tag{3.46}$$

The $\mathbf{x}$ vector has been defined to include all jumps except the last one. By using Eq.3.45, the cost function can be re-written as:

$$J_{\text{plan}} = \mathbf{x}^T\mathbf{x} + (P + H\mathbf{x})^T(P + H\mathbf{x}) \tag{3.47}$$

The strategy of only minimising the functional on the first $m-1$ jumps simplifies the optimisation problem by transforming the constrained formulation into an unconstrained one; moreover, by preserving the convexity of J, the optimum vector $\mathbf{x}$ is found by simply solving a linear system:

$$\begin{aligned} &\frac{\partial J}{\partial \mathbf{x}^T} = \mathbf{o} \quad \rightarrow \quad G\mathbf{x} + D = \mathbf{o} \\ &G = I + H^T H, \qquad D = H^T P \end{aligned} \tag{3.48}$$

Solving for $\mathbf{x}$ allows finding the vector containing the variations required at the different time nodes t_i which minimise the path in the ROE space while following the dynamics described by the STM Φ; moreover, the last variation, not included in $\mathbf{x}$, can be retrieved using Eq.3.45.

Inclusion of Differential Drag Effects

In the original publication ([29]) the effect of differential drag is introduced in the linear model of the relative dynamics as only a linear variation of the relative semi-major axis; the current section provides a general framework which allows to integrate a more complex perturbation model as the one reported in Appendix B, which requires the ROE state to be augmented by the constant estimates of the change rates of δa, δe_x^*

and δe_y^*. The variations taking place on the discretised time nodes become:

$$\mathbf{x}^* = \begin{bmatrix} a\Delta\delta\boldsymbol{\alpha}_{aug}^1 \\ ... \\ a\Delta\delta\boldsymbol{\alpha}_{aug}^{m-1} \end{bmatrix}, \qquad \text{where} \quad \Delta\delta\boldsymbol{\alpha}_{aug}^i = \begin{bmatrix} \mathbf{x}_i \\ \mathbf{o}_{3\times1} \end{bmatrix} \tag{3.49}$$

Where $\mathbf{x}_i$ is the actual ROE jump being optimised in the previous section; it only makes sense to re-write the cost function only with respect to $\mathbf{x}$ rather than the full $\mathbf{x}^*$ vector. The cost function can be expressed as:

$$\begin{aligned} J_{\text{plan}} &= \mathbf{x}^{*T}\mathbf{x}^* + (P + H\mathbf{x}^*)^T Q(P + H\mathbf{x}^*) \\ &= \mathbf{x}^{*T}(I + H^T Q H)\mathbf{x}^* + \mathbf{x}^{*T}(H^T(Q^T + Q)P) + (P^T Q P) \end{aligned} \tag{3.50}$$

where a diagonal weight matrix Q has been introduced to provide control on the amplitude of the last jump. The expressions for P and H are the same as previously provided in Eqs.3.46, except the initial/final ROE include the augmenting derivatives and the STM are size 9×9. The problem can be re-written as a function of $\mathbf{x}$ as in the following:

$$\begin{aligned} J_{\text{plan}} &= \mathbf{x}^T(I + B_R H^T Q H B_C)\mathbf{x} + \mathbf{x}^T(B_R H^T(Q^T + Q)P) + (P^T Q P) \\ B_R^{6n\times9n} &= \begin{bmatrix} I_{6\times9} & \mathbf{o} & \mathbf{o} \\ \mathbf{o} & ... & \mathbf{o} \\ \mathbf{o} & \mathbf{o} & I_{6\times9} \end{bmatrix}, \qquad B_C^{9n\times6n} = \begin{bmatrix} I_{9\times6} & \mathbf{o} & \mathbf{o} \\ \mathbf{o} & ... & \mathbf{o} \\ \mathbf{o} & \mathbf{o} & I_{9\times6} \end{bmatrix} \end{aligned} \tag{3.51}$$

The linear system matrices (defined in Eq.3.48) are re-defined as:

$$G = 2I + 2B_R H^T Q H B_C, \qquad D = B_R H^T(Q^T + Q)P \tag{3.52}$$

An example is provided in the following to compare the optimal solutions with and without differential drag effects according to the generalised formulation provided in Eq.3.52, with absolute and relative orbit data given in Tab.3.3.1, based on the numerical test case provided in [29]. The constant change rates assumed for the augmented part of the ROE are taken as $\delta\dot{a} = 5.2 \cdot 10^{-11}, \delta\dot{e}_x^* = 4.1 \cdot 10^{-10}, \delta\dot{e}_y^* = 1.3 \cdot 10^{-10}$ [1/s]. As a first observation, it is remarked that these test cases are focused only on the guidance layer, meaning that the changes in ROE which would be realised using the implemented impulsive manoeuvres are assumed to happen instantaneously at the end

Table 3.3.1: Initial and final data for optimal guidance test

a [km]	e [-]	i [^{o}]	Ω [^{o}]	ω [^{o}]	f_0 [^{o}]	t_{nodes} [T_{orbit}]
6870	0	80	120	0	0	[0, 5, 13, 18]

ROE [m]	$a\delta a$	$a\delta\lambda$	$a\delta e_x$	$a\delta e_y$	$a\delta i_x$	$a\delta i_y$
Initial	5	10000	-50	-250	-30	200
Aimed	0	3000	0	-100	0	100

of each discretised interval (see Fig.3.3.4).

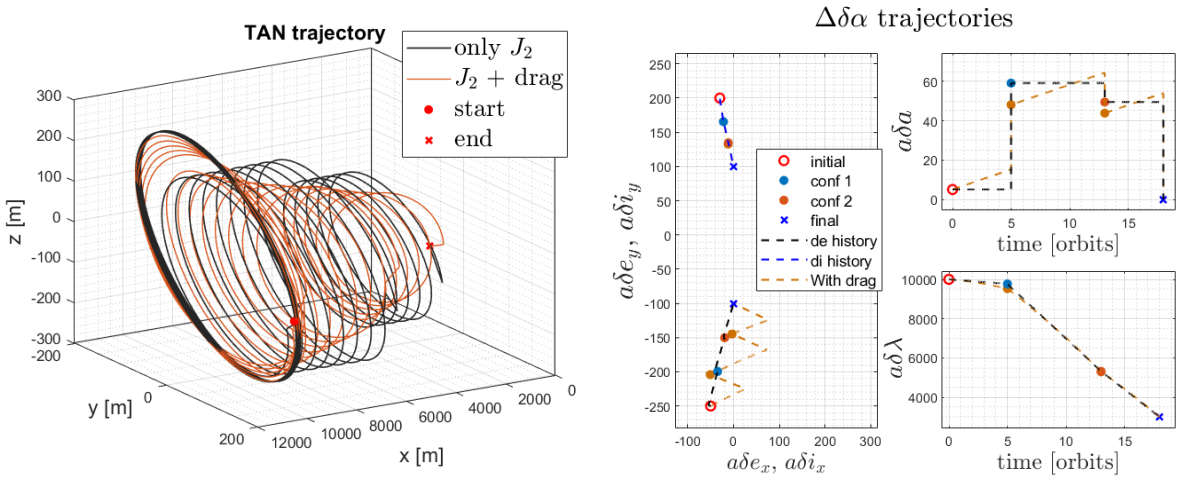

(a) Cartesian trajectories

(b) ROE trajectories

Figure 3.3.5: Comparison of optimal guidance results with differential drag

The second observation is on the effects yielded by the differential drag on the ROE:

- As expected from past discussions, the semi-major axis follows a linear trend instead of a constant one. Although not very visible from the figure, this is reflected into a quadratic trend of $\delta\lambda$.
- As it can clearly be noticed from the plots, residual drag has a negligible effect on the evolution of $\delta\mathbf{i}$ when compared to $\delta\mathbf{e}$; this differential effect might create intermediate relative orbits which lose their PAS characteristic.

The concept of safety enforcement is not directly addressed in the original publication, but it is also underlined how the intermediate configurations found by the planner are expected to lie on $\mathbf{P}_0 - \mathbf{P}_F$ line in the relative eccentricity and inclination space. The

following section discusses the use of a penalty function to introduce a constraint at the planning level to maintain safety in the presence of non-circular target, disturbing accelerations and unsafe initial conditions.

Safety Enhancement

The idea of embedding a constraint into the optimal guidance formulation through a penalty function was also adopted in [4] to improve the observability property of the angles-only relative navigation problem. The main idea of the penalty function method is to avoid constraining the optimisation problem [7] (minimization of J subject to $f(y) = 0$) by considering the minimization of:

$$\hat{J} = J(y) + K||f(y)||^2 \tag{3.53}$$

where K is very large. If the new $\hat{J}$ attains a minimum at y^*, it is reasonable to expect that:

$$f(y^*) \approx 0, \qquad \lim_{K\to\infty} y^* \to y_0 \tag{3.54}$$

where y_0 is the solution of the constrained problem. To retain an analytical solution of the penalised problem the penalty function is written as a quadratic form of $\mathbf{x}$. At each intermediate node q, the penalty function is defined to find a minimum by driving the relative $\delta\mathbf{e}$ and $\delta\mathbf{i}$ in parallel (or anti-parallel) configuration:

$$\begin{aligned} J_q^p = \mp(\delta\mathbf{e}_q)^T(\delta\mathbf{i}_q) = \mp\left(B_E\left(\Phi_{0q}\delta\boldsymbol{\alpha}_0 + D_qC_q\mathbf{x}^*\frac{1}{a}\right)\right)^T\left(B_I\left(\Phi_{0q}\delta\boldsymbol{\alpha}_0 + D_qC_q\mathbf{x}^*\frac{1}{a}\right)\right) \\ B_E = [0_{2\times2},\ I_{2\times2},\ 0_{2\times5}], \quad B_I = [0_{2\times4},\ I_{2\times2},\ 0_{2\times3}], \\ D_q = [\Phi_{1q}, ..., \Phi_{q-1,q}, I], \quad C_q = [I_{9q\times9q},\ 0_{9q\times9(n-q)}] \end{aligned} \tag{3.55}$$

where q is the number of the current intermediate time node and n is the total number of intermediate nodes. The problem is casted once again in a form which is only a function of $\mathbf{x}$. By re-writing the penalty term as $J_q^p = L_{0q} + \mathbf{x}^T L_{1q} + \frac{\mathbf{x}^T}{2} L_{2q}\mathbf{x}$ and deriving the new analytical solution to the linear problem is found as:

$$\begin{aligned} G_{penalized} = G + \sum_q \omega_q L_{2q}, \ \text{ where } \ L_{2q} = \frac{2}{a^2}(B_R C_q^T D_q^T B_E^T B_I D_q C_q B_C) \\ D_{penalized} = D + \sum_q \omega_q L_{1q}, \ \text{ where } \ L_{1q} = \frac{1}{a}(B_R C_q^T D_q^T (B_I^T B_E + B_E^T B_I)\Phi_{0q}\delta\boldsymbol{\alpha}_0) \end{aligned} \tag{3.56}$$

where ω_q is a weight factor introduced to properly scale the penalty term. According to the discussion presented in Sec.2.1.5, the safety formulation can easily be extended to eccentric target orbits using the following definition of the penalty function:

$$\begin{gathered} J_q^p = \mp(C_{23})^T(C_{56}) = \mp\left(B_{CE}\frac{\partial C}{\partial \delta\boldsymbol{\alpha}}B_A\delta\boldsymbol{\alpha}\right)^T\left(B_{CI}\frac{\partial C}{\partial \delta\boldsymbol{\alpha}}B_A\delta\boldsymbol{\alpha}\right) \\ B_A = [I_{6\times6},\ 0_{6\times3}], \quad B_{CE} = [0_{2\times1},\ I_{2\times2},\ 0_{2\times3}], \quad B_{CI} = [0_{2\times4},\ I_{2\times2}] \end{gathered} \tag{3.57}$$

Where the linear map between the ROE sets can be found in Appendix A. This reformulation allows to use the same exact formulas as provided in Eqs.3.56 by substituting:

$$B_E = B_{CE}\frac{\partial C}{\partial \delta\boldsymbol{\alpha}}B_A, \quad B_I = B_{CI}\frac{\partial C}{\partial \delta\boldsymbol{\alpha}}B_A \tag{3.58}$$

Finally, the weighting factor can be defined, in a similar way to [4], as:

$$\omega_q = \frac{J_{\text{opt}}k_p}{||C_{23}^q|| \cdot ||C_{56}^q||n_q} \tag{3.59}$$

where the value of the cost function J_{opt} and the magnitudes of C_{23} and C_{56} at each node are obtained by a pre-computation of the optimal solution without including the penalty term, n_q is the number of intermediate nodes and k_p is an arbitrary parameter. An example is provided in the following to illustrate the effect of the penalty function. As seen from Fig.3.3.6, the introduction of the penalty function has the effect to

Table 3.3.2: Initial and final data for optimal guidance test with penalty function

a [km]	e [-]	i [^{o}]	Ω [^{o}]	ω [^{o}]	f_0 [^{o}]	t_{nodes} [T_{orbit}]	k_ω
8348	0.2	1	120	120	180	[0, 1, 6, 11]	0.0039

C-elements [m]	C_1	C_2	C_3	C_4	C_5	C_6
Initial	5	-30	-250	-10000	0	200
Aimed	0	0	-100	-2000	0	100

improve PAS of the intermediate orbit with respect to the optimal trajectory. As expected, this is obtained by only slightly deviating the minimum path in the $\delta\mathbf{e}/\delta\mathbf{i}$ plane, which entails a differently phased relative orbit. In the provided test case, this increases the cost of the plan J by about 0.0029%.

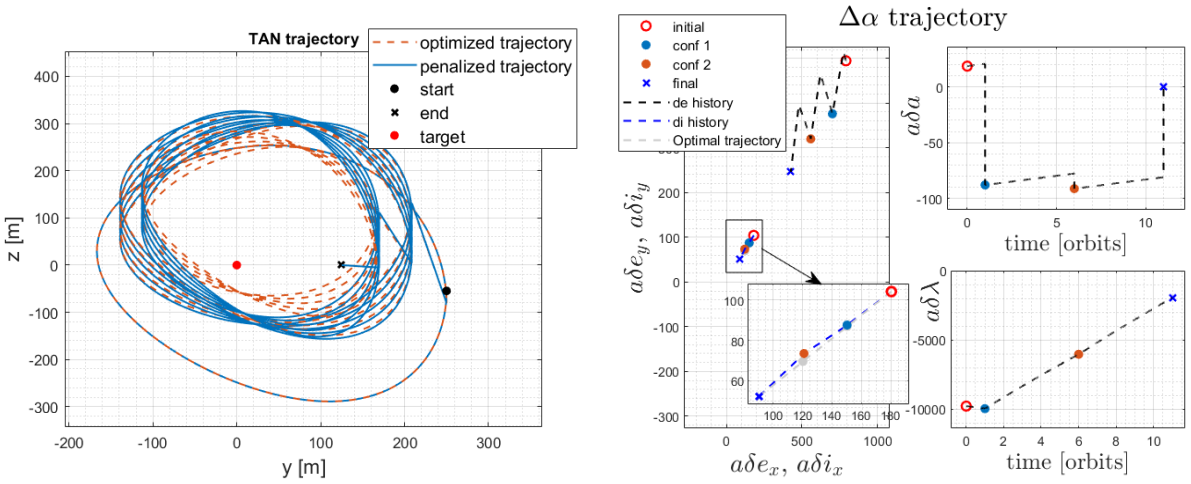

(a) Cartesian trajectories (b) ROE trajectories

Figure 3.3.6: Comparison of optimal guidance results with penalty function

The presented method enables autonomous manoeuvring of the chaser and is based on the definition of a list of time nodes. Although the method would still work by just defining an initial and final time (a mode which is referred to as "minimum Δv mode"), these discretised time intervals allow to include high level requirements into the autonomous mission planning; for example, a single time node can be defined as the end of a period in which the chaser is allowed to manoeuvre. These feasible periods can be allocated by a scheduler knowing the maximum time needed for the ROE reconfiguration, a characteristic which has been highlighted during the development of closed-form manoeuvring schemes.

3.3.3 Information-Based Guidance for Inspection

This section aims to investigate a possible solution to the inspection of an uncooperative target satellite during a rendezvous mission. An efficient inspection of a resident space object is a key aspect to enable target pose estimation, observation of its key features as well as following close-proximity operations, which might involve docking, approach and capture for servicing and/or removal; the objective of this phase is to acquire measurements of the target state and observe features of interest based on the considered mission requirements.

For this problem, path-planning formulations which aim to ensure safety operations as well as to improve the measurements taken during the inspection phase are considered; the favoured approach is one which merges passive safety to useful

observation trajectories and which can still make use of the developed impulsive guidance manoeuvres from Sec.3.2. A variety of approaches to the problem have been found from the literature, and the ones considered are mostly oriented towards a Sampling-Based Planning (SBP) logic, a strategy which has been largely applied to robotic motion planning problems [20]. These planners operate by growing a ”tree” or ”graph” (by dynamically propagating) from sample points from an N-dimensional space, which can be limited to include difficult constraints like collision avoidance. A further common feature between this group of problems is the formulation of an information metric, which can quantify the cumulative quality of the observations over time to guide the path planning problem.

- Reference [44] proposes a GNC architecture for multiple inspecting spacecraft which performs the choice of a ”passive relative orbit” (PRO) for inspection by making use of an information-based optimal control problem, which seeks the minimisation of an ”information cost” term related to the quality of vision-based sensor measurements of Points Of Interest (POI). Prior evaluation of the quality of future observations is to be based on a ray-casting database, which contains a visibility map on the target geometry parametrized on the spherical coordinates of the chaser position. The choice of the next inspecting orbit is based on a sequential greedy approach, favoured over a combinatorial optimisation for computational efficiency.

- Reference [5] adopts the high-level concept from [44] for the close inspection guidance of the non-collaborative carrier spacecraft within the SpEye demonstration missions; in this case, an analytic PAS tool based on the minimum one-orbit distance in the ROE space is used to generate a collision-free candidate sample set.

- Reference [8] also bases its path planning solution on a series of POI on the target, formulating a mission completion index based on the cumulative time spent observing each feature. A major difference from the previous approaches is in the formulation of the planning strategy, which samples the 4-dimensional space formed by the control input variables (components of the Δv to enter an inspection leg and duration of the inspection) rather than the relative state space. Unsafe trajectories are discarded by linear propagation of the covariance matrix, which allows a straightforward inclusion of manoeuvre execution errors and

orbital perturbations. Another interesting feature is the search over the sample space which makes use of local mesh-refining techniques to converge to the most promising inspection leg.

- Although more oriented towards free-flyers control for cluttered environments, reference [20] also makes use of a multi-layered GNC architecture, where the high-level planner is based on kino-RRT[7], a variant of the popular rapidly exploring random trees algorithm which produces a long-term collision-free path and the mid-level planner performs a receding-horizon, information-aware planning based on the minimisation of the trace of the inverse of the "Fisher Information Matrix", a metric which measures the amount of information given by an observation y about a specific parameter of interest.

The strategy which is adopted in the following inherits the common idea of a multi-level guidance strategy to choose and follow observation-optimal trajectories to track specific POI. In particular:

1. The information cost function is based on the work of [44] and similar steps are followed for the offline generation of a ray-casting database using the rough CAD model of the target spacecraft.
2. The sample space is defined using ROE as done in [5] to exploit their geometric intuition and quick insight into collision checking, but C-elements are employed to extend the formulation to eccentric cases.
3. The idea of locally refining the sample through a meshing function as suggested in [8] is considered to improve the inspection results.

Offline Visibility Database Generation

As introduced, the first step of the algorithm is based on the pre-computation of a ray-casting database. This is realised in the form of a look-up table which can be used to quickly obtain visibility conditions as well as observation angles, intended as the angle between an incident ray and the normal of an element of the geometry. In practice, the database is created by cycling the ray source over different positions in the spherical space around the target and by employing a function, made available by the

[7] *Kinodynamic Rapidly-Exploring Random Tree*, a sampling-based motion planning algorithm that incrementally builds a tree in the state space to efficiently explore feasible paths accounting for both kinematic and dynamic constraints.

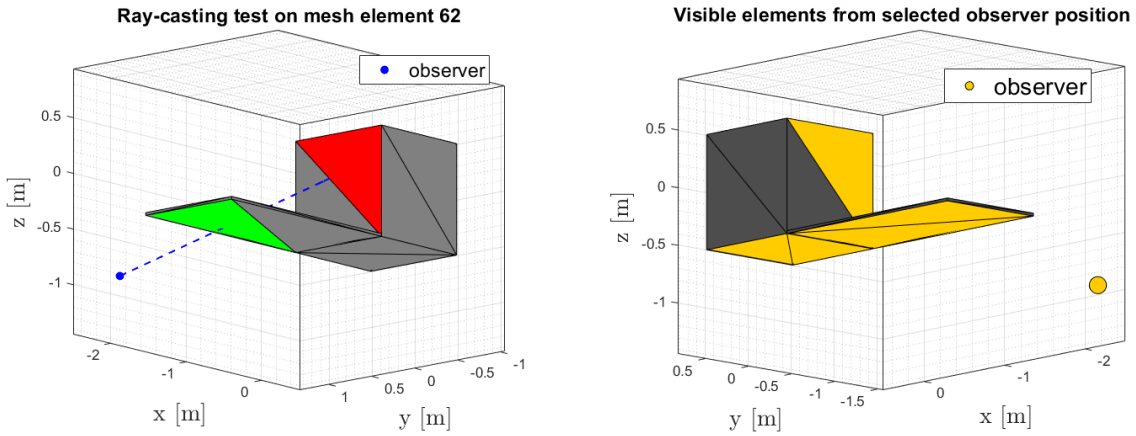

Figure 3.3.7: Target spacecraft geometric visibility check based on ray-casting

department at OHB, to assess visibility of each mesh element; as illustrated in the left of Fig.3.3.7, occlusion takes place whenever the ray source encounters another element (in green) before another one (in red). The resulting look-up table allows, given the ray source position in the body frame of the target, to obtain a binary map specifying which elements are visible (in yellow in Fig.3.3.7) as well as the discussed related observation angles.

Sample Set Generation

As introduced, the sample space over which the planning algorithm needs to search is built on the relative C-orbit elements; the main advantage related to this choice is the possibility of easily discarding unsafe trajectories thanks to the straightforward geometric PAS condition. In particular, the generation of a safe sample of points takes place in two phases:

1. The first step consists in taking a random sample of N_{sample} points by limiting the maximum absolute value of the relative drift allowed during inspection and the maximum in-plane and out-of-plane size of the relative orbit. The last two conditions generate a uniform point cloud in the C_2/C_3 and C_5/C_6 planes within circles of radii equal to the specified sizes; the maximum drift $a\delta a$ on the other hand sets a lower and upper boundary on the C_1 element (see Eqs.2.22):

$$\begin{aligned} C_1^{max} &= \frac{|a\delta a^{max}| \cdot \eta^4 + 2eC_2}{1+e^2} \\ C_1^{min} &= \frac{-|a\delta a^{max}| \cdot \eta^4 + 2eC_2}{1+e^2} \end{aligned} \tag{3.60}$$

2. The second step entails the simple application of the geometric PAS condition over the generated points, which, as already discussed, consists in imposing the collinearity condition between the C_{23} and C_{56} vectors (generalised relative E/I separation) and fixing minimum IP and OOP sizes according to the safe relative orbit sizing criterion from Eqs.3.3.9.

e	**0/0.5**
$a\delta a^{\max}$ [m]	0
$C_{IP}^{\max}$ [m]	100
$C_{OOP}^{\max}$ [m]	100
N_{sample}	10^6

KOZ_Z [m]	10
KOZ_Y [m]	10
M_Z [m]	5
M_Y [m]	5
collinearity$_{threshold}$ [^{o}]	5

Table 3.3.3: Data for random sampling (left) and safe orbit definition (right)

Tab.3.3.3 reports the data for the safe sample set generation shown in Fig.3.3.8.

For the circular case, the results align with the near-circular sample generation using quasi-non-singular ROE presented in [5], the main difference being the fact that instead of considering propagation of the relative state covariance, geometric margins and thresholds are used. As the eccentricity grows, the imposed constraints also grow in complexity (the lower boundary of C_{23} becomes quadratic in (1+e), instead the one of C_{56} is linear in (1+e) and this is reflected in the resulting sample shapes. Another aspect that needs to be pointed out is the fact that the element C_4, which represents the along track position of the relative orbit, is not constrained by the current formulation and therefore represents a degree of freedom in the inspection algorithm.

Information Cost Definition

Provided that the ray-casting database and a safe trajectories pool is available, a greedy selection of the next best inspection orbit is carried out by defining a list of Points Of Interest (POI) on the available rough prior model of the target spacecraft. Initially, the pose estimate of the POI is assumed to have a high variance implying a bad model quality; the objective is to minimise their estimation variance using the onboard sensors. By considering a candidate trajectory, discretised on the inspecting positions r_i of the chaser (which is assumed to be target-pointing) the information cost

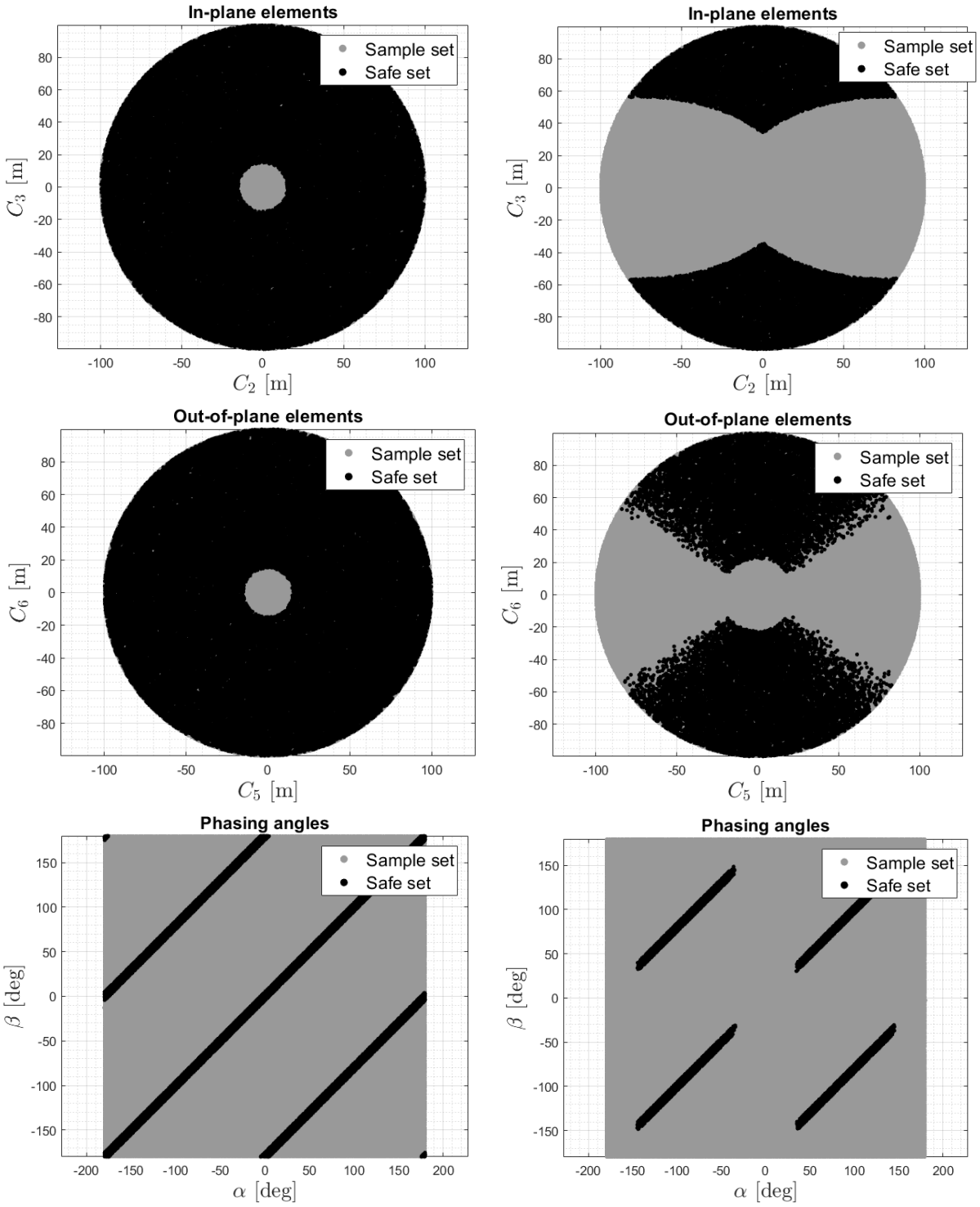

Figure 3.3.8: Sample set generation with $e = 0$ (left column) and $e = 0.5$ (right column)

associated with the j-th POI is defined as:

$$IC_{POI,j} = \left[\sigma_{0,j}^{-1} + \sum_{r_i} \sigma(r_i, d_{POI,j})^{-1} \right]^{-1} \tag{3.61}$$

where the term $\sigma_{0,j}$ represents prior estimation variance of the j-th POI and the second term gives the additional pose estimation confidence yielded by observing the point at the discretised positions. The total information cost can be obtained by taking the summation of IC over all POI, with eventual weighting factors $\omega_{POI,j}$ to model the relative observation importance of each. The variance of the observation, defined for a visual-based RGB camera sensor, can be modelled as [5][44]:

$$\sigma(r_i, d_{POI,j}) = \begin{cases} ||r_i - d_{POI,j}||^2 (2 - \cos\alpha), & \text{if visible and illuminated} \\ \infty, & \text{otherwise} \end{cases} \tag{3.62}$$

where the term $(2 - \cos\alpha)$ models the cosine behaviour of the illumination intensity on an ideal diffusive reflective surface. Apart from occulted elements as defined from the ray-casting database, non-visibility of a POI may also be given by an out-of-range distance, based on the considered sensor performance. Orbital eclipses are also considered for "non-visible" cases, as they are easily predicted by a simple geometric check in ECI knowing the Sun position and the current orbital elements.

In practice, having selected an inspection trajectory from the sample space, this is linearly propagated using a STM over an inspection time period T_{insp} and Eq.3.61 is evaluated over each of the discretised N_{insp} positions.

Mesh-Refined Random Sampling

The previously defined safe sample set generation relies on a single uniform sampling in the delimited C-elements space with a subsequent application of the safety criterion; according to the formulations in [44] and [5], the safe sample points are then used to evaluate the information cost (see Eq.3.61) on each propagated and discretised trajectory and the one with the lowest result is selected. It can be argued that the selection process of the safe sample points could be improved by biasing the random sampling towards more promising (and safe) regions; this way, a smaller initial sample N_{sample} could yield less points to evaluate with a lower information cost. As introduced, this possible improvement is inspired by the work of [8], which is based on the use

of a locally-refining Delaunay mesh, introduced by Komendera et al. [40] to explore the reachability set of a manoeuvring spacecraft. The core idea is to use a Delaunay triangulation [66] on a set of random points to build a mesh; its elements are termed simplices, which are characterised by a number of $N + 1$ vertices, where N is the dimension of the considered sample space. Secondly, each simplex is scored using a scoring function which is based on the evaluation of the cost function on its vertices. The value of the score on the q-th simplex is given as:

$$J_q = V_q^{\eta_V} \left(1 + \eta_C \frac{C_{max} - C_q}{C_{max} - C_{min}} + \eta_G \frac{G_q}{G_{max}} \right) \tag{3.63}$$

where V_q is the volume of the simplex, C_q is the lowest cost function value among the simplex vertices, G_q is the maximum gradient score along the simplex edges, whereas the x_{max} and x_{min} values refer to the maximum and minimum values among all simplices of the mesh. The weighting factors η_V, η_C and η_G allow the scoring function to prioritise regions of the search space respectively characterised by large unexplored volumes, lower mission scores or large cost gradients across the simplex. The computed scores can then be used as the probabilities to sample a determined

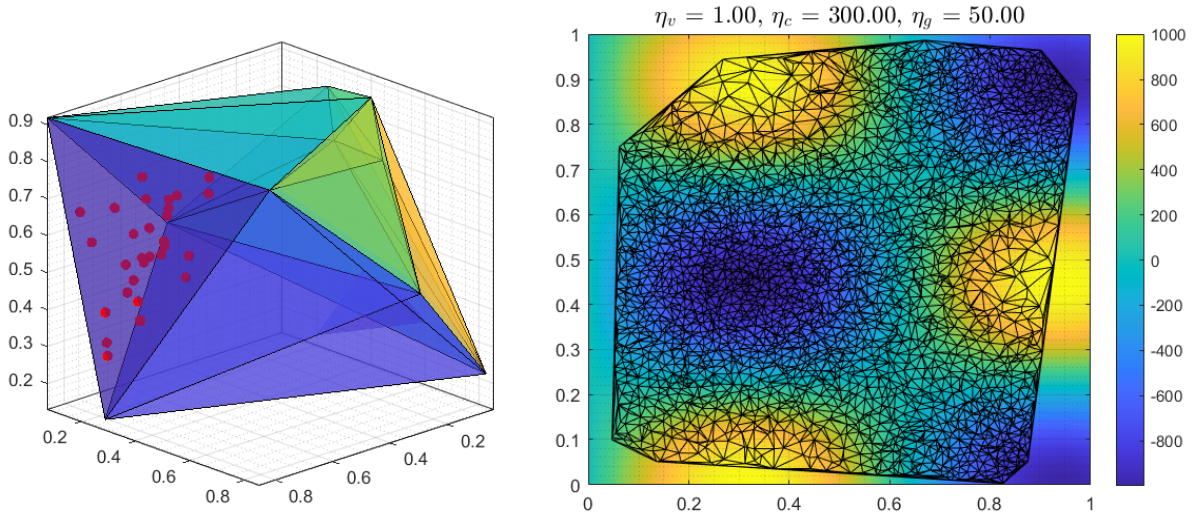

(a) Simplex sampling based on [33]

(b) $N_{\text{sample}} = 50$, $n_{\text{meshes}} = 15$, $n_{\text{refine}} = 200$

Figure 3.3.9: Mesh refining examples

number n_{refine} of new random points within the respective simplices; this last operation is based on the algorithm given in Listing 1.3 from [33]. The new points can be added to the original pool and the meshing and scoring process can be repeated a number of n_{mesh} times. With respect to the application of this technique to the current problem,

two further points need to be discussed:

- Evaluation of the information cost on the same point (vertex) is only done once;
- Unsafe points (according to the previously discussed PAS criterion) are neither discarded nor evaluated on the information cost; a very large value of the IC is instead assigned to them to drive the mesh refining process towards safe, promising regions.

A comparison between the mesh-refining and single sampling methods applied to the problem described in Tab.3.3.4 is provided in the following. IP and OOP inspection sizes as well as all margins are defined as in Tab.3.3.3, but in this case the inspection orbit is allowed to drift with $a\delta a^{max} = 5$m. Defined sensor performance include $d_{\max}$,

Table 3.3.4: Data for comparison between random sampling methods

a [km]	e [-]	i [^{o}]	Ω [^{o}]	ω [^{o}]	f_0 [^{o}]	LTAN	T_{insp} [orbits]	N_{insp}	C_4 [m]
36848	0.5	40	45	380	0	3:00 AM	2	100	0

σ_0	$d_{\max}$ [m]	$\alpha_{\text{obs}}^{max}$ [^{o}]	$\alpha_{\text{ill}}^{max}$ [^{o}]	η_V	η_C	η_G	n_{mesh}	n_{refine}	$N_{\text{sample}}^{\text{init}}$
10^8	100	80	85	1	300	150	3	50	100

$\alpha_{\text{obs}}^{max}$, $\alpha_{\text{ill}}^{max}$ which refer to maximum distances and observation/illumination angles under which a mesh element is considered observable. Two mesh elements on the

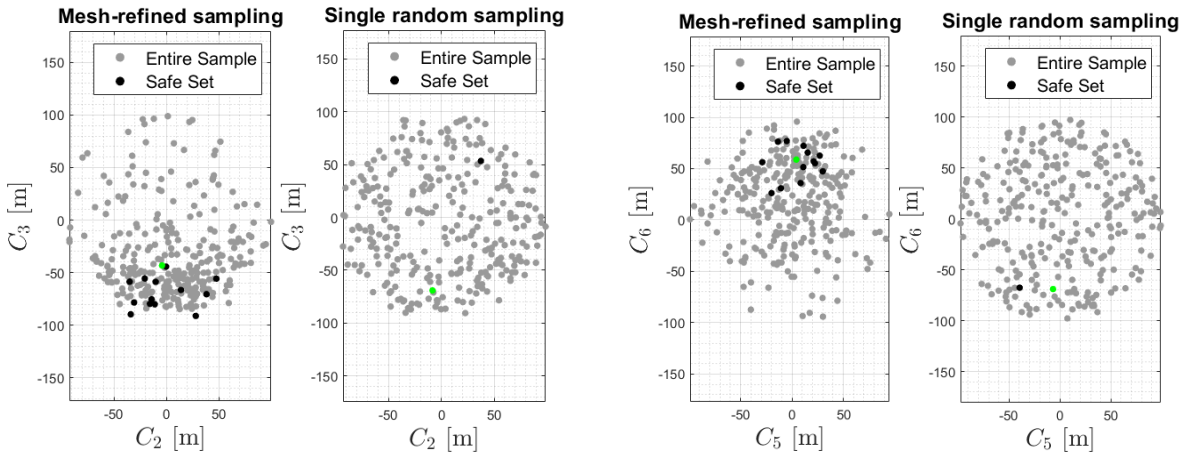

Figure 3.3.10: Comparison of mesh refining and single random sampling methods

target geometry are defined as POI, and the target attitude is assumed to be stable in the LVLH frame. $N_{\text{sample}}^{\text{init}}$ represents the initial number of points to be used in the first

step of the mesh refining method; for a fair comparison, the total number of samples to use for the single sampling method is computed as $N_{\text{sample}} = N^{\text{init}}_{\text{sample}} + n_{\text{mesh}} \cdot n_{\text{refine}}$. Looking at Fig.3.3.10, it is clear that by using a limited total number of random points (amounting to 250 in the example) the single random sampling method can only find very few feasible solutions, owing to the uniform distribution in the available sample space. On the other hand, the mesh-refining method orients newly sampled points toward the safer region of the space, which yields more candidate trajectories to choose from at the end. As for the information cost associated to the chosen trajectories (green points in Fig.3.3.10), the new method finds $IC_{MR} = 1.0433 \cdot 10^3$, whereas the original method reaches a minimum of $IC_{SS} = 8.2639 \cdot 10^3$. Although quite

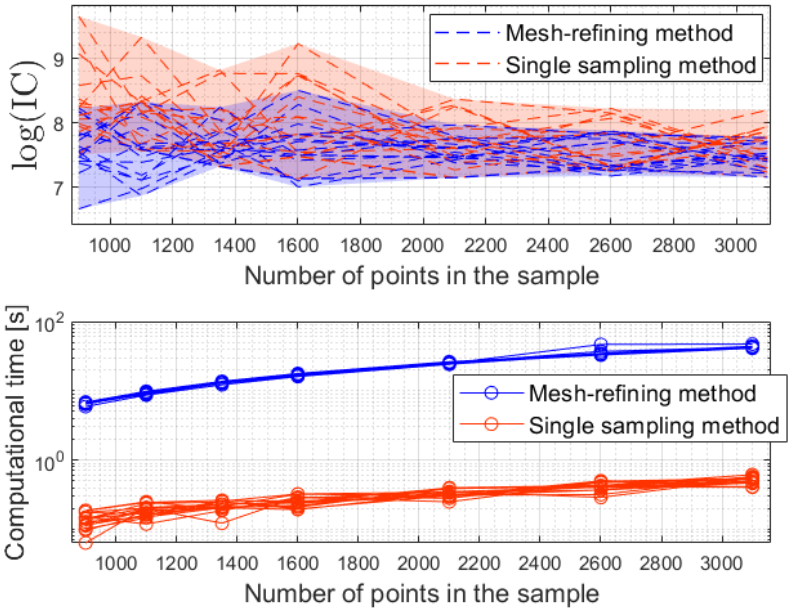

Figure 3.3.11: Comparison of sampling methods over different sample size

convenient when using a very small sample of points, one can easily imagine that the mesh-refining method has the drawback of an increased computational time. This can be observed in Fig.3.3.11, where the size of $N^{\text{init}}_{\text{sample}}$ is progressively increased, and multiple runs are tested for both algorithms. The tests are conducted using `MATLAB 2018b` software running on a machine with `Intel(R) Core(TM) i7-10850H` 2.70GHz with 32GB of RAM. It can be observed that the mesh-refining method provides more consistent results across different sample sizes, but with the cost of a significantly higher computational time. Ultimately, the trade-off leading to the choice of either method is mostly based on whether the optimisation step is conducted on-board or on-ground; in the second case, owing to greater computing power available, the mesh-refining method could be preferred because it provides better solutions using the same

number of samples.

Target Attitude Propagation

The previous sections assumed a target spacecraft with a fixed attitude in the LVLH frame. In a non-collaborative inspection scenario, typical of ADR missions, this assumption might result unrealistic. In fact, according to [48], defunct satellites (or space debris) are subject to three main types of torques: random, dissipative and orienting torques. The first type can either spin-up or spin-down the debris and include spurious activation of on-board actuators, momentum transfer from other debris and more; dissipative torques on the other hand tend to damp the rotational motion of the satellite through magnetic eddy currents in non-ferromagnetic materials mounted on-board. Lastly, orienting torques tend to move the object towards a periodic attitude, which can be aligned with the gravity gradient or the planet's magnetic field. For LEOs, which, as illustrated in Fig.1.1.1, represent the most cluttered region around Earth, it is expected that most of the objects have their dynamics dominated by dissipative and orienting torques. On the other hand, because magnetic and gravity gradient effects decrease to the third power of the orbit radius, it is expected that in higher orbits like MEO and GEO a large number of objects is in a fast rotation state [48].

The two main takeaways are that the planning algorithm should be able to account for the target's rotational motion, but it is also apparent that its efficacy may be undermined by the limited knowledge of the initial rotational conditions, including the various torques discussed. With respect to the previous implementation of the algorithm, the planner now needs to rotate the chaser and Sun relative positions from the LVLH frame to the target body frame before accessing the look-up table to assess visibility and illumination conditions. To represent the kinematics of a rigid body rotation, the singularity-free quaternion set (scalar-last) is chosen, which relates to the body angular velocity vector $\boldsymbol{\omega}$ through the following equation [42]:

$$\dot{\mathbf{q}} = \frac{1}{2} \begin{bmatrix} 0 & \omega_3 & -\omega_2 & \omega_1 \\ -\omega_3 & 0 & \omega_1 & \omega_2 \\ \omega_2 & -\omega_1 & 0 & \omega_3 \\ -\omega_1 & -\omega_2 & -\omega_3 & 0 \end{bmatrix} \mathbf{q} \tag{3.64}$$

Assuming rigid body dynamics, the angular velocity may be obtained upon integration

of the Euler's rotational equations:

$$J\dot{\boldsymbol{\omega}} = -\begin{bmatrix} 0 & -\omega_3 & \omega_2 \\ \omega_3 & 0 & -\omega_1 \\ -\omega_2 & \omega_1 & 0 \end{bmatrix} J\boldsymbol{\omega} + \boldsymbol{L} \tag{3.65}$$

where J is a general inertia matrix and $\boldsymbol{L}$ is the external torque acting on the spacecraft. By integrating Eqs.3.65 and Eqs.3.64 over time, it is possible to obtain the target attitude at each desired instant. The only external torque modelled in the propagation is the gravity gradient, which can be expressed at each instant as [42]:

$$\mathbf{L}_{gg} = 3\frac{\mu}{r^3}\hat{\mathbf{r}}_B \times (J\hat{\mathbf{r}}_B), \qquad \hat{\mathbf{r}}_B = DCM_{ECI2BF}\frac{\mathbf{r}_{ECI}}{r} \tag{3.66}$$

where DCM_{ECI2BF} is the direction cosine matrix expressing the rotation from ECI to body frame, which is easily obtained from the current quaternion vector. A test of the planning algorithm for a target in a free rotation state is presented below, with the same base data as Tab.3.3.4, with the only difference being an inspection period T_{insp} of just one orbit; additional data for attitude propagation is provided in Tab.3.3.5. Fig.3.3.12

Table 3.3.5: Data for target attitude propagation

ω_0 [1/s]	q_0	$J\ [kg \cdot m^2]$
$\begin{bmatrix} 0 \\ 0 \\ 0 \end{bmatrix}$	$\begin{bmatrix} 0 & 0 & 0 & 1 \end{bmatrix}^T$	$\begin{bmatrix} 2000 & 7.4 & 47.8 \\ 7.4 & 4000 & 17.9 \\ 47.8 & 17.9 & 3000 \end{bmatrix}$

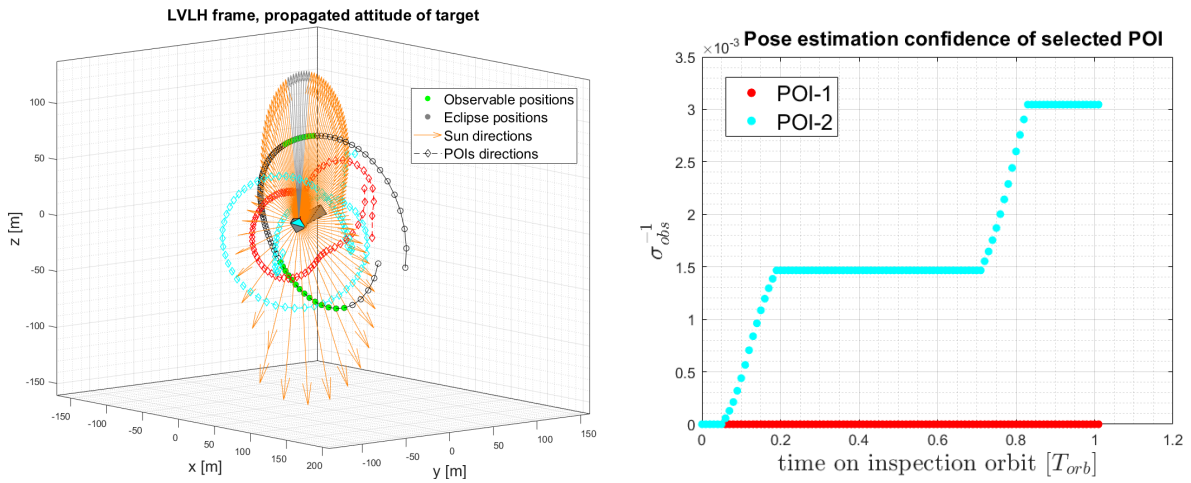

Figure 3.3.12: Inspection results on rotating target spacecraft (not in scale)

reports the inspection results of the trajectory obtained using the mesh-refinement method on the problem at hand; on the left, a visualization of the LVLH relative motion is provided. On a single orbit period, the planner orients the relative orbit in such a way that two observation windows (discretised green points) allow measurements to be taken. On the right of Fig.3.3.12, the pose estimation confidence (inverse of the observation variance) for the two considered POI is reported. It can be noticed that one of two is never properly observed, owing to unfavourable relative motion conditions; moreover, as shown in Fig.3.3.7, the red POI is more prone to be shadowed by the solar panel. The same inspection problem is optimised by considering fixed attitude of the target in LVLH frame, and the results are reported in Fig.3.3.13. In this second case,

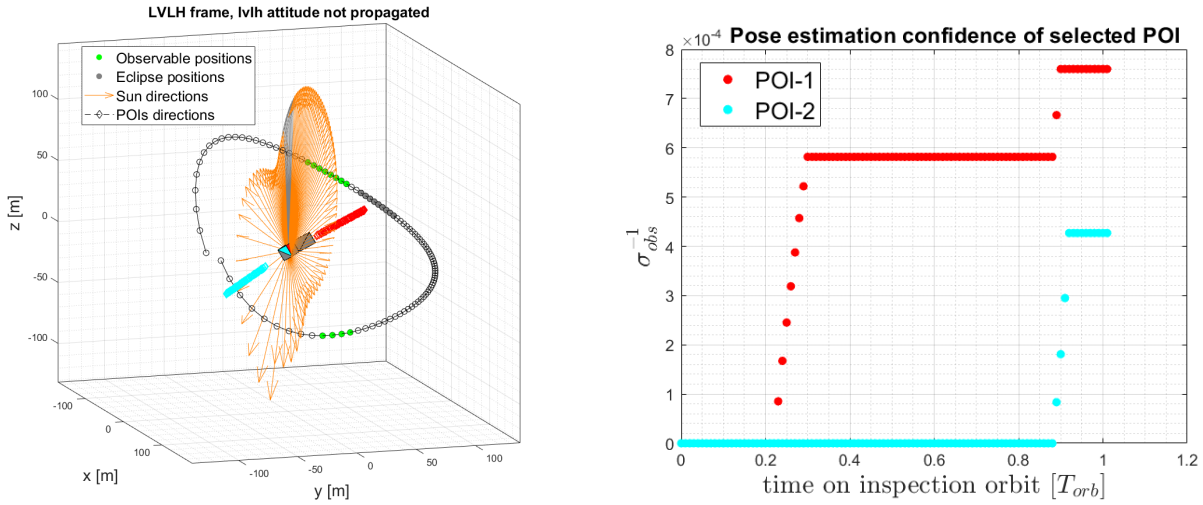

Figure 3.3.13: Inspection results on fixed target spacecraft (not in scale)

the planner still finds two observation windows to inspect the POI; in this case, given the initial attitude of the target, the red POI is visible under better conditions, whereas the blue one is seen under high observation angles, which imply high observation variance. A rotating target can favour observation of many points on its geometry that would be otherwise hidden but, as introduced, the efficacy of the planner (the actual observation quality against the predicted one) is naturally affected by uncertainties in the rotational motion of the spacecraft. A test is presented in the following to assess how uncertainties in the estimation of initial data for attitude propagation from Tab.3.3.5 affect the planning algorithm; in particular, the observation results for three selected POI are compared to the same planning algorithm which does not propagate the target attitude. Tab.3.3.6 reports the estimation uncertainties considered on the initial conditions for the target rotational motion; these are used to change the initial conditions specified in Tab.3.3.5 for the actual rotational motion, whereas the ideal

conditions are fed to the planning algorithm with and without attitude propagation.

Table 3.3.6: Uncertainties for target attitude propagation

$\sigma_{\omega,0}$ [deg/s]	$\sigma_{q,0}$ [deg]	σ_J $[kg \cdot m^2]$
0.1	2	10

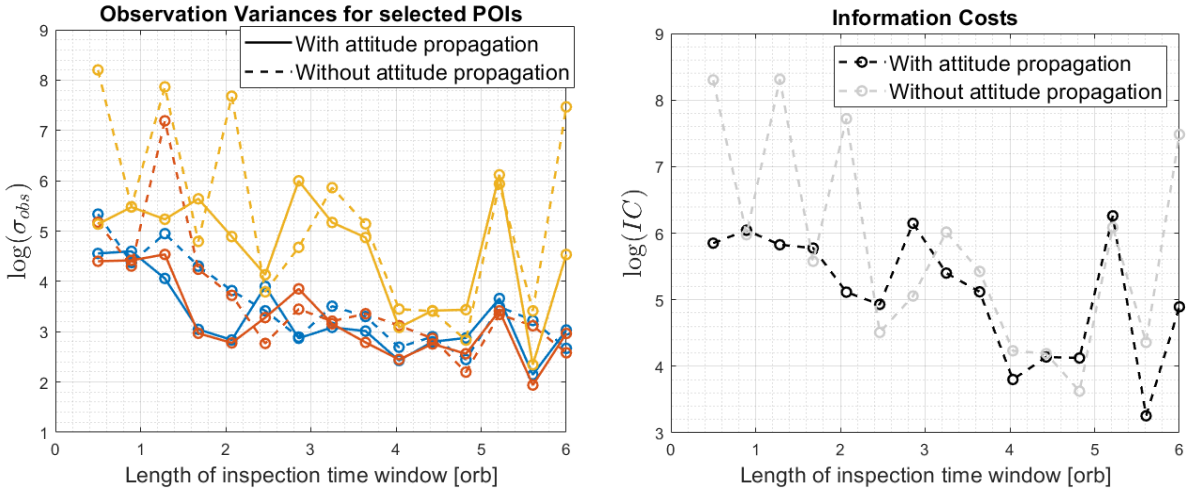

Figure 3.3.14: Results over increasing windows with and without attitude propagation

Fig.3.3.14 reports the single observation variances for the three POI as well as the total information cost for each test case. Looking at the figure on the right, it is clear that, for the given uncertainties, the planning algorithm which includes attitude propagation consistently provides the better observation trajectory for a limited time window (for about less than 2.5 periods). Due to the numerical integration of Eqs.3.65, a faster rotating target would reduce this time horizon even further, leading to the conclusion that attitude propagation can be useful for low initial angular velocities $\boldsymbol{\omega}$ of the space debris and for time-limited inspection orbits; as it will be seen in the next section, this implies using safe intermediate parking orbits to move from one inspection orbit to the next.

Chapter 4

Integration in the RPO Simulator

4.1 Simulator Description

As previously introduced, the final step of the work is the integration of the developed guidance algorithms in the Rendezvous and Proximity Operations (RPO) simulator, a high fidelity `MATLAB/Simulink` simulation tool developed in the department to test GNC software. At the highest level, the simulator is split into a ”Real World” subsystem and a ”Software” one. The first of the two is reported is Fig.4.1.1, and its purpose is

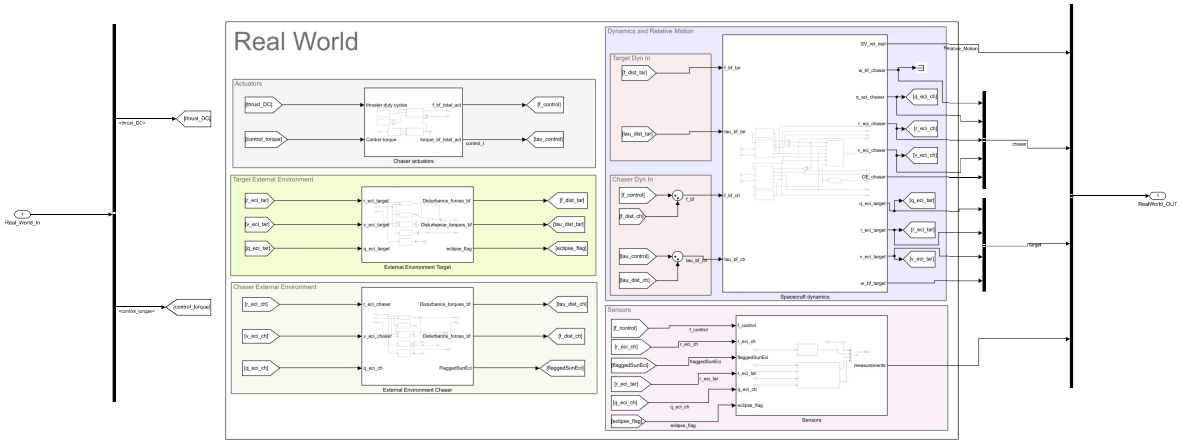

Figure 4.1.1: Real world subsystem of RPO simulator

to accurately simulate the relative spacecraft dynamics to be controlled. In particular, orbital motion of the chaser and target is obtained through integration of the non-linear equations of motion considering a complex gravitational model which accounts for the Earth mass distribution, as well as orbit perturbations including a differential drag

model based on the actual geometry of the two satellites. For the controlled chaser, two types of actuators are implemented: a set of six ON/OFF thrusters are used to execute the orbital manoeuvres commanded by the guidance, whereas three reaction wheels are used to provide attitude control. For the current application, the only sensor which is implemented is a visual-based, wide-angle camera used to point to the target in proximity operations.

The ”Software” part of the simulator includes attitude control to align the chaser axes to the LVLH frame or to point to the target and a relative motion guidance block which includes the algorithms developed in Sec.3; its input and output interfaces are shown in Fig.4.1.2. Some observations are at order:

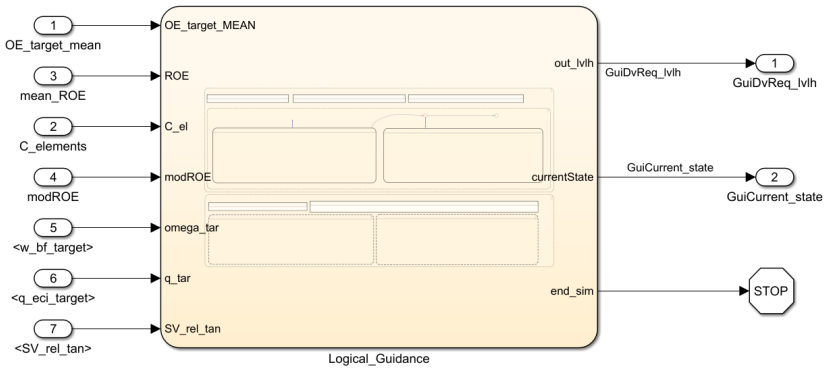

Figure 4.1.2: Guidance subsystem of RPO simulator

- As seen in previous sections, the main data used by the developed guidance are absolute and relative orbit elements; the first are retrieved using classic conversion routines from the Cartesian representation used in the integration of the equations of motion within the spacecraft plant. However, to exclude short-term oscillations caused by environment perturbations, these osculating sets are converted to mean sets through the first-order mapping based on the Brouwer and Lyddane theory provided in Appendix F of [60]. Accordingly, the ROE sets are computed using the single absolute mean sets.
- In a realistic scenario, all the shown inputs are estimated by the navigation software, which naturally introduces errors on the real data based on the system performance. Since the focus of the current work lies on the guidance, these inputs are taken as the real data from integration.
- The main output of the guidance block is a $\Delta\mathbf{v}$ request, which is sent as a pulse

signal at the time of execution. A thruster firing algorithm picks up the request and computes the duty cycles to send to the ON/OFF thrusters according to a Pulse-Width Modulation (PWM) logic; the idea is to compute the cumulative velocity change supplied based on the integration of the force delivered by the thrusters. Note that this functioning implies finite-duration burns during the manoeuvres, which already introduces a relevant discrepancy from the impulsive changes of velocity assumed so far.

One last observation is reserved to the linear propagation models used by the guidance; as previously discussed, the strategies detailed in Sec.3.3 make use of STM models to propagate the relative motion accounting for orbit perturbations. As reported in Appendix B, the inclusion of differential drag effects requires an estimation of the assumed piecewise-constant change rates of δa, δe_x^* and δe_y^*; in a conservative framework, this can be done on-the-fly by reaching a safe relative orbit and acquiring a set of data over which the estimation may be performed. Fig.4.1.3 reports the guidance

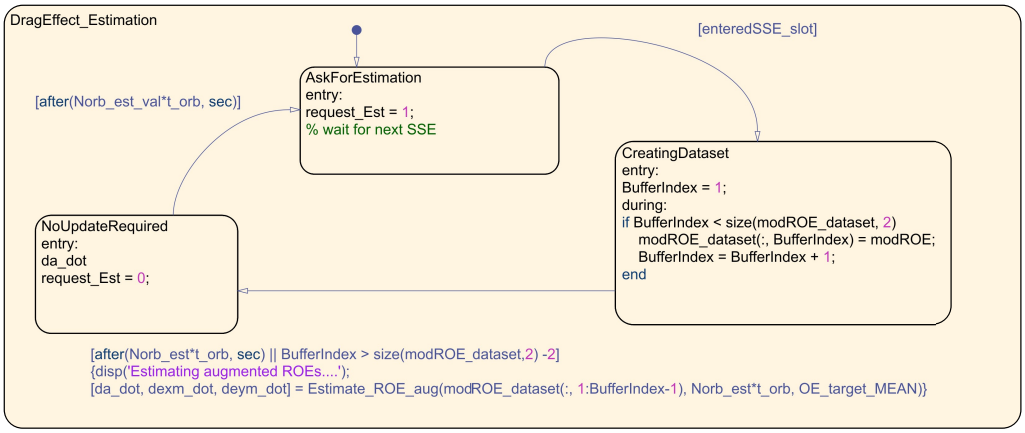

Figure 4.1.3: Drag effect estimation superstate

state which controls the estimation process. In particular, if the past estimation of the time derivatives needs to be updated or no prior estimation is available the superstate raises a request (managed by the upper layer of Fig.3.3.2) to reach a Stationary Safe Ellipse (SSE); once the lower control layers confirm its achievement, the dataset for estimation is created in a predefined time period where manoeuvres are not allowed. To take advantage of the geometry defined for the approach (see Fig.3.3.1), the waypoints can be used as locations to periodically update the dataset.

4.2 Missions Definition

The current section details two rendezvous scenarios, one with a circular target orbit and the other with an elliptic one, in which the integrated guidance software is tested, as well as common data between the two cases.

4.2.1 General Simulations Setup

The chaser spacecraft geometry considered for both missions is visualised in Fig.4.2.1; the visual based camera is assumed to be mounted on the $+z$ direction, therefore its z-axis is oriented towards the target using a simple PD control algorithm and the onboard reaction wheels. The presented mission scenarios can share the same rendezvous

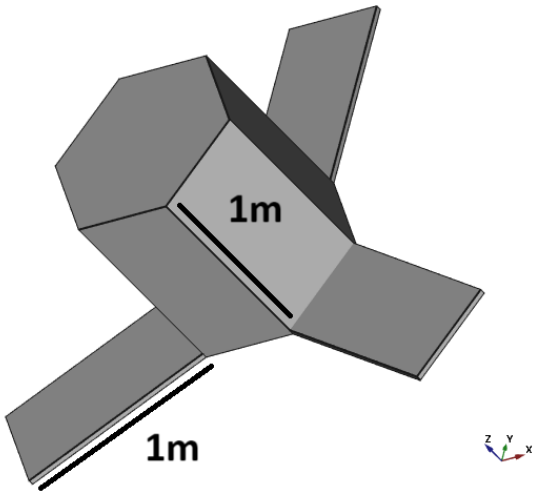

Figure 4.2.1: Chaser spacecraft geometry

Table 4.2.1: Common simulation data, first part

Parameter	Symbol	Value	Unit
Chaser mass	m_c	400	kg
Thruster force	F_c	20	N
Minimum Δv deliverable	Δv_{min}	0.2	mm/s
# of orbits for drag effects estimation	N_{orb}^{est}	3	orbits
Validity of drag effects estimation	N_{orb}^{val}	30	orbits
Maximum range for inspection	d_{max}	100	m
Maximum observation angle	α_{obs}^{max}	80	^{o}
Maximum illumination angle	α_{ill}^{max}	85	^{o}
Prior variance of POI	σ_0	10^8	[-]

concept of operations, which is visualised in the following figure.

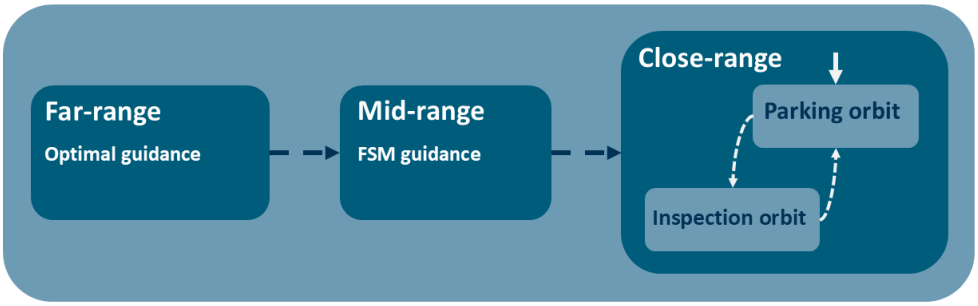

Figure 4.2.2: Rendezvous concept of operations

Table 4.2.2: Common simulation data, second part

Parameter	Symbol	Value	Unit
FSM relative E/I separation threshold	EI_{thr}	5	deg
FSM SSE relative drift threshold	$a\delta a_{thr}$	1	m
FSM WSE maximum relative drift	$a\delta a_{max}$	100	m
FSM WSE minimum relative drift	$a\delta a_{min}$	3	m
FSM WSE nominal drift period between waypoints	T_{drift}	5	orbits
Inspection margins from KOZ along z and y	M_{zy}^{insp}	[5, 5]	m
Inspection maximum absolute drift	$a\delta a_{max}^{insp}$	5	m
Inspection maximum IP/OOP sizes	-	100	m
Inspection orbit along track position	C_4^{insp}	0	m
Inspection planning initial sample	N_{sample}^{init}	300	[-]
Inspection planning # mesh refinement	n_{meshes}	2	[-]
Inspection planning volume weight for refinement	η_V	1	[-]
Inspection planning cost weight for refinement	η_C	300	[-]
Inspection planning gradient weight for refinement	η_G	150	[-]
Inspection planning # of added points per refinement	n_{refine}	100	[-]
Inspection planning # of trajectory discretised points	N_{insp}	100	[-]
Duration of transfer from parking orbit to inspection	T_{transf}	0.8	orbits
Duration of inspection	T_{insp}	2	orbits
Number of firings to use to reach inspection orbit	$N_{firings}$	6	[-]
Holding period over parking orbit	T_{park}	2	orbits
Parking orbit position on the along-track axis	$\lvert a\delta\lambda_{park}\rvert$	250	m
Parking orbit margins from KOZ	M_{zy}^{insp}	[80, 80]	m
Optimal guidance maximum reconfiguration time	$T_{reconfig}^{max}$	1.5	orbits

The idea is to cover large initial reconfigurations using the open-loop planning of the optimal guidance and then switch over to the FSM to safely approach the target and

accommodate holding positions. Finally, proximity operations begin by safely entering a parking orbit using a generalised radial hop, from which the inspection orbit can be reached using a time-fixed glideslope manoeuvre.

4.2.2 First Scenario: Inspection of Rocket Body in SSO

The first test scenario is based on the Phase I of the Commercial Removal of Debris Demonstration (CRD2) project, within which the satellite ADRAS-J, developed by Astroscale Japan, performed rendezvous and inspection of a non-cooperative object on a Sun-Synchronous Orbit (SSO) [71]; the designated target was the H-IIA upper stage, used in 2009 to launch the Greenhouse Gases Observing Satellite (GOSAT). Based on the rocket body NORAD ID (33500), its Keplerian elements have been retrieved from [61] and are reported in Tab.4.2.3. Tab.4.2.4 reports the input data for the far-

Table 4.2.3: Keplerian elements and assumed inertia of the H-IIA upper stage

a [km]	e [-]	i [^{o}]	Ω [^{o}]	ω [^{o}]	m_T [kg]	$[J_{xx}, J_{yy}, J_{zz}]$ $[kg \cdot m^2]$
7167.5	0.0036	98.25	211.94	139.43	2000	[7647, 1210, 7647]

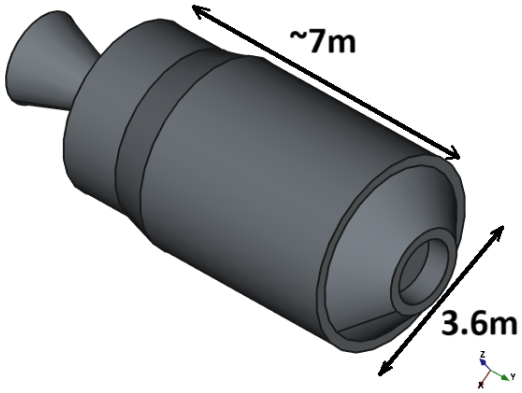

Figure 4.2.3: Rocket body geometry

Table 4.2.4: Optimal guidance far-range data, scenario 1

$a\delta\boldsymbol{\alpha}$ [km]	$\Delta T_{no\ man.}$ [orbits]	T_{final} [orbits]	k_ω
$a\delta\boldsymbol{\alpha}_0 = [0.01, -40, 0, 1.0, 0.5, -0.6]^T$ $a\delta\boldsymbol{\alpha}_F = [0.00, -15, 0, 0.5, 0, -0.5]^T$	[5.5, 6; 8, 9.5; 13, 15; 19, 22]	25	0.069

Table 4.2.5: FSM mid-range data, scenario 1

Along-track positions [km]	Hold times [orbits]	Margins from KOZ [m]
$[-15, -3, -0.5]$	$[2, 3, 2]$	$\begin{bmatrix} M_z \\ M_y \end{bmatrix} = \begin{bmatrix} 250 & 150 & 100 \\ 250 & 150 & 100 \end{bmatrix}$

range guidance; initial and aimed relative states are given in the form of quasi-non-singular ROE, and a series of time constraints, defined from the moment of generation of the guidance plan, is also provided. As previously introduced, the flexibility offered from the discretised time nodes allows to embed higher level requirements like periods where no manoeuvres are allowed ($\Delta T_{no\ man.}$) as well as a tentative final time (T_{final}). The FSM, mid-range guidance is constrained by the waypoint data given in Tab.4.2.5. Lastly, the inspection planning algorithm parameters are fully defined by Tab.4.2.2 except for the POI, which is selected to optimise visibility on a specific surface on the cylindrical outer hull, as it will be seen later.

4.2.3 Second Scenario: Rendezvous with HEO Satellite

The second scenario is defined to prove safe rendezvous capability to a Highly-Eccentric Orbit spacecraft; the target specifications are reported in Tab.4.2.6 and its geometry in Fig.4.2.4. Tab.4.2.7 reports the input data to the far-range guidance. On

Table 4.2.6: Keplerian elements and assumed inertia of the target

a [km]	e [-]	i [^{o}]	Ω [^{o}]	ω [^{o}]	m_T [kg]	$[J_{xx}, J_{yy}, J_{zz}]$ $[kg \cdot m^2]$
14156	0.5	59	84	188	400	[200, 400, 400]

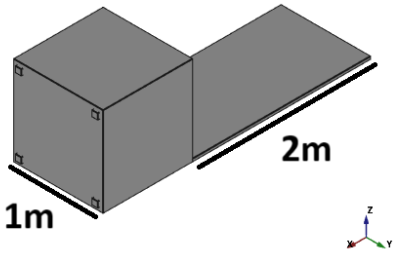

Figure 4.2.4: Target satellite geometry

the other hand, for the mid-range FSM the same parameters as those specified for the

Table 4.2.7: Optimal guidance far-range data, scenario 2

C-elements [km]	$\Delta T_{no\ man.}$ [orbits]	T_{final} [orbits]	k_ω
$\boldsymbol{C}_0 = [0.005, 0, 1.0, -40, 0.5, -0.6]^T$ $\boldsymbol{C}_F = [0.000, 0, 0.5, -20, 0.0, -0.5]^T$	[0, 0.5; 2, 3; 5, 6]	10	0.4

circular target scenario are used (see Tab.4.2.5) to showcase how the same architecture can be used across different orbit scenarios.

4.3 Results

4.3.1 First Scenario

The resulting trajectory for the entire approach to the target is shown in Fig.4.3.1; on the right side, the cross-track plane projection is displayed to demonstrate PAS of the entire approach. The entire timeline of the Δv requests over the approach is shown in

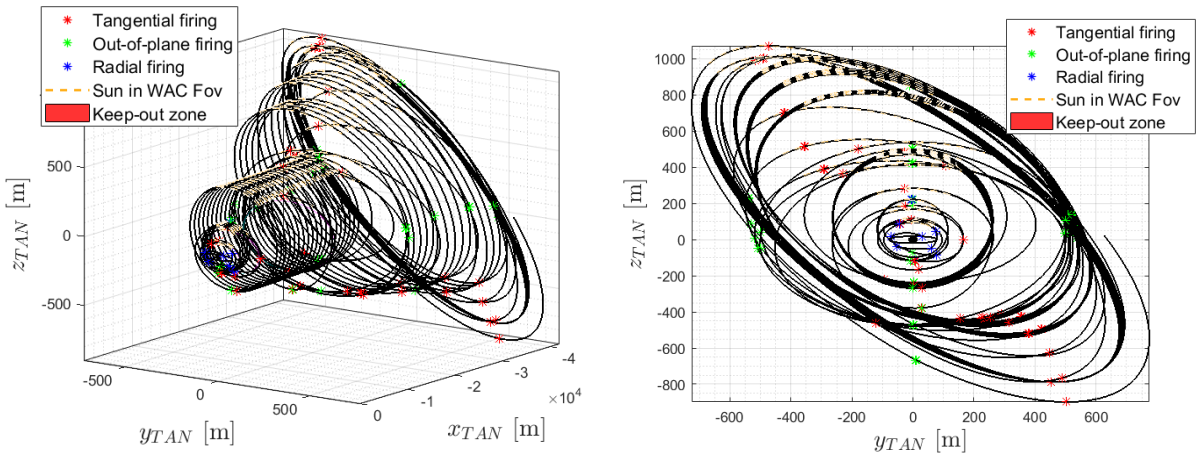

Figure 4.3.1: Relative trajectory in TAN frame, Scenario 1

Fig.4.3.2 and allows to make some observations:

- For the practical implementation, single point manoeuvres (radial and out-of-plane) are decomposed in multiple firings when the single Δv request is too high; for the current tests, the limit has been set to 5 cm/s. For the defined chaser spacecraft mass and thrust specifications (see Tab.4.2.1), these single firings only take few seconds to be completed.
- The very first task scheduled by the integrated guidance is a three-point tangential manoeuvre (and OOP correction) to enter a SSE state on the current

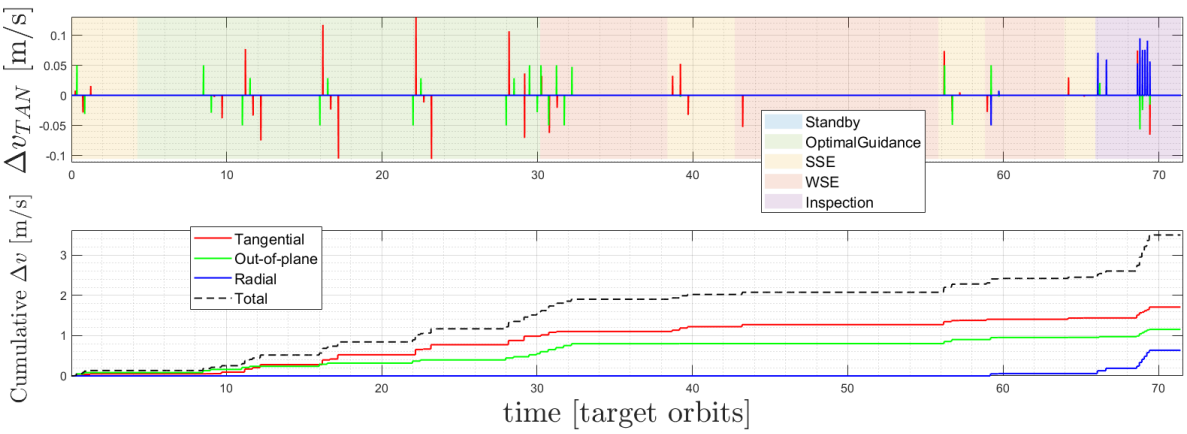

Figure 4.3.2: Δv commands requested by the guidance, Scenario 1

position; the reason for this is to create a first estimation on the differential drag effects.

- From the moment of generation of the open-loop optimal guidance plan one can notice that no manoeuvres take place in the forbidden time periods specified by $\Delta T_{no\ man.}$ (see Tab.4.2.4).
- According to the FSM definition, very few manoeuvres are executed within the WSE drifting periods; moreover, as described in Sec.3.3.1, the guidance has the authority to change the length of the nominal drifting period to be compliant with the specified safety constraints. It can also be observed that the first SSE of the FSM hold time is longer than the one specified in Tab.4.2.5. The reason for this is because the on-board guidance (more specifically the superstate in Fig.4.1.3) demands an update of the drag effects estimation, according to the data specified in Tab.4.2.1, and therefore maintains the holding position for longer.
- The inspection phase begins with the two-point non-drifting transfer to reach the parking orbit; from there, the safe ROE glideslope is used to enter the inspection trajectory.
- Looking at the cumulative Δv request over time in the lower plot of Fig.4.3.2 one can notice that significant amounts of fuel are consumed during the execution of the optimal plan and the final ROE glideslope. As for the first reconfiguration, the consumption is related to how many intermediate configurations are commanded; by using a lower number of time nodes the chaser can reach the aimed state in less manoeuvres, improving fuel efficiency. For the second reconfiguration, this level of fuel consumption is related to the choice made

to have drift-free intermediate configurations in the glideslope trajectory, as explained in Sec.3.2.3.

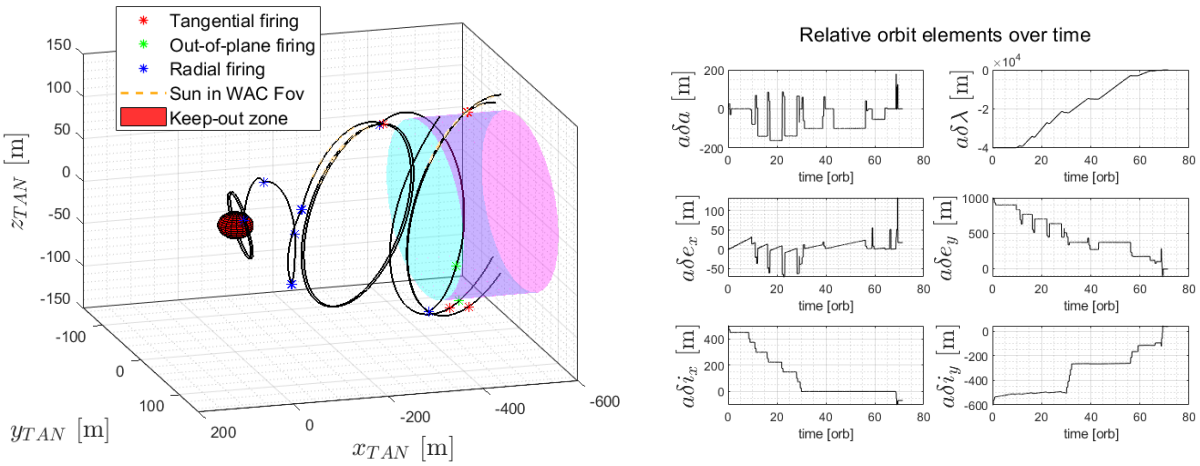

Figure 4.3.3: Close-proximity trajectory (left) and ROE history (right)

Fig.4.3.3 reports the zoom-in on the close-proximity trajectory as well as the history of the ROE over time. From the figure on the left, one can distinguish the non-drifting transfer used to reach the stationary parking orbit from the last specified waypoint, as well as the glideslope trajectory (whose firings are mostly aligned with the radial direction) which spirals around the x-axis to reach the inspection orbit. The right side of Fig.4.3.3 reveals that the intermediate positions of the final manoeuvre are characterised by high values of the relative drift as well as of the relative eccentricity vector. As previously introduced, the inspection planning algorithm is used to optimise

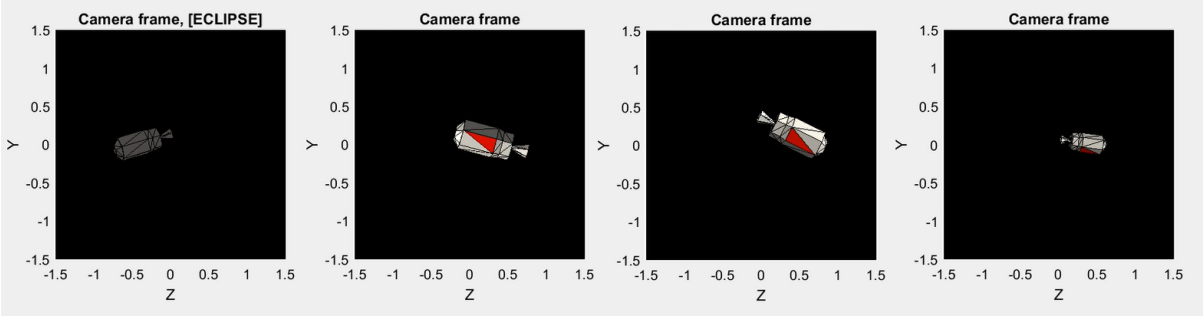

Figure 4.3.4: Chaser camera frames during inspection, Scenario 1

the observation over a specific point on the cylindrical outer hull of the rocket; Fig.4.3.4 reports the view from the chaser camera over four positions on the reached inspection orbit, assuming that the Sun lies on the orbit plane of the target (dawn-dusk orbit). The POI, coloured in red, can be observed under proper lighting conditions during the closest passage to the target.

4.3.2 Second Scenario

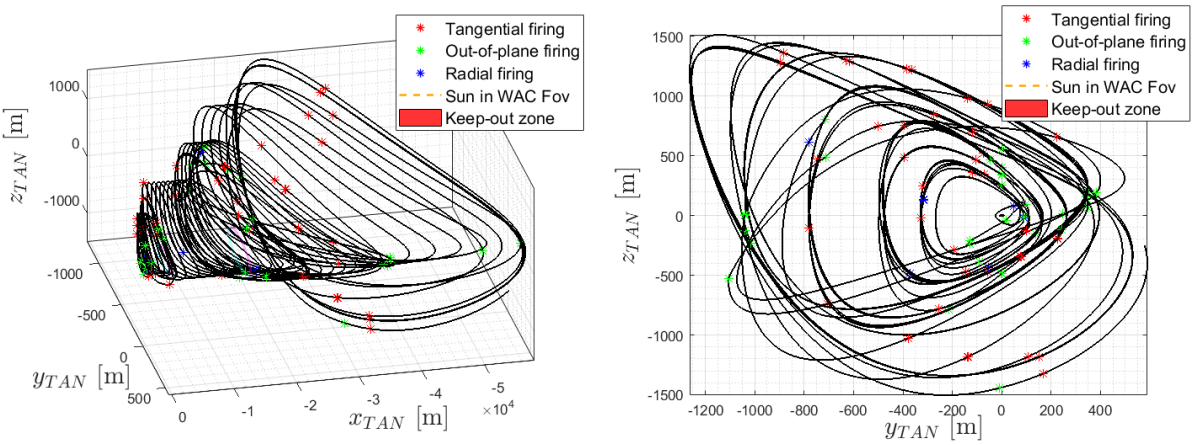

Figure 4.3.5: Relative trajectory in TAN frame, Scenario 2

Fig.4.3.5 reports the relative TAN trajectory of the chaser spacecraft. When comparing the overall trajectory to Fig.4.3.1, it is apparent how the higher orbit eccentricity increases the maximum cross-track oscillations when imposing the same PAS margins. This effect is particularly relevant when considering relative navigation methods based on target detection and a fixed-attitude chaser, where line-of-sight angle requirements become critical. The timeline of the guidance Δv commands is reported in Fig.4.3.6;

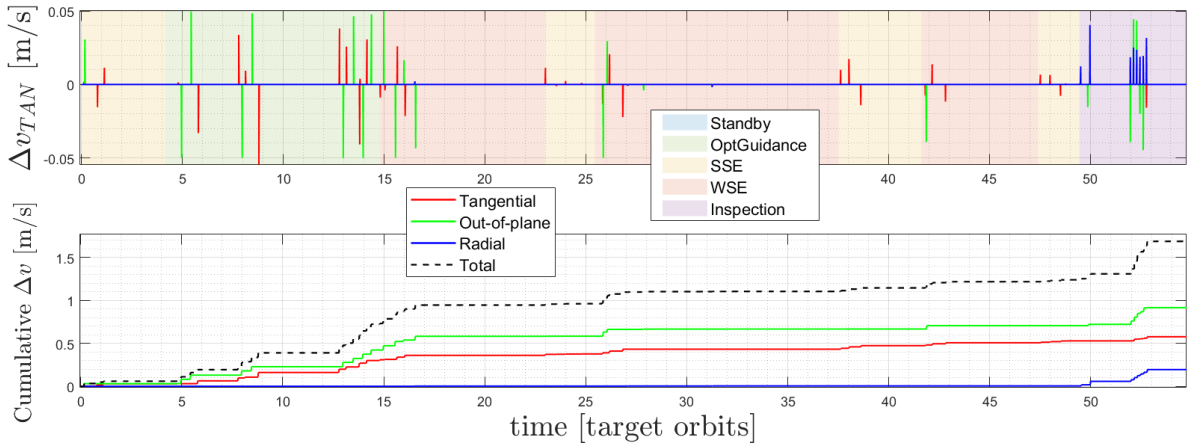

Figure 4.3.6: Δv commands requested by the guidance, Scenario 2

the main difference from the previous case is the shorter optimal guidance plan, which now only spans ten orbit periods. This is naturally reflected in faster drifting orbits during the initial large reconfigurations, as seen in Fig.4.3.5; the shorter time horizon for the optimal reconfiguration also causes the update in the drag estimation effects to move from the first SSE of the FSM to the second.

As it can be seen on the right side of Fig.4.3.7, this mission scenario is characterised by

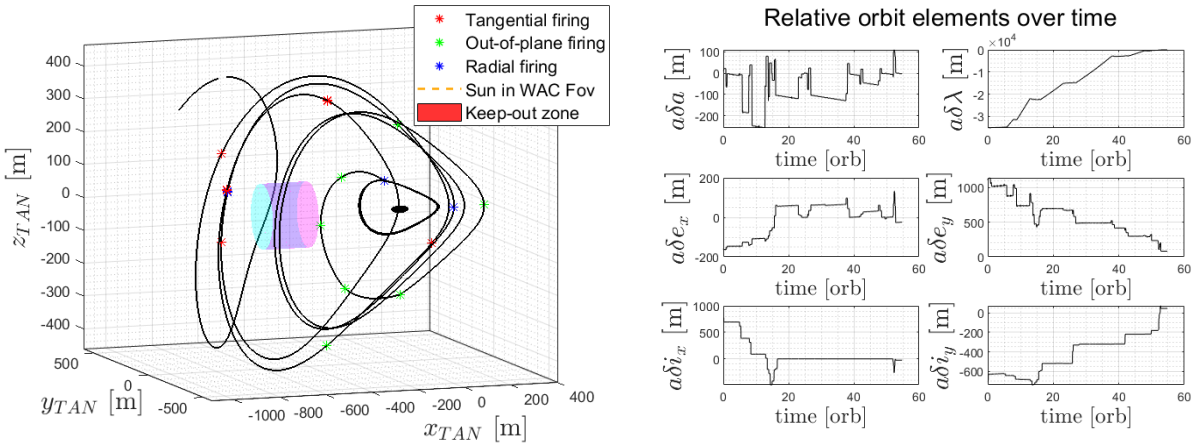

Figure 4.3.7: Close-proximity trajectory (left) and ROE history (right), Scenario 2

higher differential drag effects on the relative semi-major axis, which are compensated by the FSM using more frequent tangential correcting firings during holding phases. It should be pointed out that, given the sign of the time derivative of $\delta\dot{a}$, in a practical scenario the ideal way to reach the target would have been to approach it from the front ($+x$-direction) rather than from the back; this would increase the passive safety because in case of loss of thrust control the differential drag would naturally separate the two spacecraft rather than closing their distance. On the left side of Fig.4.3.7, the close-proximity trajectory is also shown to be characterised by larger IP and OOP oscillations, as well as relative orbits which compared to Fig.4.3.3 have a more pronounced excursion in the along-track direction. This effect is intuitively accentuated for higher eccentricities of the target orbit [50], and should be taken into account when extending the use of the presented rendezvous approach to general cases.

Chapter 5

Conclusions and Future Work

The presented work has demonstrated how to develop an integrated autonomous guidance software for rendezvous and inspection operations starting from the lower layer architecture which makes use of closed-form manoeuvres. As shown in Sec.4, the proposed logic can be easily reused in different mission scenarios with only few changes; such a result has been achieved thanks to different choices made throughout the work to generalise the formulation.

In particular, in Sec.2.1.5 the advantages in the adoption of ROE to parametrize the relative motion have been discussed; it was also shown that the geometrical intuition on the shape of the relative orbit given by quasi-non-singular ROE may be extended to elliptic target orbits by considering new sets of integration constants. To this regard, C-elements have been taken into account to generalise the concept of relative E/I separation to grant Passive-Abort Safety in spiralling rendezvous approaches.

In Sec.3.2 a guidance library of single-point and multiple-point manoeuvres has been developed moving from the Gauss Variational Equations expressed in a velocity-aligned frame. This choice allowed to more easily generalise closed-form solutions of schemes developed in near-circular target cases to eccentric scenarios.

As for the higher layers of the software, an original architecture in the form of a Finite State Machine has been developed and proposed to enable autonomous rendezvous operations. Its flexibility to adapt to substantially different mission scenarios while still maintaining the same level of passive safety has been demonstrated during the validation in the high-fidelity simulator in Sec.4; nonetheless, it should be reminded that some level of tuning of its parameters (see Tab.4.2.2) is still required based

on the mission specifications and expected control/navigation performance. One possible way of improvement would be to let the guidance autonomously decide control thresholds based on the estimated orbit perturbations and geometric margins using linear propagation of the estimated relative state covariance. Lastly, the fundamental structure of the FSM has been developed with modularity in mind, meaning that the software itself allows for easy and quick updates, for example substitution of a newly implemented manoeuvring scheme in place of one of the blocks in Fig.3.3.3.

Autonomous guidance strategies from the literature have also been explored and extended to arbitrarily eccentric cases using the C-elements set. In particular, in Sec.3.3.2 a penalty function has been introduced to deviate the minimum path of the optimal guidance towards safer intermediate positions. With respect to its integration in the non-linear simulator, one natural way of improvement of the final state achieved would be to implement the optimal plan generation using the logic of Model Predictive Control, which entails a re-computation of the remaining plan after each manoeuvre is executed.

Lastly, a sampling-based inspection algorithm has been developed to orient safe close proximity operations towards the optimal observation of selected Points Of Interest on the target geometry. A level of optimisation in the search of the inspection trajectory has been introduced using a mesh-refining method to improve the predicted inspection results using smaller samples of points and the benefit of including an on-board model which propagates the target attitude has been assessed through specific tests based on the uncertainty characterising the initial conditions. Future work could involve researching methods aimed to reduce the uncertainties related to relative attitude propagation such that the single inspection may last longer and the overall fuel consumption be reduced. Moreover, a different definition of the visibility database and information cost, which conditions the smoothness of the search domain, could be proposed to allow the implementation of efficient gradient descent algorithms to obtain better observation trajectories in a reduced time.

Bibliography

[1] Alfriend, Kyle, Vadali, Srinivas Rao, Gurfil, Pini, How, Jonathan, and Breger, Louis. *Spacecraft formation flying: Dynamics, control and navigation*. Vol. 2. Elsevier, 2009.

[2] Battin, Richard H. *An introduction to the mathematics and methods of astrodynamics*. Aiaa, 1999.

[3] Borelli, Giacomo. "Strategies for safe operations of removal and servicing missions in low Earth orbit". In: (2023).

[4] Borelli, Giacomo, Gaias, Gabriella, and Colombo, Camilla. "Rendezvous and proximity operations design of an active debris removal service to a large constellation fleet". In: *Acta Astronautica* 205 (2023), pp. 33–46.

[5] Borelli, Giacomo, Gaias, Gabriella, Nakajima, Yu, Colombo, Camilla, Capuano, Vincenzo, Saggiomo, Fabio, Leccese, Giuseppe, and Natalucci, Silvia. "Mission analysis and guidance and control for the SpEye inspection CubeSat". In: *Acta Astronautica* 220 (2024), pp. 75–87.

[6] Brouwer, Dirk and Clemence, Gerald M. *Methods of celestial mechanics*. Elsevier, 2013.

[7] Bryson, Arthur Earl. *Applied optimal control: optimization, estimation and control*. Routledge, 2018.

[8] Capolupo, Francesco and Labourdette, Pierre. "Receding-horizon trajectory planning algorithm for passively safe on-orbit inspection missions". In: *Journal of Guidance, Control, and Dynamics* 42.5 (2019), pp. 1023–1032.

[9] Chamberlin, James A and Rose, James T. "Gemini rendezvous program". In: *Journal of Spacecraft and Rockets* 1.1 (1964), pp. 13–18.

[10] Chernick, Michelle and D'Amico, Simone. "New closed-form solutions for optimal impulsive control of spacecraft relative motion". In: *Journal of Guidance, Control, and Dynamics* 41.2 (2018), pp. 301–319.

[11] Clohessy, WH and Wiltshire, RS. "Terminal guidance system for satellite rendezvous". In: *Journal of the aerospace sciences* 27.9 (1960), pp. 653–658.

[12] Curtis, Howard D. *Orbital mechanics for engineering students*. Butterworth-Heinemann, 2019.

[13] D'Amico, Simone. "Autonomous formation flying in low earth orbit". In: (2010).

[14] D'Amico, Simone, Ardaens, J-S, and Larsson, Robin. "Spaceborne autonomous formation-flying experiment on the PRISMA mission". In: *Journal of Guidance, Control, and Dynamics* 35.3 (2012), pp. 834–850.

[15] D'Amico, Simone and Montenbruck, Oliver. "Proximity operations of formation-flying spacecraft using an eccentricity/inclination vector separation". In: *Journal of Guidance, Control, and Dynamics* 29.3 (2006), pp. 554–563.

[16] D'Amico, Simone. "Relative orbital elements as integration constants of Hill's equations". In: *DLR, TN* (2005), pp. 05–08.

[17] Davis, Thomas, Baker, Major Tammy, Belchak, Timothy, and Larsen, William. "XSS-10 micro-satellite flight demonstration program". In: (2003).

[18] Di Mauro, Giuseppe, Lawn, Margaret, and Bevilacqua, Riccardo. "Survey on guidance navigation and control requirements for spacecraft formation-flying missions". In: *Journal of Guidance, Control, and Dynamics* 41.3 (2018), pp. 581–602.

[19] Eckstein, MC, Rajasingh, CK, and Blumer, P. "Colocation strategy and collision avoidance for the geostationary satellites at 19 degrees west". In: *International Symposium on Space Flight Dynamics*. Vol. 6. 1989, p. 28.

[20] Ekal, Monica, Albee, Keenan, Coltin, Brian, Ventura, Rodrigo, Linares, Richard, and Miller, David W. "Online information-aware motion planning with inertial parameter learning for robotic free-flyers". In: *2021 IEEE/RSJ International Conference on Intelligent Robots and Systems (IROS)*. IEEE. 2021, pp. 8766–8773.

[21] ensatellite. *Hill's Equations: Derivation and Solution*. https://ensatellite.com/hills-equations/. 2025.

[22] ESA. "Reference Systems and Frames". In: (2011). URL: https://gssc.esa.int/navipedia/index.php/Reference_Systems_and_Frames#cite_note-1.

[23] Fehse, Wigbert. *Automated rendezvous and docking of spacecraft*. Vol. 16. Cambridge university press, 2003.

[24] Forshaw, Jason, Lopez, Ron, Okamoto, Akira, Blackerby, Chris, and Okada, Nobu. "The ELSA-d End-of-life debris removal mission: mission design, in-flight safety, and preparations for launch". In: *Proceedings of the Advanced Maui Optical and Space Surveillance Technologies Conference*. 2019, pp. 17–20.

[25] Fortescue, Peter, Swinerd, Graham, and Stark, John. *Spacecraft systems engineering*. John Wiley & Sons, 2011.

[26] Gaias, Gabriella, Ardaens, Jean-Sébastien, and Montenbruck, Oliver. "Model of J 2 perturbed satellite relative motion with time-varying differential drag". In: *Celestial Mechanics and Dynamical Astronomy* 123.4 (2015), pp. 411–433.

[27] Gaias, Gabriella, Ardaens, Jean-Sébastien, and Schultz, Christian. "The AVANTI experiment: flight results". In: (2017).

[28] Gaias, Gabriella, Colombo, Camilla, and Lara, Martin. "Analytical framework for precise relative motion in low earth orbits". In: *Journal of Guidance, Control, and Dynamics* 43.5 (2020), pp. 915–927.

[29] Gaias, Gabriella, D'Amico, Simone, and Ardaens, Jean-Sébastien. "Generalised multi-impulsive manoeuvres for optimum spacecraft rendezvous in near-circular orbit". In: *International Journal of Space Science and Engineering* 3.1 (2015), pp. 68–88.

[30] Gaias, Gabriella and D'Amico, Simone. "Impulsive maneuvers for formation reconfiguration using relative orbital elements". In: *Journal of Guidance, Control, and Dynamics* 38.6 (2015), pp. 1036–1049.

[31] Gim, Dong-Woo and Alfriend, Kyle T. "State transition matrix of relative motion for the perturbed noncircular reference orbit". In: *Journal of guidance, control, and dynamics* 26.6 (2003), pp. 956–971.

[32] Goodman, John L. “History of space shuttle rendezvous and proximity operations”. In: *Journal of Spacecraft and Rockets* 43.5 (2006), pp. 944–959.

[33] Grimme, Christian. “Picking a uniformly random point from an arbitrary simplex”. In: *Inf. Syst. Statist., Munster, Germany, Tech. Rep* (2015).

[34] Hablani, Hari B, Tapper, Myron L, and Dana-Bashian, David J. “Guidance and relative navigation for autonomous rendezvous in a circular orbit”. In: *Journal of guidance, control, and dynamics* 25.3 (2002), pp. 553–562.

[35] Hanspeter Schaub. *Attitude Dynamics Fundamentals*. `https://hanspeterschaub.info/PapersPrivate/Schaub2010c.pdf`. 2010.

[36] Harris, Andrew, Teil, Thibaud, and Schaub, Hanspeter. “Spacecraft decision-making autonomy using deep reinforcement learning”. In: *29th AAS/AIAA space flight mechanics meeting, hawaii*. 2019, pp. 1–19.

[37] Jiang, Fanghua, Li, Junfeng, Baoyin, Hexi, and Gao, Yunfeng. “Study on relative orbit geometry of spacecraft formations in elliptical reference orbits”. In: *Journal of guidance, control, and dynamics* 31.1 (2008), pp. 123–134.

[38] Kawano, Isao, Mokuno, Masaaki, Kasai, Toru, and Suzuki, Takashi. “Result and evaluation of autonomous rendezvous docking experiment of ETS-VII”. In: *Guidance, Navigation, and Control Conference and Exhibit*. 1999, p. 4073.

[39] Koenig, Adam W, Guffanti, Tommaso, and D’Amico, Simone. “New state transition matrices for spacecraft relative motion in perturbed orbits”. In: *Journal of Guidance, Control, and Dynamics* 40.7 (2017), pp. 1749–1768.

[40] Komendera, Erik, Scheeres, Daniel, and Bradley, Elizabeth. “Intelligent computation of reachability sets for space missions”. In: *Proceedings of the AAAI Conference on Artificial Intelligence*. Vol. 26. 2. 2012, pp. 2299–2304.

[41] Lim, Yeerang and Mok, Sung-Hoon. “In-plane formation reconfiguration with radial maneuvers”. In: *Journal of Guidance, Control, and Dynamics* 43.10 (2020), pp. 1881–1892.

[42] Markley, F Landis and Crassidis, John L. “Correction to: Fundamentals of Spacecraft Attitude Determination and Control”. In: *Fundamentals of spacecraft attitude determination and control*. Springer, 2014, pp. C1–C7.

[43] Montenbruck, O, Kirschner, M, and D’Amico, Simone. “E-/I-vector separation for GRACE proximity operations”. In: *DLR/GSOC TN* (2004), pp. 04–08.

[44] Nakka, Yashwanth Kumar, Hönig, Wolfgang, Choi, Changrak, Harvard, Alexei, Rahmani, Amir, and Chung, Soon-Jo. “Information-based guidance and control architecture for multi-spacecraft on-orbit inspection”. In: *Journal of Guidance, Control, and Dynamics* 45.7 (2022), pp. 1184–1201.

[45] Office, ESA Space Debris. “ESA’S ANNUAL SPACE ENVIRONMENT REPORT”. In: (31 March 2025).

[46] Pearson, Don J. “The glideslope approach”. In: *Orbital mechanics and mission design* (1989), pp. 109–123.

[47] Pesce, Vincenzo, Colagrossi, Andrea, and Silvestrini, Stefano. *Modern spacecraft guidance, navigation, and control: from system modeling to AI and innovative applications*. Elsevier, 2022.

[48] Peters, Thomas V. “Formation flying guidance for space debris observation, manipulation and capture”. In: *Astrodynamics Network AstroNet-II: The Final Conference*. Springer. 2016, pp. 225–239.

[49] Peters, Thomas V, Branco, João, Escorial, Diego, Castellani, Lorenzo Tarabini, and Cropp, Alex. “Mission analysis for PROBA-3 nominal operations”. In: *Acta Astronautica* 102 (2014), pp. 296–310.

[50] Peters, Thomas V and Noomen, Ron. “Linear cotangential transfers and safe orbits for elliptic orbit rendezvous”. In: *Journal of Guidance, Control, and Dynamics* 44.4 (2020), pp. 732–748.

[51] Peters, Thomas V, Noomen, Ron, and Colmenarejo, Pablo. “Analytical Solutions to Two-Impulse Nondrifting Transfer Problems for Rendezvous in Elliptical Orbits”. In: *Journal of Guidance, Control, and Dynamics* 37.3 (2014), pp. 775–788.

[52] Peters, TV. “Guidance for rendezvous and formation flying in elliptical orbits”. In: (2024).

[53] Riggi, Lucas and D’Amico, Simone. “Optimal impulsive closed-form control for spacecraft formation flying and rendezvous”. In: *2016 american control conference (acc)*. IEEE. 2016, pp. 5854–5861.

[54] Roscoe, Christopher WT, Vadali, Srinivas R, Alfriend, Kyle T, and Desai, Uri P. “Optimal formation design for magnetospheric multiscale mission using differential orbital elements”. In: *Journal of Guidance, Control, and Dynamics* 34.4 (2011), pp. 1070–1080.

[55] Roscoe, Christopher WT, Westphal, Jason J, and Mosleh, Ehson. “Overview and GNC design of the CubeSat Proximity Operations Demonstration (CPOD) mission”. In: *Acta Astronautica* 153 (2018), pp. 410–421.

[56] Sasaki, Takahiro, Nakajima, Yu, and Yamamoto, Toru. “Proximity approaches and design strategies for non-cooperative rendezvous v-bar hopping vs. spiral approach”. In: *Transactions of the Japan Society for Aeronautical and Space Sciences* 64.3 (2021), pp. 136–146.

[57] Schaub, Hanspeter. “Relative orbit geometry through classical orbit element differences”. In: *Journal of Guidance, Control, and Dynamics* 27.5 (2004), pp. 839–848.

[58] Schaub, Hanspeter and Alfriend, Kyle T. “Impulsive feedback control to establish specific mean orbit elements of spacecraft formations”. In: *Journal of guidance, control, and dynamics* 24.4 (2001), pp. 739–745.

[59] Schaub, Hanspeter and Alfriend, Kyle T. “J2 invariant relative orbits for spacecraft formations”. In: *Celestial Mechanics and Dynamical Astronomy* 79.2 (2001), pp. 77–95.

[60] Schaub, Hanspeter and Junkins, John L. *Analytical mechanics of space systems*. Aiaa, 2003.

[61] Space-Track. *Space-Track Satellite Catalog*. `https://www.space-track.org/`. Accessed: July 2025.

[62] Sullivan, Joshua, Grimberg, Sebastian, and D’Amico, Simone. “Comprehensive survey and assessment of spacecraft relative motion dynamics models”. In: *Journal of Guidance, Control, and Dynamics* 40.8 (2017), pp. 1837–1859.

[63] Swiatek, Paulina, Innocenti, Luisa, Wolahan, Andrew, Capogna, Fulvio, Caiazzo, Antonio, and Vakaet, Christophe. *Design Principles for Sustainable Close Proximity Operations*. 2019.

[64] Vasconcelos, José, Gaggi, Serena, Amaral, Tiago, Bakouche, Charles, Cotuna, Adina, and Friaças, Ana. “Close-Proximity Operations Design, Analysis, and Validation for Non-Cooperative Targets with an Application to the ClearSpace-1 Mission”. In: *Aerospace* 12.1 (2025), p. 67.

[65] Vela, Claudio, Opromolla, Roberto, and Fasano, Giancarmine. “A low-thrust finite state machine based controller for N-satellites formations in distributed synthetic aperture radar applications”. In: *Acta Astronautica* 202 (2023), pp. 686–704.

[66] Watson, David F. “Computing the n-dimensional Delaunay tessellation with application to Voronoi polytopes”. In: *The computer journal* 24.2 (1981), pp. 167–172.

[67] Wikipedia contributors. *Osculating orbit*. `https://en.wikipedia.org/wiki/Osculating_orbit`. 2025.

[68] Wikipedia contributors. *Transport Theorem*. `https://en.wikipedia.org/wiki/Transport_theorem`. 2025.

[69] Woffinden, David C and Geller, David K. “Navigating the road to autonomous orbital rendezvous”. In: *Journal of Spacecraft and Rockets* 44.4 (2007), pp. 898–909.

[70] Xie, Yongchun, Chen, Changqing, Liu, Tao, and Wang, Min. *Guidance, navigation, and control for spacecraft rendezvous and docking: theory and methods*. Springer Nature, 2021.

[71] Yamamoto, Toru, Matsumoto, Jun, Okamoto, Hiroyuki, Yoshida, Ryota, Hoshino, Chiharu, and Yamanaka, Koji. “Pave the way for active debris removal realization: Jaxa commercial removal of debris demonstration (crd2)”. In: *8th European Conference on Space Debris*. 2021, p. 200.

[72] Yamanaka, Koji and Ankersen, Finn. “New state transition matrix for relative motion on an arbitrary elliptical orbit”. In: *Journal of guidance, control, and dynamics* 25.1 (2002), pp. 60–66.

Appendix - Contents

Appendix A

Linear Conversion Matrices

The following matrix of partial derivatives provides the linear map which converts a relative state expressed in the quasi-non-singular ROE set $\delta\alpha_{qns}$ (see Eq.2.19) to the relative orbit C-elements $\mathbf{C}$ (see Eq.2.22), based on reference [50]:

$$\frac{\partial \mathbf{C}}{\partial \delta \boldsymbol{\alpha}_{qns}} = p \cdot \begin{bmatrix} 1 & 0 & -2\eta^{-2} e\cos\omega & -2\eta^{-2} e\sin\omega & 0 & 0 \\ e & 0 & -\eta^{-2}(1+e^2)\cos\omega & -\eta^{-2}(1+e^2)\sin\omega & 0 & 0 \\ 0 & 0 & \sin\omega & -\cos\omega & 0 & -e\cot i \\ 0 & \eta^{-3} & \frac{\sin\omega}{\eta^3}\sqrt{\frac{1-\eta}{1+\eta}} & -\frac{\cos\omega}{\eta^3}\sqrt{\frac{1-\eta}{1+\eta}} & 0 & \cot i\,\eta^{-2}(1-1/\eta) \\ 0 & 0 & 0 & 0 & -\cos\omega & -\sin\omega \\ 0 & 0 & 0 & 0 & \sin\omega & -\cos\omega \end{bmatrix} \tag{A.1}$$

The newly derived inverse transformation is also provided:

$$\frac{\partial \delta \boldsymbol{\alpha}_{qns}}{\partial \mathbf{C}} = \frac{1}{p} \cdot \begin{bmatrix} -\frac{e^2+1}{(e^2-1)} & \frac{2e}{(e^2-1)} & 0 & 0 & 0 & 0 \\ 0 & 0 & -K_1 & \eta^3 & \sin\omega \cdot K_2 & \cos\omega \cdot K_2 \\ \frac{e\eta^2\cos\omega}{(-e^2+1)} & -\frac{\eta^2\cos\omega}{(-e^2+1)} & \sin\omega & 0 & -e\cot i\sin^2\omega & -e\cot i\cos\omega\sin\omega \\ \frac{e\eta^2\sin\omega}{(-e^2+1)} & -\frac{\eta^2\sin\omega}{(-e^2+1)} & -\cos\omega & 0 & e\cot i\cos\omega\sin\omega & e\cot i\cos^2\omega \\ 0 & 0 & 0 & 0 & -\cos\omega & \sin\omega \\ 0 & 0 & 0 & 0 & -\sin\omega & -\cos\omega \end{bmatrix} \tag{A.2}$$

$$K_1 = \sqrt{-(\eta-1)/(\eta+1)}$$

$$K_2 = \cot i\ (\eta - 1 + e \cdot K_1)$$

Appendix B

State Transition Matrices

The current appendix reports the linear propagation models for the quasi-non-singular ROE set which are used in the thesis to account for different types of orbit perturbations for arbitrary target eccentricities.

B.1 Inclusion of First-Order J2 Secular Effects

Based on reference: [28]

$$\Phi_{J_2}^{ROE} = \begin{bmatrix} 1 & 0 & 0 & 0 & 0 & 0 \\ \Phi_{21} & 1 & \Phi_{23} & \Phi_{24} & \Phi_{25} & 0 \\ \Phi_{31} & 0 & \Phi_{33} & \Phi_{34} & \Phi_{35} & 0 \\ \Phi_{41} & 0 & \Phi_{43} & \Phi_{44} & \Phi_{45} & 0 \\ 0 & 0 & 0 & 0 & 1 & 0 \\ \Phi_{61} & 0 & \Phi_{63} & \Phi_{64} & \Phi_{65} & 1 \end{bmatrix} \tag{B.1}$$

$$\begin{aligned} \Phi_{21} &= -\frac{3}{2}n\Delta t - \frac{21}{8}K_2\frac{n\Delta t}{\eta^4}H(\eta+1) & \Phi_{61} &= \frac{21}{8}K_2\frac{n\Delta t}{\eta^4}\sin 2i \\ \Phi_{23} &= \frac{3}{4}K_2 e_{x,0}\frac{n\Delta t}{\eta^6}H(3\eta+4) & \Phi_{63} &= -3K_2 e_{x,0}\frac{n\Delta t}{\eta^6}\sin 2i \\ \Phi_{24} &= \frac{3}{4}K_2 e_{y,0}\frac{n\Delta t}{\eta^6}H(3\eta+4) & \Phi_{64} &= -3K_2 e_{y,0}\frac{n\Delta t}{\eta^6}\sin 2i \\ \Phi_{25} &= -\frac{3}{4}K_2\frac{n\Delta t}{\eta^4}\sin 2i(3\eta+4) & \Phi_{65} &= \frac{3}{2}K_2\frac{n\Delta t}{\eta^4}\sin^2 i \end{aligned} \tag{B.2}$$

$$
\begin{aligned}
\Phi_{31} &= -\frac{21}{8}K_2\frac{n\Delta t}{\eta^4}A_1K & \Phi_{41} &= -\frac{21}{8}K_2\frac{n\Delta t}{\eta^4}A_2K \\
\Phi_{33} &= C + 3K_2\frac{n\Delta t}{\eta^6}e_{x,0}A_1K & \Phi_{43} &= S + 3K_2\frac{n\Delta t}{\eta^6}e_{x,0}A_2K \\
\Phi_{34} &= -S + 3K_2\frac{n\Delta t}{\eta^6}e_{y,0}A_1K & \Phi_{44} &= C + 3K_2\frac{n\Delta t}{\eta^6}e_{y,0}QA_2K \\
\Phi_{35} &= -\frac{15}{4}K_2\frac{n\Delta t}{\eta^4}A_1\sin 2i & \Phi_{45} &= -\frac{15}{4}K_2\frac{n\Delta t}{\eta^4}A_2\sin 2i
\end{aligned}
\tag{B.3}
$$

where the following parameters are defined:

$$
\begin{aligned}
K_2 &= J_2(R_E/a)^2 & \Delta t &= t_F - t_0 \\
e_{x,0} &= e\cos\omega & e_{y,0} &= e\sin\omega \\
H &= 3\cos^2 i - 1 & K &= 5\cos^2 i - 1 \\
S &= \sin\left(\frac{3}{4}K_2\frac{n\Delta t}{\eta^4}K\right) & C &= \cos\left(\frac{3}{4}K_2\frac{n\Delta t}{\eta^4}K\right) \\
A_1 &= -(Se_{x,0} + Ce_{y,0}) & A_2 &= (Ce_{x,0} - Se_{y,0})
\end{aligned}
\tag{B.4}
$$

B.2 Inclusion of Differential Drag Effects

Density-model-free method based on reference: [39].

$$
\Phi^{ROE}_{J_2+drag} = \begin{bmatrix} \Phi^{ROE}_{J_2} & \begin{bmatrix} \Delta t & 0 & 0 \\ -\left(\frac{3}{4}n + \frac{7}{4}kEP\right)\Delta t^2 & \frac{1}{2}keFGP\Delta t^2 & 0 \\ \frac{7}{4}ke_{yf}Q\Delta t^2 & \cos\omega_f\Delta t - 2kee_{yf}GQ\Delta t^2 & -\sin\omega_f\Delta t \\ -\frac{7}{4}ke_{xf}Q\Delta t^2 & \sin\omega_f\Delta t + 2kee_{xf}GQ\Delta t^2 & \cos\omega_f\Delta t \\ 0 & 0 & 0 \\ \frac{7}{4}kS\Delta t^2 & -2keGS\Delta t^2 & 0 \end{bmatrix} \\ \mathbf{o}_{3\times 6} & \mathbf{I}_{3\times 3} \end{bmatrix}
\tag{B.5}
$$

$$
\begin{aligned}
k &= \frac{3}{4}\frac{J_2R_E^2\sqrt{\mu}}{a^{7/2}\eta^4}, & E &= 1+\eta, \quad F = 4+3\eta \\
G &= 1/\eta^2, & P &= 3\cos^2 i - 1 \quad Q = 5\cos^2 i - 1 \\
S &= \sin 2i \qquad \omega_f = \omega + kQ\Delta t \qquad e_{xf} = e\cos\omega_f \quad e_{yf} = e\sin\omega_f
\end{aligned}
\tag{B.6}
$$

The STM reported in Eq.B.5 propagates the augmented quasi-non-singular ROE state vector defined as in the following:

$$
\delta\boldsymbol{\alpha}_{AUG} = \begin{bmatrix} \delta\boldsymbol{\alpha} & \delta\dot{a}_{drag} & \delta\dot{e}'_{x,drag} & \delta\dot{e}'_{y,drag} \end{bmatrix}^T
\tag{B.7}
$$

where the $'$ symbol identifies a modified ROE set which is obtained by simply rotating the relative eccentricity vector:

$$\delta\boldsymbol{\alpha}' = J(\boldsymbol{\alpha}_T)\delta\boldsymbol{\alpha} = \begin{bmatrix} I_{2\times2} & 0_{2\times2} & 0_{2\times2} \\ 0_{2\times2} & \begin{bmatrix} \cos\omega & \sin\omega \\ -\sin\omega & \cos\omega \end{bmatrix} & 0_{2\times2} \\ 0_{2\times2} & 0_{2\times2} & I_{2\times2} \end{bmatrix} \delta\boldsymbol{\alpha} \tag{B.8}$$

The key aspect of this method is the need to estimate the constant rates which augment the initial relative state vector; this can be done in orbit during a stationary "initialisation phase" during which the navigation stores the estimated ROE over time and filters out the mean effects due to J_2 using the following equation:

$$\delta\boldsymbol{\alpha}_{drag}(t) = J(\boldsymbol{\alpha}_T(t_i))\delta\boldsymbol{\alpha}_{est}(t) - A^{J_2}((\boldsymbol{\alpha}_T(t_i))J(\boldsymbol{\alpha}_T(t_i))\delta\boldsymbol{\alpha}_{est}(t_i)\cdot(t-t_i) \tag{B.9}$$

$$A^{J_2} = k\begin{bmatrix} 0 & 0 & 0 & 0 & 0 & 0 \\ -\frac{7}{2}EP & 0 & eFGP & 0 & -FS & 0 \\ 0 & 0 & 0 & 0 & 0 & 0 \\ -\frac{7}{2}eQ & 0 & 4e^2GQ & 0 & -5eS & 0 \\ 0 & 0 & 0 & 0 & 0 & 0 \\ \frac{7}{2}S & 0 & -4eGS & 0 & 2T & 0 \end{bmatrix}, \qquad T = \sin^2 i \tag{B.10}$$

which essentially casts the ROE in the modified set and removes the mean effects of J_2 using the plant matrix A^{J_2}. Once such a dataset is available over few orbits, a simple linear regression on the values of δa, $\delta e'_x$ and $\delta e'_y$ can be used to compute their time derivative over the initialisation interval.

Appendix C

Input Matrices

C.1 Velocity-Aligned Frame

The following reports the input matrix which maps a change in orbital velocity (expressed in the TAN frame) into a change in quasi-non-singular ROE for arbitrary target eccentricities, as developed in Sec.3.2.

$$\mathcal{B}_{TAN} = \begin{bmatrix} \frac{2av}{\mu} & 0 & 0 \\ \left(\frac{2\sin f}{v}\sqrt{\frac{1-\eta}{1+\eta}} - \frac{2re\eta\sin f}{vp}\right) & 0 & \left(+\frac{2}{v} + \frac{r\cos f}{va}\sqrt{\frac{1-\eta}{1+\eta}}\right) \\ \left(\frac{2e\cos\omega}{v} + \frac{2}{v}\cos(\omega+f)\right) & \left(-\frac{e\sin\omega\cdot r\sin(f+\omega)\cos i}{h\sin i}\right) & \left(-\frac{r}{va}\sin(\omega+f) - \frac{2e\sin\omega}{v}\right) \\ \left(\frac{2e\sin\omega}{v} + \frac{2}{v}\sin(\omega+f)\right) & \left(\frac{e\cos\omega\cdot r\sin(f+\omega)\cos i}{h\sin i}\right) & \left(\frac{r}{va}\cos(\omega+f) + \frac{2e\cos\omega}{v}\right) \\ 0 & \left(-\frac{r\cos(f+\omega)}{h}\right) & 0 \\ 0 & \left(-\frac{r\sin(f+\omega)}{h}\right) & 0 \end{bmatrix} \tag{C.1}$$

C.2 LVLH Frame

$$\mathcal{B}_{LVLH} = \begin{bmatrix} \frac{2\rho}{\eta an} & 0 & -\frac{2e\sin f}{\eta an} \\ \frac{\eta a(2\sin f + e\sin(2f)/2)}{\sqrt{\mu a}\cdot\rho}\sqrt{\frac{1-\eta}{1+\eta}} & 0 & \frac{\eta a\cos f\sqrt{(1-\eta)/(1+\eta)} + 2\eta + (1-\eta)\cos^2 f}{\sqrt{\mu a}\cdot\rho} \\ \eta\frac{(2+e\cos f)\cos(f+\omega) + e\cos\omega}{\rho na} & \left(-\frac{e\sin\omega\cdot r\sin(f+\omega)\cos i}{h\sin i}\right) & -\frac{\eta\sin(f+\omega)}{na} \\ \eta\frac{(2+e\cos f)\sin(f+\omega) + e\sin\omega}{\rho na} & \left(\frac{e\cos\omega\cdot r\sin(f+\omega)\cos i}{h\sin i}\right) & \frac{\eta\cos(f+\omega)}{na} \\ 0 & \left(-\frac{r\cos(f+\omega)}{h}\right) & 0 \\ 0 & \left(-\frac{r\sin(f+\omega)}{h}\right) & 0 \end{bmatrix} \tag{C.2}$$